

Heterogeneous single-site catalysts based on multi-component metal-organic frameworks (MOFs) for sustainable oxidation reactions in the liquid phase

Vom Fachbereich Chemie der Technischen Universität Kaiserslautern zur
Verleihung des akademischen Grades „**Doktor der Naturwissenschaften**“
genehmigte Dissertation

DE-386



vorgelegt von

Milada Teubnerová, M. Sc.

geboren in Brandýs nad Labem – Stará Boleslav

Betreuer: Prof. Dr. Wolfgang Kleist

Kaiserslautern, 26.03.2024

'Mischief managed'

J. K. Rowling, 1999

Die vorliegende Arbeit wurde von September 2018 bis Dezember 2020 in der Fachrichtung der Technische Chemie des Fachbereichs der Chemie an der Ruhr Universität Bochum und von Januar 2021 bis Dezember 2022 in der Fachrichtung der Technische Chemie des Fachbereichs der Chemie an der Rheinland-Pfälzischen Technischen Universität Kaiserslautern-Landau angefertigt.

Dekan: Prof. Dr. A. J. Pierik

Prüfungskommission:

Vorsitzender: Prof. Dr. S. Becker

1. Berichterstatter: Prof. Dr. W. Kleist
2. Berichterstatter: Prof. Dr. M. Muhler
3. Berichterstatter: Prof. Dr. G. Manolikakes

Acknowledgement

I would like to thank Prof. Dr. Wolfgang Kleist for the opportunity to start my PhD studies in his group. Furthermore, I want to thank him for being my first supervisor.

I want to thank Max Planck Institute in Mülheim an der Ruhr for the funding during the first months in Bochum and for being part of Recharge program. Also, a big thanks to the SFB TRR247 project (project number: 388390466) for the financial support almost during the whole time of my PhD. studies.

I am also grateful to my former colleagues Dr. Johannes Bitzer and Dr. Ceylan Yildiz for a huge help during the first months in Germany and also for the very nice atmosphere within our group in Bochum.

Above all my colleagues I want to thank Alina Ouissa for everything she did for me. For helping me to overcome all problems at work and also in my private life. Thanks to her also my German improved massively. I want to thank Ina Berwanger, Lena Langner, Andrea Lösch, Tim Herrendorf, Johannes Schaumlöffel, Benjamin Heider, Sven Schaefer and other colleagues in Kaiserslautern for the scientific discussions, help with measurements and also other support. I am also thankful to all my supervised students (Benjamin Heider, Lynn Kirchgatter, Julia Leandro, Tabea Sterbak and Sandra Poplawska) who helped me to investigate my project more deeply.

I thank Prof. Dr. Martin Muhler and his group in Bochum for a very nice time there. I also thank Prof. Ute Krämer und Petra Düchting for the ICP-OES Measurements in Bochum. Special thanks belong also to Dr. Ksenia Kutonova and Simon Oßwald from KIT for synthesizing the amino-linker.

Most importantly, I want to thank my family, the Ward family from Hohenecken and especially Josef Hájíček. When I was feeling the worst, those people were always there to help me. Josef Hájíček belong also special thanks for the patience and for the support not only in Germany but also during the writing process.

Abstract

Metal-organic frameworks (MOFs) have gained increasing attention in the last four decades due to their versatility and unique properties. They are often used as catalysts because they combine advantageous properties of both heterogeneous and homogeneous catalysts. Noble metals are very active in catalysis, but they are expensive, sometimes toxic to the environment and very rare. Therefore, the demand for the substitution of noble metals by commonly available metals such as iron or cobalt is of interest. The complexity and versatility of MOF materials is further enhanced by the use of mixed-linker and mixed-metal approaches or post-synthetic modification reactions.

The aim of this PhD project was to synthesize and characterize MOF-based catalysts which contain Co and Fe and to test the resulting materials in the liquid phase oxidation reaction of alcohols. In the first part of this work, mixed-metal CPO-27(Co,Fe) with three different metal ratios and two different spatial distributions were prepared. The spatial distributions of the metals were either statistically distributed or a core-shell orientation. The resulting catalysts were characterized by powder X-ray diffraction, thermogravimetric analysis and ICP-OES analysis. The results confirmed that the catalysts were highly porous, corresponded to the CPO-27 structure and that the amounts of metals were close to the desired ratios. The materials were then tested in oxidation reactions of benzyl alcohol and 1-phenylethanol. For the parameter optimization, the highly active monometallic CPO-27(Co) catalyst was used and parameters such as temperature and the amount of catalyst, substrate or oxidant (air) were investigated. Bimetallic CPO-27(Co,Fe) catalysts were then tested with the optimized parameters and both conversion and selectivity were compared to the monometallic CPO-27(Co) reference. In general, the rare and expensive cobalt can be partially replaced by cheap but inactive iron without affecting the catalytic activity and in some cases, the distribution of the metals in the MOF lattice have an effect on the catalytic performance.

In the second part of this work, the previously synthesized CPO-27(Co,Fe) catalysts were thermally decomposed in an inert atmosphere to obtain metal species which are encapsulated in a porous carbonaceous matrix *via* the so called MOF-mediated synthesis. The decomposition was expected to result in unique materials that could not be synthesized by any other route. The resulting materials were characterized by powder X-ray diffraction, N₂ physisorption and ICP-OES analysis. The characterization revealed differences between materials prepared from statistically distributed and core-shell-structured CPO-27(Co,Fe). These catalysts were also

tested in the oxidation of benzyl alcohol and compared not only within this series but also with the CPO-27 precursors, showing that in some cases the thermally decomposed materials were even more catalytically active than their MOF precursors.

In the last part of this thesis, Co,Fe DUT-5-based catalysts with core-shell structure and statistical distribution, respectively, were synthesized. The first step was to prepare a DUT-5-based framework. For the statistically distributed material, 4,4'-biphenyldicarboxylate, 2,2'-bipyridine-5,5'-dicarboxylate and 2-amino-4,4'-biphenyldicarboxylate linkers were mixed with an aluminum salt precursor. The 2,2'-bipyridine-5,5'-dicarboxylate linkers were then used to directly immobilize cobalt ions. The amine-functionalized linkers were post-synthetically modified with salicylaldehyde and the resulting chelating groups were finally used for the immobilization of iron ions. The core-shell backbone consisted of 4,4'-biphenyldicarboxylate and 2,2'-bipyridine-5,5'-dicarboxylate in the core. The first shell contained only unfunctionalized 4,4'-biphenyldicarboxylate and the outer shell consisted of a mixture of 2-amino-4,4'-biphenyldicarboxylate and 4,4'-biphenyldicarboxylate linkers. The post-synthetic reactions were then performed analogously to the statistically distributed materials: (1) cobalt immobilization at the bipyridine linkers, (2) insertion of chelating groups at the amine linkers and (3) iron immobilization. All materials were thoroughly characterized after each synthesis step using powder X-ray diffraction, infrared spectroscopy, thermogravimetric analysis, N₂ physisorption and ICP-OES analysis. The linker ratios were calculated by ¹H NMR of diluted samples. The results confirmed the formation of a porous material with a DUT-5 structure, but the spatial distribution could not be confirmed unambiguously by the methods used. Both materials were tested, together with a monometallic DUT-5 BPyDC(Co) reference, in oxidation reactions cinnamyl alcohol. The results showed significant differences between the statistically distributed and core-shell catalysts, providing evidence for the difference in spatial orientations and the synergistic effects of the two metals.

In summary, novel MOF materials containing Co and Fe were synthesized, characterized and tested in oxidation reactions of primary and secondary alcohols under aerobic conditions. The results confirmed that in some cases a part of rare cobalt could be replaced by cheap and widely available iron without decreasing the catalytic activity and selectivity. In addition, the spatial distribution of the metals can have a direct and massive influence on the catalytic properties and therefore, a thorough characterization is a very important part of the synthesis process.

Kurzfassung

Metall-organische Gerüstverbindungen (metal-organic frameworks, MOFs) haben in den letzten vier Jahrzehnten aufgrund ihrer Vielseitigkeit und einzigartigen Eigenschaften an Bedeutung gewonnen. Sie werden häufig als Katalysatoren verwendet, weil sie vorteilhafte Eigenschaften sowohl von heterogenen als auch von homogenen Katalysatoren in sich vereinen. Edelmetalle sind häufig sehr aktiv in der Katalyse, aber sie sind teuer, manchmal giftig für die Umwelt und sehr selten. Daher ist es von Interesse, diese Edelmetalle durch allgemein verfügbare Metalle wie Cobalt oder Eisen zu ersetzen. Die Komplexität und Vielseitigkeit von MOF-Materialien kann durch den Einsatz von Mixed-Linker- und Mixed-Metal-Konzepten oder durch postsynthetische Modifizierungen noch gesteigert werden.

Ziel dieses Dissertationsprojekts war die Synthese und Charakterisierung von MOF-basierten Co, Fe-Katalysatoren und die Anwendung der resultierenden Materialien in Oxidationsreaktionen von Alkoholen in flüssiger Phase. Im ersten Teil dieser Arbeit wurden Mixed-Metal- CPO-27(Co,Fe)-Materialien mit drei verschiedenen Metallverhältnissen und zwei verschiedenen räumlichen Verteilungen der beiden Metalle hergestellt. Die Metalle waren entweder statistisch verteilt oder in Kern-Schale-Form im Gerüst eingebaut. Die resultierenden Katalysatoren wurden mittels Röntgenpulverdiffraktometrie, Thermogravimetrie und ICP-OES-Analytik charakterisiert. Es wurde bestätigt, dass die Katalysatoren hochporös waren und der CPO-27-Struktur entsprachen und dass die Metallgehalte den gewünschten Werten entsprachen. Die resultierenden Materialien wurden dann in Oxidationsreaktionen von Benzylalkohol und 1-Phenylethanol getestet. Für die Parameteroptimierung wurde ein hochaktiver monometalischer CPO-27(Co)-Katalysator verwendet, und Parameter wie Temperatur, Katalysatormenge, Substratmenge oder Flussrate des Oxidationsmittels (Luft) wurden variiert. Bimetallische CPO-27(Co,Fe)-Katalysatoren wurden dann unter den optimierten Parametern getestet und Umsätze und Selektivitäten mit der monometallischen CPO-27(Co)-Referenz verglichen. Das hochaktive Co kann dabei zum Teil durch kostengünstiges Fe ersetzt werden, ohne die katalytische Aktivität negativ zu beeinflussen.

In dem zweiten Teil dieser Arbeit wurden die zuvor synthetisierten CPO-27(Co,Fe)-Katalysatoren in einer inerten Atmosphäre thermisch zersetzt, um unter kontrollierten Bedingungen gewünschte Metallspezies eingebettet in einer porösen kohlenstoffhaltigen Matrix zu erhalten. Diese Präparationsmethode ermöglicht es, einzigartige Materialien herzustellen, die auf keinem anderen Weg synthetisiert werden können. Die resultierenden

Materialien wurden mittels Röntgenpulverdiffraktometrie, N₂ Physisorption und ICP-OES charakterisiert. Die Charakterisierung ergab Unterschiede zwischen den Materialien, mit statistischer Verteilung der beiden Metalle und der Kern-Schale-Struktur. Auch diese Katalysatoren wurden in der Oxidation von Benzylalkohol getestet und nicht nur untereinander, sondern auch in ihren CPO-27 Vorstufen verglichen, wobei sich herausstellte, dass die thermisch zersetzten Materialien in einigen Fällen sogar katalytisch aktiver waren als ihre MOF-Vorstufen.

Im letzten Teil dieser Arbeit wurden Co, Fe-haltige Katalysatoren auf Basis von DUT-5 mit Kern-Schale-Struktur und statistischer Verteilung synthetisiert. Der erste Schritt bestand darin, Gerüststrukturen auf Basis von DUT-5 herzustellen. Für das statistisch verteilte Material wurden 4,4'-Biphenyldicarboxylat, 2,2'-Bipyridin-5,5'-dicarboxylat und 2-Amino-4,4'-biphenyldicarboxylat als Linker so wie ein Aluminiumsalz eingesetzt. Die 2,2'-Bipyridin-5,5'-dicarboxylat-Linker wurden dann zur direkten Immobilisierung von Cobalt verwendet. Die aminfunktionalisierten Linker wurden anschließend mit Salicylaldehyd postsynthetisch modifiziert und die resultierenden Chelatgruppen zur Immobilisierung von Eisenionen genutzt. Die verbauten Linker in Kern-Schale-Grundgerüst bestanden aus 4,4'-Biphenyldicarboxylat und 2,2'-Bipyridin-5,5'-dicarboxylat im Kern. Die erste Schale enthielt ausschließlich unfunktionalisiertes 4,4'-Biphenyldicarboxylat und die äußere Schale bestand aus einer Mischung aus 2-Amino-4,4'-biphenyldicarboxylat- und 4,4'-Biphenyldicarboxylat-Linkern. Die post-synthetischen Reaktionen wurden dann analog zu den statistisch verteilten Materialien durchgeführt: (1) Immobilisierung von Cobalt an den Bipyridinlinkern, (2) Einfügung von Chelatgruppen an den Aminlinkern und (3) Immobilisierung von Eisen. Beide Materialien wurden nach jedem Syntheseschritt mittels Röntgenpulverdiffraktometrie, Infrarotspektroskopie, thermo-gravimetrische Analyse, N₂-Physisorption und ICP-OES-Analyse charakterisiert. Das Linkerverhältnis wurde durch ¹H-NMR der aufgelösten Proben bestimmt. Die Katalyseergebnisse zeigten deutliche Unterschiede zwischen den statistisch verteilten und den Kern-Schale Katalysatoren, was einen Beweis für die unterschiedlichen räumlichen Anordnungen liefert.

Zusammenfassend wurden neuartige Co,Fe-haltige MOF-Materialien synthetisiert, charakterisiert und in Oxidationsreaktionen von primären und sekundären Alkoholen unter Verwendung von Luftsauerstoff als Oxidationsmittel getestet. Die Ergebnisse bestätigten, dass ein Teil des hochaktiven Cobalts durch kostengünstiges und in größeren Mengen verfügbares Eisen ersetzt werden kann, ohne dabei die katalytische Aktivität und Selektivität zu verringern.

Darüber hinaus konnte gezeigt werden, dass die räumliche Verteilung der beiden Metalle einen direkten und massiven Einfluss auf die Katalyse hat, weshalb die Charakterisierung ein sehr wichtiger Teil des Syntheseprozesses ist.

Table of contents

Acknowledgement	I
Abstract	III
Kurzfassung	V
1 Scientific background.....	1
1.1 Synthesis of metal-organic frameworks.....	1
1.2 Isorecticular MOF structures	5
1.3 Multi-component metal-organic frameworks	5
1.3.1 Mixed-linker metal-organic frameworks.....	7
1.3.2 Mixed-metal metal organic frameworks	8
1.4 Post-synthetic modification (PSM).....	11
1.4.1 Post-synthetic exchange	11
1.4.2 Immobilization of metals on linker molecules	13
1.4.3 Post-synthetic modification of amine-functionalized MOFs	15
1.5 Metal-organic frameworks with terephthalate-based linkers.....	16
1.5.1 MOF-5.....	17
1.5.2 MIL-53	18
1.5.3 CPO-27.....	19
1.6 Metal-organic frameworks with 4,4'-biphenyl-dicarboxylate-based linkers.....	20
1.6.1 DUT-5	21
1.6.2 MOF-253	22
1.6.3 UiO-67.....	23
1.7 MOF-mediated synthesis of heterogeneous catalysts (controlled decomposition of MOFs).....	24
1.8 Metal-organic frameworks as catalysts in liquid phase oxidation reactions.....	25
2 Motivation	29
3 Results and discussion.....	31
3.1 Synthesis, characterization and catalytic performance of CPO-27 materials.....	31
3.1.1 Synthesis and characterization of monometallic CPO-27 materials	31
3.1.2 Synthesis and characterization of bimetallic CPO-27(Co,Fe) materials with statistical distribution	35

3.1.3 Bimetallic CPO-27(Co,Fe) materials with core-shell structure	38
3.1.4 Catalytic applications of CPO-27-based materials.....	42
3.1.4.1 Application of statistically distributed CPO-27(Co,Fe) catalysts in the liquid phase oxidation of 1-phenylethanol	42
3.1.4.2 Application of CPO-27-based catalysts in liquid phase oxidation reaction of benzyl alcohol	49
a) Statistically distributed CPO-27(Co,Fe) catalysts.....	52
b) Core-shell-structured CPO-27 catalysts	54
3.2 Thermal decomposition of CPO-27 materials	56
3.2.1 Thermal decomposition of monometallic CPO-27 materials.....	57
3.2.2 Thermal decomposition of bimetallic CPO-27(Co,Fe) with statistical distribution ..	59
3.2.3 Thermal decomposition of CPO-27(Co,Fe) materials with core-shell structure....	60
3.2.3.1 Co@Fe/C materials decomposed from CPO-27(Co)@CPO-27(Fe)	60
3.2.3.2 Fe@Co/C materials decomposed from CPO-27(Fe)@CPO-27(Co)	61
3.2.4 Application of thermally decomposed MOF materials in the oxidation of benzyl alcohol	63
3.2.4.1 Statistically distributed Co,Fe/C catalysts.....	63
3.2.4.2 Core-shell-structured Co,Fe/C catalysts.....	64
3.3 Synthesis, characterization and catalytic performance of DUT-5-based materials	67
3.3.1 DUT-5-based materials with statistical distribution.....	67
3.3.2 DUT-5-based materials with core-shell structure	71
3.3.3 Application of DUT-5 materials in oxidation of cinnamyl alcohol	76
4 Summary and Conclusions	79
5 Experimental part	83
5.1 Chemicals.....	83
5.2 Syntheses.....	83
5.2.1 Monometallic CPO-27 materials.....	83
5.2.2 CPO-27-based materials with statistical distribution	83
5.2.3 CPO-27-based materials with core-shell structure	85
5.2.4 Thermal decomposition of CPO-27 materials.....	87
5.2.5 DUT-5-based materials with statistical distribution.....	87
5.2.6 DUT-5-based materials with core-shell distribution	88

Table of contents

5.2.7 Post-synthetic modification reaction	89
5.3 Analytical methods	90
5.3.1 Attenuated total reflection infrared spectroscopy (ATR-IR)	90
5.3.2 Gas chromatography coupled with mass spectrometry	90
5.3.3 Inductively coupled plasma optical emission spectrometry (ICP-OES)	92
5.3.4 Nitrogen physisorption	92
5.3.5 Nuclear magnetic resonance spectroscopy (NMR)	92
5.3.6 Powder X-ray Diffraction.....	93
5.3.7 Thermogravimetric analysis (TGA)	93
5.3.8 X-ray absorption spectroscopy (XAS)	93
5.4 Catalytic tests	93
5.4.1 Oxidation of benzyl alcohol	93
5.4.2 Oxidation of 1-phenylethanol.....	94
5.4.3 Oxidation of cinnamyl alcohol	94
6 Abbreviations and symbols.....	97
7 References	102
Appendix	109

1 Scientific background

Metal-organic frameworks (MOFs) or porous coordination polymers (PCPs) represent a unique category of porous crystalline structures. They consist of organic linkers bridged by metal ions or clusters, forming mostly two- or three-dimensional highly ordered networks. The metal centers are usually transition metals or metal-oxoclusters, which are also called secondary building units (SBUs). Organic linkers typically contain at least two functional groups – mostly carboxylates, phosphates or sulfates. The choice of a linker defines the shape and size of pores in the framework, which and can be tuned according to the usage.^[1,2]

These crystalline porous networks are characteristic for their (ultra)high specific surface area (usually between $S_{\text{BET}}=1000 - 2000 \text{ m}^2/\text{g}$, but also much higher values were reported), which makes MOFs a very interesting group of materials.^[3] In some cases, the structural flexibility of MOFs allows reversible structural transformations in response to external stimuli such as changes of the temperature, pressure, or during gas adsorption, which is called the breathing effect.^[4–6] Among the first groups investigating metal-organic frameworks and their properties were the groups of Férey^[7–11], Kitagawa^[12–14] or Yaghi^[15–18]. Nowadays, the research scope of metal-organic frameworks is broad and, therefore, more than 90,000 of MOF structures have already been described and more than 500,000 of structures were predicted.^[19]

Due to their unique properties, MOFs appear ideal for various applications, including the storage of clean energy carriers, such as hydrogen^[20–22] and methane^[23–25]. They can also be used in gas separation, for example for the selective capturing of carbon dioxide, one of the most relevant greenhouse gases.^[23,26,27] MOFs also can enable a controlled drug delivery, using the uniform defined pores to encapsulate and release therapeutic agents.^[28–30] Most importantly, MOFs are investigated and used as highly active heterogeneous catalysts both in the gas phase as well as in the liquid phase.^[14,31–34]

1.1 Synthesis of metal-organic frameworks

During the synthesis of metal-organic frameworks the choice of heat source, temperature, solvent and other parameters is critical, as the conditions can have a direct impact on the synthesized materials and their properties.^[30,35,36] In this chapter, some of the techniques will be discussed and also presented using examples.

The classic strategies for MOF synthesis include solvothermal synthesis, in which the metal salt and the organic ligand are dissolved in a solvent and transferred into a sealed reaction flask or an autoclave. The elevated temperature and pressure is crucial for the synthesis of the desired MOF structure.^[37–39] A special example of this method is the hydrothermal synthesis, where water is used as a solvent. It is necessary that all chemicals are soluble in water and the resulting MOF material is water-resistant and also resistant towards other chemicals present in the reaction mixture. This was crucial for example in the case of Buragohain *et al.*^[40], who presented a hydrothermal synthesis of Cr-MIL-101-X (X= F, Cl, Br, CH₃, F₂ and (CH₃)₂) where water and concentrated HCl was placed in a Teflon-lined stainless steel autoclave and heated at 180 °C for 144 h. Another solvent-based method of synthesis is a microwave-assisted synthesis where microwave irradiation accelerates the MOF formation, which reduces significantly the reaction times and improves the product yields. Moreover, this method often requires lower amount of solvents and the consumption of energy is lower, which contributes to a bigger environmental and economical sustainability. An example of a microwave assisted synthesis can be MIL-53(Al) where the particle size range and morphology can be controlled by altering the microwave power.^[41] In the respective article, the authors presented the synthesis of 62 mg of MIL-53(Al) in only 4.3 seconds, which shows the ability of microwaves to shorten the synthesis time. The next solvent-based method is ultrasound-assisted synthesis, where ultrasound waves promote the mixing of reactants and enhance the nucleation, leading to the rapid formation of MOFs.^[42–44] The influence of ultrasound setups on crystallinity and crystallite size was presented for the MOF-5 structure and compared to conventional solvothermal synthesis.^[45] Smaller crystallites were obtained during the ultrasound synthesis than with the solvothermal synthesis in 1-methyl-2-pyrrolidone (NMP). Increasing the power level above 30 % led to impurities and the crystal quality decreased significantly with increasing reaction time, probably due to the high temperatures generated by the prolonged irradiation.^[45]

Another method that has been frequently used is the classical synthesis in liquid phase, which involves the dissolution of metal precursors and organic linkers in a suitable solvent to form a homogeneous solution, followed by the controlled nucleation and growth of MOF crystals under specific reaction conditions. Unlike in the solvothermal synthesis, the temperature is not above the boiling point of the respective solvent mixture and the reaction is performed at ambient pressure, which enables to decrease the costs. Sanz *et al.*^[46] presented the synthesis of CPO-27(Cu) using 20 ml of DMF (b.p. 153 °C) and water/2-propanol as solvents. This mixture

was heated up to 100 °C for 18 hours to yield reddish needle-shaped crystals. The solvent composition (DMF/2-propanol ratio) had a direct impact on material properties, such as specific surface area, pore volume and CO₂ adsorption capacity. All of the above mentioned properties increased when 2-propanol was used instead of water together with DMF, due to an increase of crystallinity.^[46] Kleist *et al.*^[47] presented a novel synthesis for MOF-5 in 2010. Until then, MOF-5 was synthesized under solvothermal conditions with a base, as the slow deprotonation of the acid groups of benzene-1,4-dicarboxylic acid allowed for the slow and controlled precipitation of the MOF material. This approach was, however, unsuitable for mixed-linker analogs with amine-functionalized linkers, because of the different acid constants of unfunctionalized and functionalized linker molecules. In the novel approach, benzene-1,4-dicarboxylic acid and Zn(NO₃)₂·6H₂O were dissolved in 500 ml of DMF at room temperature in round-bottom flask under reflux and heated to 150 °C for 18 h, resulting in highly porous MOF-5-based catalysts.^[47]

The next type of synthesis is the mechanochemical synthesis, which is recently gaining increasing attention as this method eliminates partially or entirely the need for solvents and thus, reduces waste generated during the synthesis. Synthesis of MOF-74(Zn), during which solid reactants and a very low amount of solvent are ground together in a ball mill, was investigated by Julien *et al.*^[48] and Beamish-Cook *et al.*^[49] Julien *et al.* used very low amount of water (solid/liquid ratio of 0.625 µl/mg) and observed one intermediate in an *in situ* experiment (**Figure 1a**). On the other hand, Beamish-Cook *et al.* used a low amount of DMF during the mechanochemical synthesis and observed four different intermediates before the final MOF-74 structure was built (**Figure 1b**). Even though, both syntheses led to the creation of MOF-74 structure, mechanistic investigation is crucial for the rational design of mechanochemical syntheses of MOFs.

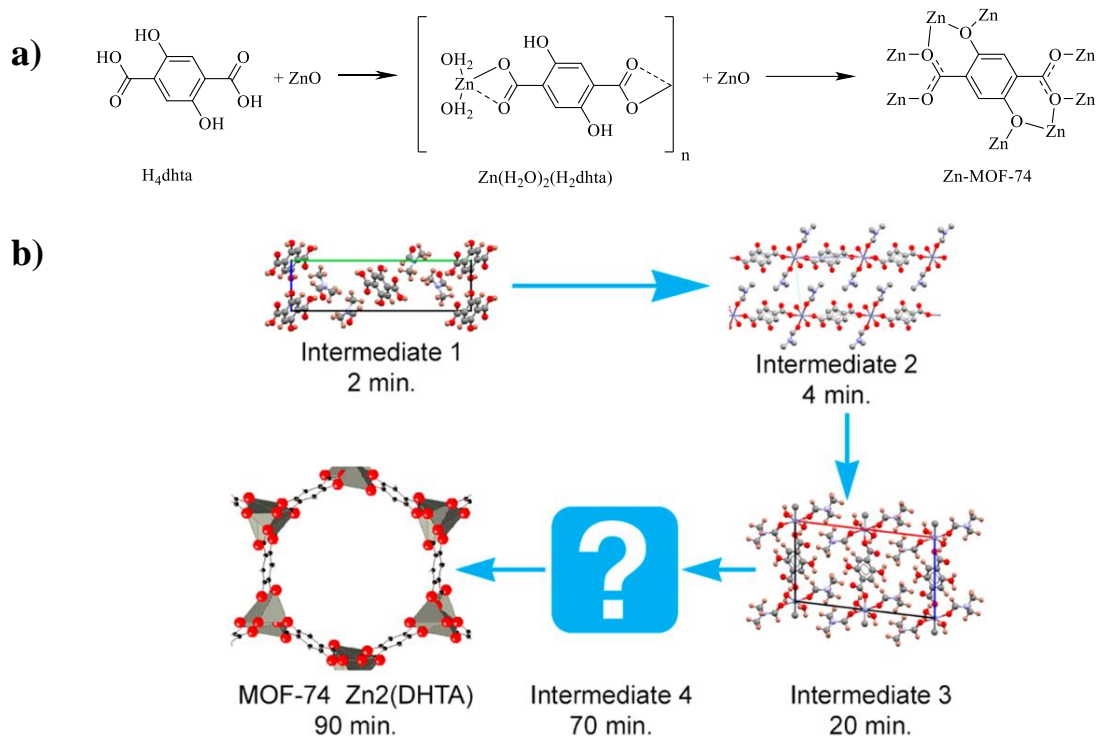


Figure 1. Chemical representation of the MOF-74(Zn) synthesis with respective intermediates during the mechanochemical reaction of H_4DHTA and ZnO (1:2 ratio) in the presence of **a)** a small amount of water and **b)** a small amount of DMF. Reprinted from ^[49], American Chemical Society, licenced by CC-BY 4.0.

In the above-described methods, metal salts have been mixed with organic linker molecules. However, it is possible to use pure metals or more precisely metal ions as in the case of electrochemical synthesis. Electrochemical synthesis can be performed in a batch or continuously and the source of metal ions is the anode.^[50,51] To oxidize a metal at an anode, a certain electric field has to be applied and according to the voltage the oxidation state of the metal can be adjusted. The biggest advantages of electrochemical synthesis are milder conditions and shorter reaction time than in the case of solvothermal synthesis.^[52] However, in order to dissolve the linker molecules, organic solvents have to be used in many cases, which complicates the understanding of the whole process. More to that, organic solvents exhibit usually lower conductivity and, therefore, the position of anode and cathode is crucial for the creation of desired MOF structure.^[53] Nevertheless, structures such as HKUST-1, ZIF-8, MIL-100(Al) and MIL-53(Al) have already been successfully synthesized using an electrical field.^[54] The quality and properties remain in general the same as after the solvothermal synthesis, but one exception – MIL-53(Al) did not show any breathing behavior after adsorption, probably due to the very small size of its crystallites.^[54] Electrochemical synthesis can be also used for the formation of thin layers of MOFs on other materials such as copper alloys.^[55,56]

Among other synthesis techniques belong chemical vapor deposition, which can be used for the synthesis of thin MOF films or coatings^[57–60] and bioinspired syntheses^[61–64] where biomolecules or biomimetic principles are used.

1.2 Isorecticular MOF structures

IRMOFs, short for ‘isorecticular metal-organic frameworks’, are specific types of MOFs known for their uniformity in the crystal structure and pore size while varying in the choice of metal ions and organic linkers.^[65] The term ‘isorecticular’ implies that these MOFs share the same underlying framework or topology, making them a versatile class of porous materials. Characteristic for IRMOFs is a uniform crystal structure, which enables the precise control and predictability of their properties. By varying metal ions and/or organic linkers it is possible to change chemical and physical properties such as the pore size, and thus, making them suitable for accommodating a variety of guest molecules. The most renowned work was presented by Eddaoudi *et al.*^[66] in 2002, where MOF-5-based materials with octahedral ZnO_4 clusters and rigid dicarboxylates were synthesized. The resulting materials were reported as IRMOF-1 to IRMOF-16 and some of the structures are depicted in **Figure 2**.

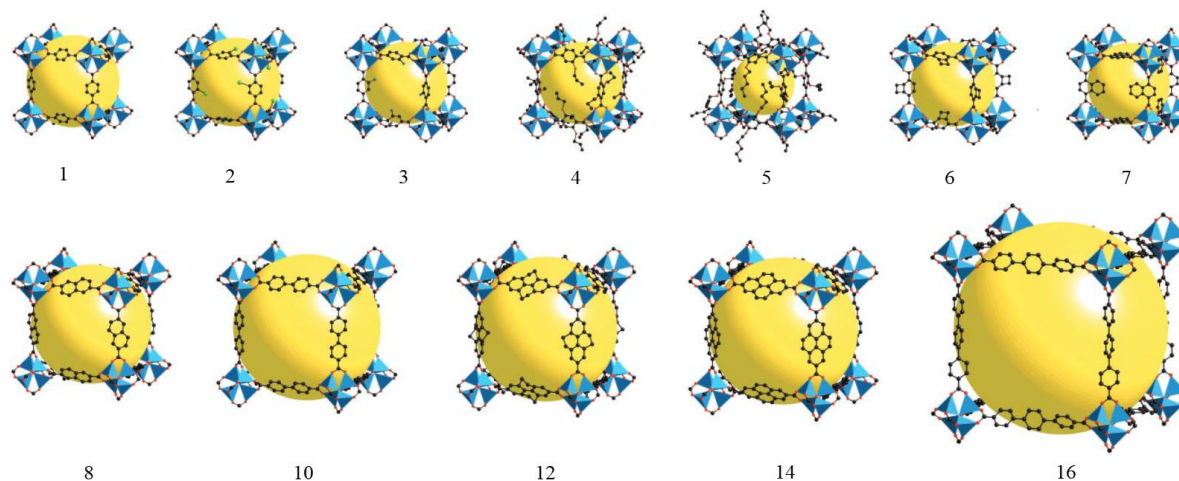


Figure 2. Isorecticular metal-organic frameworks (IRMOF- n where n corresponds to the number under each structure) based on MOF-5 (=IRMOF-1). Blue polyhedra: Zn, black: C, red: O, green in No.2: Br, blue in No.3: nitrogen of NH_2 . The yellow spheres represent the largest van der Waals spheres that would fit in the cavities without touching the frameworks. Reprinted from ^[66] with permission from AAAS.

1.3 Multi-component metal-organic frameworks

Organic linkers and metal centers contribute to the complexity of the materials and each linker or metal can influence the properties of the resulting MOF. To increase the variety even further,

it is possible to incorporate more than one type of linker and/or more than one type of metal into one structure on equivalent positions.^[67] Usually, linkers or metal ions, respectively, of similar sizes are combined to ensure that there is no change in the pore size and lattice structure.^[68,69] These materials are in general called ‘multi-component metal-organic frameworks’,^[47,70,71] or ‘multivariate MOFs’,^[72] or even ‘mixed-MOFs’,^[73,74] and can be divided into two basic groups – mixed-linker MOFs and mixed-metal MOFs (**Figure 3**). In an extreme case, it is also possible to combine mixed-linker and mixed-metal approach in one structure.^[65] The biggest benefit of multi-component materials are tunable properties according to the desired usage – for example, the presence of different active centers in one catalyst^[75–78], shifted thermostability^[79] or the existence of additional functional groups that can influence the gas storage properties.^[80,81]

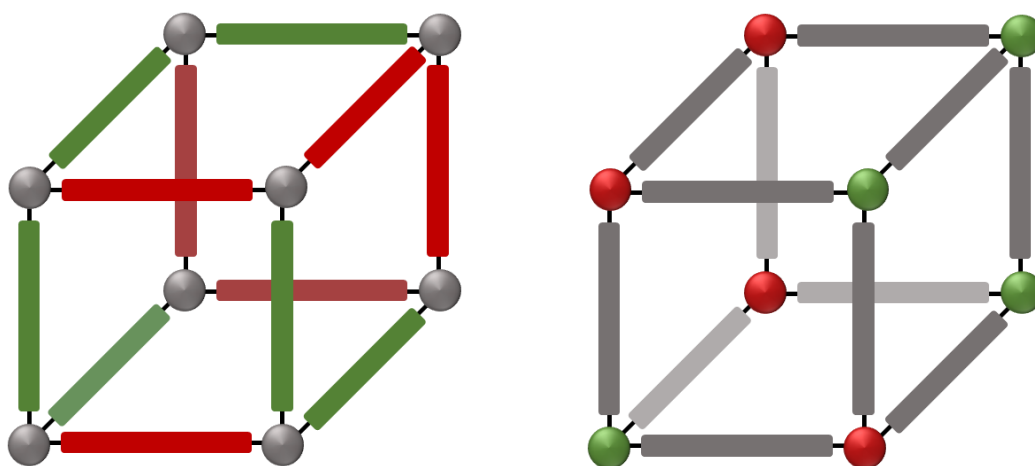


Figure 3. Schematic representation of the mixed-linker (left) and the mixed-metal (right) concept.

Moreover, the multi-component MOFs can also have different arrangements – so-called statistical (or random) distribution and a core-shell distribution. Within a statistically distributed material, both metals (or linkers) are randomly distributed throughout the whole structure, not building any significant domains with only one kind of metal. However, it is very hard to obtain truly statistically distributed samples as in most cases small conglomerates are built.^[82] The core-shell distribution, as the name already describes, is built from a core, in which only one metal (linker) is present, and a shell, where the second metal (linker) can be found. These layers are observable in each particle and the tight contact between the two parts can cause unique properties – unlike in the case of physical mixture of the two components.^[77]

1.3.1 Mixed-linker metal-organic frameworks

Mixed-linker MOFs consist of two or more different linker molecules and the difference between the random distributed and the core-shell structures can be significant. Statistically distributed materials differ mostly only by the presence of additional functional groups on the linker molecule to maintain the original MOF structure.^[79,81,83,84] The synthesis is usually based on solvothermal synthesis, where linkers are mixed with the metal precursors in a reaction flask. It is also possible to post-synthetically incorporate additional functional groups as described in **Chapter 1.4**. In the case of core-shell structures, completely different linkers can be used, creating two different MOFs above each other.^[20,85,86] The synthesis of the core-shell structured mixed-linker MOFs is usually divided into more steps and after each layer or modification the material can be characterized to assure that the crystallinity and other properties are retained.

Truly mixed-linker MOFs (not a physical mixture) are hard to characterize. Traditional characterization techniques (such as PXRD, nitrogen physisorption, IR, NMR etc.) give only a limited insight into the distribution of the linkers. PXRD measurements are used for the identification of crystalline structures and, thus, can at least give an information about the formation of unwanted crystalline phases. More demanding would be a high-resolution PXRD which provides, using lattice constants, an indication about the linker distribution.^[87,88] For example, a physical mixture of MOF-5 and IRMOF-3 shows two distinct reflections at 3.13° (MOF-5) and 3.14° (IRMOF-3). The presence of only one reflection, which is shifted towards a larger angle with increasing amount of the substituted linker indicates the presence of the two linkers in one unit cell.^[74] High resolution PXRD can be performed only at synchrotron facilities, which disables the usage as a routine characterization technique. Moreover, the position of reflections depends on the beam energy and thus, is not the same throughout different facilities. Nevertheless, when the difference between the two linker molecules is significant, even a laboratory PXRD (with some additional equipment) is sufficient for an evaluation according to Vergard's law. For example, Hendon *et al.*^[89] were able to characterize UiO-67 with increasing amount of bipyridine dicarboxylic (BPyDC) linker, showing that the reflection at 26.8° follows precisely a linear shift towards lower angle with an increasing BPyDC amount.

Another useful technique to differentiate between the physical mixture and the mixed-linker distribution can be thermogravimetric analysis or, more precisely, the first derivative of the TG curve (DTG). The basic requirement is that the two linkers have significant difference in thermal stability. Kleist *et al.*^[74] observed in the DTG only one minimum corresponding to the

decomposition of the linker molecules which shifted towards lower temperatures with increasing ABDC amount. However, the higher amount of ABDC linker (above 40 %) in the MIX-MOF led to two minima in DTG which were both assigned to the linker decomposition. The splitting of the minima indicates that the higher amount of ABDC results in a physical mixture of MOF-5 and IRMOF-3, whereas one minimum in DTG corresponds to a mixed-linker material.

A slightly more demanding technique is solid state NMR. The first possibility is to use isotopically labeled linkers.^[90] However, isotope labeling is quite an expensive technique. On the other hand, Krajnc *et al.*^[91] presented the synthesis and characterization of DUT-5 with unfunctionalized biphenyldicarboxylic linker (BPDC) and functionalized BPyDC linker. The crucial condition for this NMR analysis is that at least one of the signals from each linker molecule has to be separated from the rest of the signals and therefore, it would be possible to perform 2D evaluation. Firstly, they had to confirm which signal corresponds to which hydrogen using ^1H - ^{13}C LG-HETCOR experiment and DFT/GIPAW calculation. Computational calculations are demanding but for each system they have to be performed only once. Later on, ^1H spin-diffusion experiments were performed, showing the cross peaks between the two selected hydrogens (one from each linker). These cross-peaks are only visible when the two linkers are in a very close vicinity and therefore, it could be concluded that no clusters were built.

Other characterization techniques can only be used on limited basis. Nitrogen physisorption measurements are hard to evaluate because of the possible presence of solvent molecules in the pores and the synergistic effects of the linkers influencing the adsorption and desorption.^[92] A great amount of techniques can indicate the amount of each linker molecule but cannot contribute to the linker distribution. Into quantitative or semi-quantitative techniques belong among others: IR^[93], UV-VIS^[31] and liquid-phase NMR of the digested sample^[94].

1.3.2 Mixed-metal metal organic frameworks

Two or more metals can be incorporated in the structure in different ways. Either on equivalent positions as nodes of the metal-organic linker or on non-equivalent positions, where only one metal creates the structure and the other metal(s) is bonded at a different location (such as in the pore or on a functional group of a linker or in a different coordination environment). For more details on non-equivalent mixed-metal MOFs see **Chapter 1.4**. Both possibilities could

be, strictly speaking, called as mixed-metal MOFs. However, this term is usually used only for the materials with different metals on equivalent nodes of the structure.

As in the case of mixed-linker MOFs, also mixed-metal MOFs can have different arrangements. Randomly distributed mixed-metal MOFs are usually synthesized *via* direct hydrothermal or solvothermal synthesis, where all metal salts are mixed with the linker at the same time resulting later on in a multimetallic material. With this strategy, materials with up to ten different metals were already synthesized.^[95] However, as Wang *et al.* admit, the amount of each metal can be different due to the different crystal growth rates. More to that, the metals can also build different clusters from nanometer up to micrometer scale. Nonetheless, the direct synthesis is generally used to decrease the costs, whenever this is possible. One of the broadly investigated structure is MIL-53 due to its breathing behavior (see **Chapter 1.5.2**), which can be tuned using different metals.

Core-shell distributions can also be synthesized during one-step synthesis, usually when the solubility of the metal salts or the crystallization rates are very different. Depauw *et al.*^[96] reported the synthesis of an ‘egg yolk’ material with bimetallic Cr/V core and monometallic Cr shell using microwave synthesis. More interestingly, the outcome during classical solvothermal synthesis was the same material with a random distribution. However, in most cases, two-step synthesis is used. In the first step, the core is synthesized and after washing, drying (and characterization) the core is mixed with the new chemicals for the synthesis of a shell. This approach gives a better control regarding the shell growth. It is also possible to adjust the size ratio between the core and the shell.^[77]

There are different elemental analysis techniques to determine the metal ratio such as ICP-OES, AAS or MS. However, elemental analysis is not able to distinguish between the different metal distributions. More to that, the above-mentioned techniques are destructive. It is also not possible to determine whether the metals are incorporated into the backbone of the MOF itself or only as clusters in the pores. As in the case of mixed-linker materials, PXRD and Vergard’s law can be used. Sun *et al.*^[97] reported a Co/Ni-MOF-74 structure where Ni was substituted by Co and a reflection at about 6.8° shifted towards a lower angle. The successful incorporation of Co into the structure was later on confirmed during EXAFS measurements at a synchrotron facility.

In specific cases also IR spectroscopy can be used, usually in the range of 600 cm^{-1} and lower.^[98] However, in this area the bands are often broad and hard to distinguish from each other.

Therefore, IR spectroscopy is of only a limited usage and is not one of the techniques which are often used for mixed-metal MOFs. One of the materials where FTIR can be used is MIL-53(Cr,Fe).^[99] Three bands are observable in the range between 925 and 847 cm^{-1} where the spectra are usually less cluttered. The band at 925 cm^{-1} can be attributed to Cr(m2-OH)Cr OH groups and the band at 847 cm^{-1} to Fe(m2-OH)Fe OH groups. The third band at 885 cm^{-1} is observable only for the bimetallic material and can be assigned to the Cr(m2-OH)Fe moieties, proving the close vicinity of Cr and Fe in the structure.

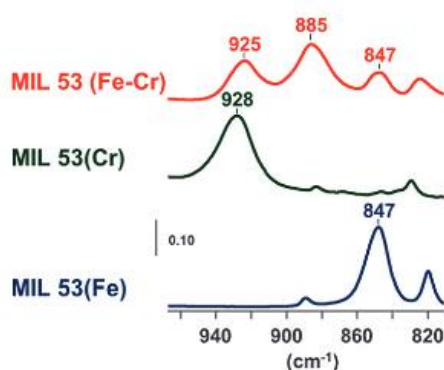


Figure 4. IR spectra of MIL-53(Cr), MIL-53(Fe) and MIL-53(Fe–Cr) outgassed at 423 K in the $\delta(\text{OH})$ range. Used with permission of Royal Society of Chemistry, from ^[99]; permission conveyed through Copyright Clearance Center, Inc.

SEM/EDX (scanning electron microscopy coupled with energy-dispersive X-ray spectroscopy) is one of the most common technique to investigate the metal distribution but it strongly depends on the resolution of the device. In general, the resolution can go down to nm area, which has both advantages and disadvantages. With a better resolution, it is possible to determine whether the metals are randomly distributed. On the other hand, only few particles are investigated and therefore, it is very hard to determine the distribution for the whole sample. Still, SEM/EDX is one of the few standard methods in which core-shell distribution can be observed as, for example, in the case of the core-shell Co-MOF-74@Mn-MOF-74.^[77] More to that, it is also possible to see the differences in the shell thickness depending for example on the time of the reaction or amount of chemicals used for the shell. This information can be crucial for the catalytic reactions later on. Similar method is TEM/EDX (transmission electron microscopy with energy-dispersive X-ray spectroscopy) which can reach even better resolution.

1.4 Post-synthetic modification (PSM)

One-step synthesis is preferred as it is the cheapest and also the most sustainable way of a MOF production. However, mostly due to the instability, size or reactivity of the linker, it can be challenging or even impossible to obtain certain MOF structures. Because of that, post-synthetic modification reactions are used. The principle of PSM is the subsequent modification of an already existing structure, retaining its framework topology. Among the various PSM techniques, covalent and dative PSM are two prominent approaches that allow for the introduction of functional groups or structural modifications within MOFs.^[100] During the covalent PSM a new covalent bond is created. Usually it is applied on the linkers^[101–104] but also PSMs on the metal centers have been reported.^[105] The suitable groups for covalent PSM are for example aldehyde groups and amine groups. Amine group PSMs are in detail described in **Chapter 1.4.3**. The covalent bond formation can lead to an enhanced stability and tailor-made properties, such as improved gas adsorption, catalytic activity, or selectivity in separations.^[106] Covalent PSM offers a greater structural control but may lead to a reduced porosity. Dative PSM, on the other hand, is characterized by the formation of coordinative bonds, which can form on a SBU or on a linker molecule.^[103] Regarding the SBU, we are usually talking about the desolvation and subsequent immobilization of other molecules, such as pyridine.^[107,108] Also linker molecules (such as bipyridine linkers) can serve for the dative post-synthetic modification where the metal is bound directly to the linker molecules (see **Chapter 1.4.2**). This approach allows for the incorporation of guest species in a reversible and dynamic manner. Dative PSM can be used to modulate the pore size, guest-host interactions, and guest release kinetics, making it a versatile strategy for various applications.^[103,109,110] Dative PSM maintains the MOF's inherent porosity but sacrifices some control over structural modifications.

A special case of post-synthetic modification is the post-synthetic deprotection and the post-synthetic exchange (**Chapter 1.4.1**). The post-synthetic deprotection is used in cases, where the group has to be protected during the formation of the MOF structure mostly due to its high reactivity. During the post-synthetic reaction, the protecting group is detached, and thus, the material is activated, for example for catalytic reactions.^[111–113]

1.4.1 Post-synthetic exchange

Post-synthetic exchange is one of the easiest PSM reaction and can be done for both linkers and metals. Linkers and metals of similar size as the original ones in the structure are mostly used.

The schematic representation of the post-synthetic metal exchange (PSME) is shown in **Figure 5a**). The original MOF structure is mixed with a dissolved metal salt and the metal centers exchange after some time.

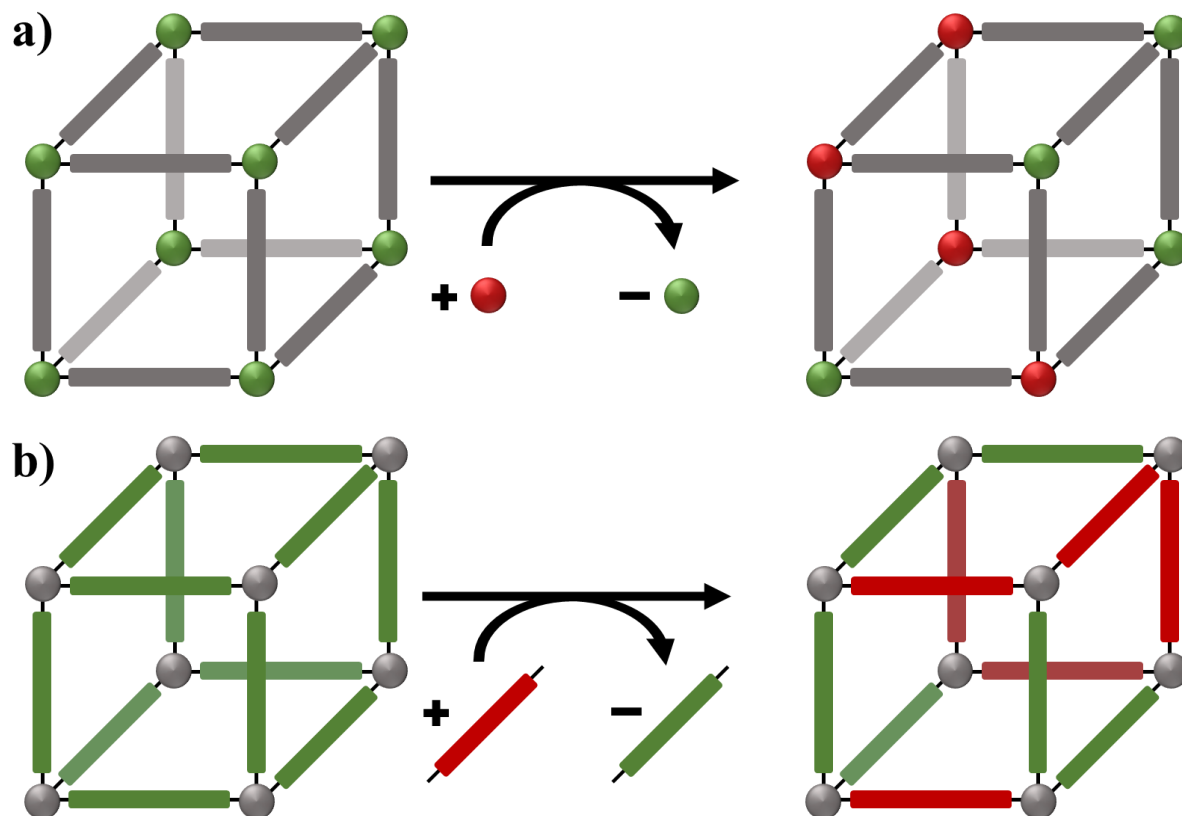


Figure 5. Schematic representation of a) post-synthetic metal exchange and b) post-synthetic linker exchange.

The reaction time can influence the amount of exchanged metals and up to all metal centers can be exchanged.^[114] Moreover, it can also lead to the creation of a core-shell structure, where the initially used metal is present only in the core and the post-synthetically incorporated metal is partially or fully present in the shell.^[115] However, during PSM unwanted oxide-phases can arise and the crystallinity can decrease^[116] or the MOF structure can collapse. One successful example of post-synthetic metal exchange is Co/Ni-MOF-74.^[97] The starting material Ni-MOF-74 was inactive for cyclohexene oxidation and, therefore, cobalt was incorporated onto positions, which were later more accessible for the substrate. The resulting material showed superior catalytic activity over the pure Co-MOF-74 maintaining the crystallinity and porosity of the parent MOF, but showing a synergistic effect between cobalt and nickel. The choice of metal can also have an influence on specific properties, such as flexibility and porosity as presented for DUT-49.^[117] Depending on the metal centers, the structure can change from not flexible (Zn), towards flexible (Ni) ending with a special phenomenon called ‘negative gas

adsorption' (Cu). During adsorption experiments the structure contracts, which then results in the release of the excess adsorbate molecules from the pores. DUT-49(Cu) can be synthesized also during classical solvothermal synthesis but the crystallites that are formed during the direct synthesis are smaller and, thus, the characterization based on the crystal size is more complicated.

PSLE – post synthetic linker exchange (**Figure 5b**) is not that widely used as the PSME and is also mostly combined with other subsequent reactions.^[118–121] One of the reasons is the complicated characterization of the linker distribution. Usually, X-ray photoelectron spectroscopy or the energy-dispersive X-ray spectroscopy are used but the disadvantage of these methods is their limited sampling volume and also limited information depth or resolution. An article about the usage of Rutherford backscattering spectrometry (RBS) for UiO-66, which was exchanged with 2-iodobenzene-1,4-dicarboxylate (I-bdc), was published in 2017.^[119] This non-invasive method detects the energy of the highly energetic ions after they have been elastically scattered due to the Coulomb potential of the sample nuclei (Rutherford scattering). This method can reach few μm below the surface, which is usually enough for the MOF particles and enables to investigate the linker distribution in the material. The disadvantage of RBS is that it requires heavier elements ($Z > 30$) which significantly limits the usage for most post-synthetic linker exchanged cases reported in the literature. The authors were able to calculate the amount of the newly incorporated linker referenced to Zr centers of UiO-66. This information is complementary to ^1H NMR of the digested sample which gives information on the total linker amount. Moreover, they were able to prove that the exchanged linker was statistically distributed throughout the whole material and the migration of I-bdc through the UiO-66 crystal proceeds faster than its incorporation.^[119]

1.4.2 Immobilization of metals on linker molecules

Besides functional groups that bind to SBUs, the linker molecule can also exhibit additional functional groups. One of the commonly used linkers are those with chelating groups (such as bipyridine^[122–124], thioether^[125], porphyrin^[126] or N-heterocyclic carbene^[127]) at which additional metals are immobilized. The principle is schematically represented in **Figure 6**.

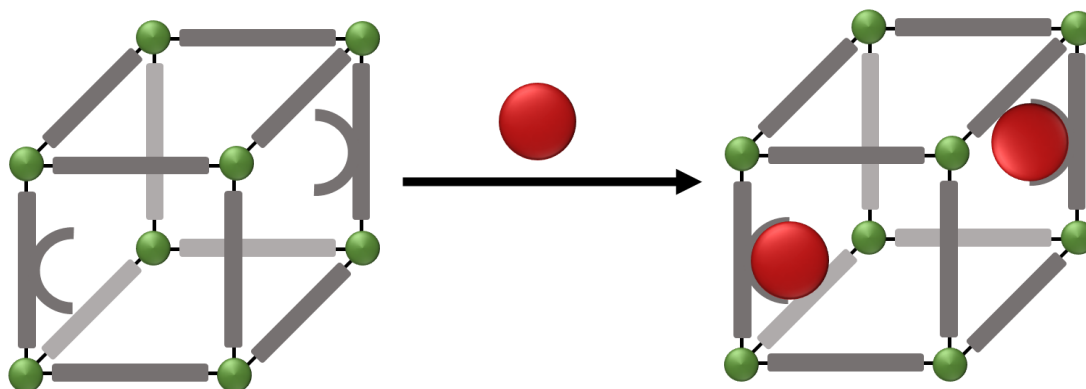


Figure 6. Schematic representation of the immobilization of metals ions at linker molecules.

One of the work on this topic was presented by Lin and co-workers in 2005.^[128] Chiral bridging ligand (R)-6,6'-dichloro-2,2'-dihydroxy-1,1'-binaphthyl-4,4'-bipyridine (**Figure 7**) was used to immobilize octahedrally coordinated Cd(II) centers, leaving the dihydroxy functional groups for subsequent $\text{Ti}(\text{O}^i\text{Pr})_4$ immobilization. The resulting catalyst exhibited a very high degree of conversion (often above 99 %) and enantioselectivity (around 80 %) towards additions of ZnEt_2 to aromatic aldehydes.

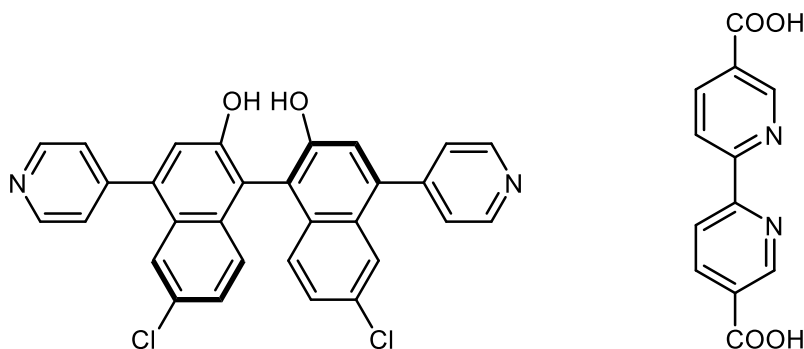


Figure 7. (R)-6,6'-dichloro-2,2'-dihydroxy-1,1'-binaphthyl-4,4'-bipyridine and 2,2'-bipyridine-5,5'-dicarboxylate linkers used for the direct immobilization of metals.

Relevant for this thesis is 2,2'-bipyridine-5,5'-dicarboxylate as a linker (**Figure 7**), which forms MOF-253 structure and was already many times used for post-synthetic metalation with Pd, Co or Ru ions.^[122,124,129–131] However, in the case of MOF-253 an interesting phenomenon occurred. Carson *et al.*^[132] immobilized 7 % and 13 % of ruthenium on MOF-253. Even though, in both cases the post-synthetically modified material exhibited similar crystallinity according to PXRD, the calculated specific surface area for MOF-253-Ru13% was only 80 m^2/g which is in contrast to the material with $S_{\text{BET}}(\text{MOF-253-Ru7\%}) = 1145 \text{ m}^2/\text{g}$. The pores of the MOF-253-Ru13% were probably blocked by ruthenium complexes at the pore mouth and nitrogen could not enter the pores. Also the catalytic activity of the material, which was tested firstly using

1-phenylethanol and then other alcohols as substrates, showed that lower Ru loadings and higher surface areas were significantly more active as oxidation catalysts (TON of 1980) than samples with high Ru loadings and low surface areas.

1.4.3 Post-synthetic modification of amine-functionalized MOFs

Chelating groups can be also incorporated into the structure during post-synthetic modification using amine-tagged or aldehyde-tagged linkers. Amine-tagged linkers are one of the most commonly used functionalized linkers as they are often commercially available and they can be easily incorporated into the structure. After the synthesis, amine groups are also easy to modify during the following post-synthetic steps (for schematic representation of the reaction see **Figure 8**). In 2007, Wang and Cohen^[102] published a communication about IRMOF-3 with 2-amino-1,4-benzenedicarboxylic (ABDC) linkers which were covalently modified using acetic anhydride, predicting that similar PSM reactions will gain in importance in the next few years. Indeed, anhydrides (such as acetic anhydride, maleic anhydride, crotonic anhydride etc.) became popular and were used in several MOF structures.^[133–138]

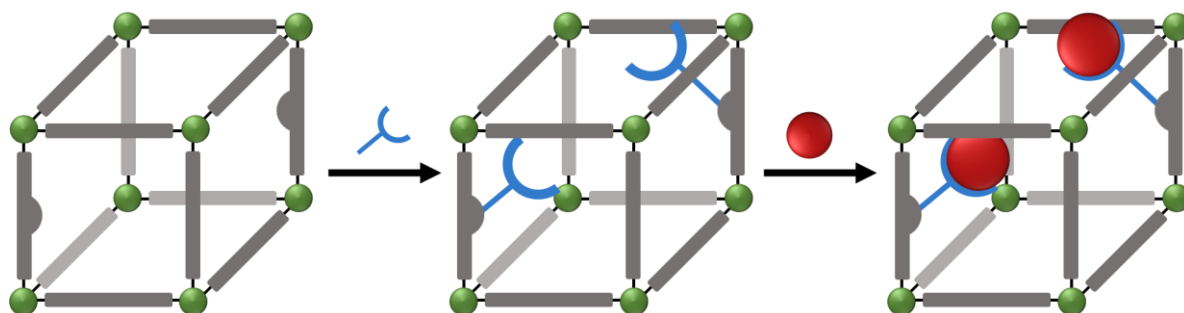


Figure 8. Schematic representation of the incorporation of chelating groups and subsequent immobilization of metal ions in amine-functionalized MOFs during post-synthetic modification.

2-Amino-1,4-benzenedicarboxylic acid was also used in two other MOF structures besides IRMOF-3, namely DMOF-1-NH₂ and UMCM-1-NH₂.^[139] During the post-synthetic modification, chain anhydrides of different length and branched anhydrides were used and the resulting materials were investigated regarding the degree of modification, as well as their thermal and structural stability and porosity. All PSM materials retained their crystallinity and thermal stability regardless of the used anhydride. Within the UMCM-1-NH₂ material, the porosity was dependent on the length of [CH₃(CH₂)_nCO]₂O, where **n** = 0, 2, 4, 8, 12, 18. Longer or more branched aldehydes resulted in lower specific surface area/porosity of the resulting structure. However, even the lowest measured specific surface area (~2800 m²/g) indicates that the MOF remained highly porous after the anhydride incorporation. This can be explained by

the two different pore-openings in the structure of UMCM-1-NH₂. As the small pore-openings consists of amine-modified linkers, the anhydrides coordinate there, leaving the larger pore openings accessible for nitrogen molecules. For DMOF-1-NH₂, the results of nitrogen physisorption measurements varied broadly and no simple trend could be observed. The degree of aldehyde modification, on the other hand, followed the same trend for both materials. The highest modification degree was observed for small anhydrides, where almost 100% of NH₂-BDC were modified. The degree of modification then decreased with the length and the complexity of the anhydride molecules.^[139]

Post-synthetically incorporated cyclic anhydrides can afterwards be used as chelating groups for the immobilization of additional metals if the ring is opened during the reaction. The resulting MOF materials then exhibit at least two different metal species on non-equivalent positions (one at the SBU and the other attached to linker molecule). For instance, in the Kleist group, MIL-53-NH₂(Al) was in the first step post-synthetically modified with maleic anhydride and in the second step Pd(II) ions were chelated into the structure.^[135] The resulting catalyst was then tested in Heck-type coupling reactions of aryl halides with styrene where they exhibited high catalytic activity. Unlike commercially used catalysts, MIL-53-NH₂(Al)-Mal-Pd is a heterogeneous catalyst which provides additional advantages during the catalytic reactions (for more details about heterogeneous and homogeneous catalysis see **Chapter 1.8**).

In addition to this procedure, the presence of anhydride groups in MOF materials can be also obtained using other methods than the post-synthetic modification of amine-tagged linkers. MIL-121 provides two COOH groups that are not coordinated to the SBU and point towards the pores. As the pores are blocked by these carboxylic acids, the material exhibits low specific surface area. When treated at 440 °C for 16 hours, the structure partially collapses and the free COOH groups condensate creating anhydrides and hierarchical HMIL-121 arise. The resulting material is highly porous and the anhydride groups can react with a great variety of different moieties such as alcohols, aromatic amines or metal complexes.^[140]

1.5 Metal-organic frameworks with terephthalate-based linkers

Terephthalate-based linkers are very versatile and together with various SBUs they can create MOFs with diverse pore shapes and properties. Among others, terephthalate linkers are used in **MOF-5** together with zinc-oxo clusters building cubic structure (**Chapter 1.5.1**), in **MIL-53**

with aluminum metal centers creating structures with breathing properties (**Chapter 1.5.2**) and in **CPO-27** with hexagonal pore shape and different metal centers (**Chapter 1.5.3**).

1.5.1 MOF-5

MOF-5 was firstly introduced by the group of Yaghi in 1999 and consists of benzene-1,4-dicarboxylate (BDC) and tetrahedral Zn_4O units creating a 3D cubic structure (**Figure 9**).^[18] The structure is synthesized during a solvothermal synthesis in DMF and chloroform. After the synthesis, it is possible to exchange the adsorbed DMF molecules with volatile chloroform. Chloroform guests can be removed from the structure at room temperature leaving a highly porous and crystalline material with a Langmuir surface area of 2900 m²/g and a thermal stability around 450 °C. These properties make MOF-5 valuable for catalysis as well as for hydrogen storage.^[18,141] However, MOF-5 exhibit limited stability to moisture and acidic/basic environments which lead to structural degradation over time.

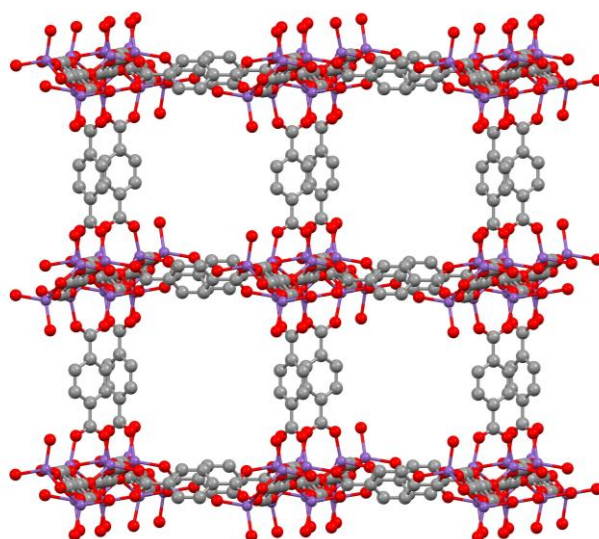


Figure 9. Schematic representation of MOF-5 structure. Grey: carbon, red: oxygen, violet: zinc.

The versatility of MOF-5 material was demonstrated for a zinc-manganese system (Mn:Zn ratio of approximately 1:15), which was used as a precursor for a catalyst that was active in olefin epoxidation.^[142] During the PSM reaction of Mn^{II} -MOF-5 with *tert*-butylsulfonyl-2-iodosylbenzene the oxidation state of manganese changed to +III creating $Mn^{III}(OH)$ -MOF-5. The incorporation of Mn^{2+} cations into MOF-5 had no influence on the catalytic reactivity but after the reaction with *tert*-butylsulfonyl-2-iodosylbenzene the resulting material was very active in the selective epoxidation of cyclic alkenes such as cyclopentene or norbornene.^[142] Beside the example mentioned above, also in this structure amino-tagged linkers can be used

for the creation of mixed-linker material with post-synthetically incorporated metals, such as palladium.^[47]

1.5.2 MIL-53

This metal-organic framework with the structure formula $M^{III}(OH) \cdot \{O_2C-C_6H_4CO_2\} \cdot \{HO_2C-C_6H_4-CO_2H\}_{0.75}$ was firstly introduced by the group of Férey in the year 2003.^[143,144] MIL-53 derives its name from the Matériaux de l'Institut Lavoisier, and the structure is composed of terephthalic linkers bridged by the metal centers which are octahedrally coordinated by six oxygen atoms (**Figure 10**). Metal centers are usually trivalent metals such as Al^[145], Cr^[143], Fe^[146], Ga^[147], In^[148], Sc^[149,150] or V^[151,152]. The structure has been extensively studied due to its unique structural flexibility, which allows it to undergo reversible structural transitions in response to changes in temperature or external stimuli and is called the breathing effect. The crucial condition of a breathing effect is that the framework topology is retained, and no chemical bonds are broken or created and only the pore dimensions change.^[145,153]

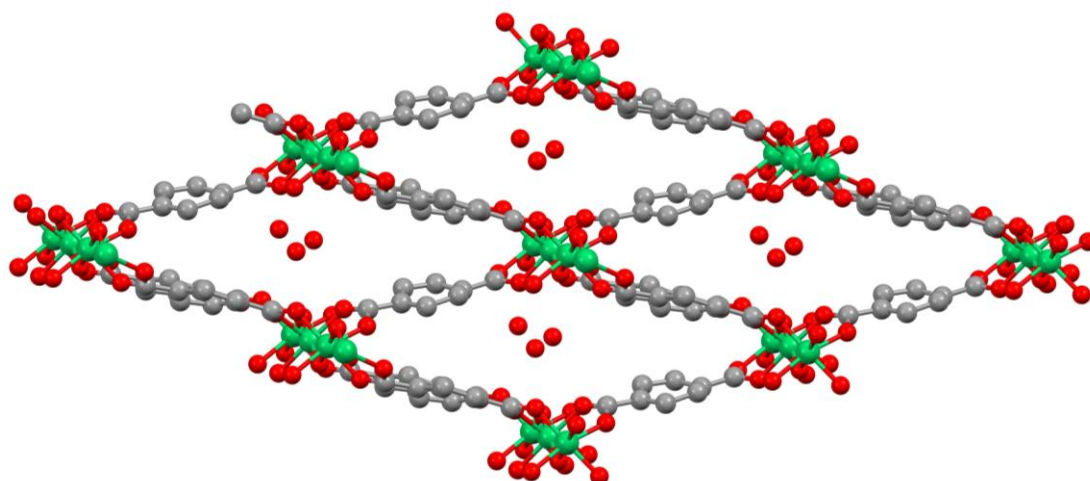


Figure 10. Schematic representation of the MIL-53 structure. Grey: carbon, red: oxygen, green: aluminum.

Not only external stimuli have an effect on the breathing behavior – already the solvent chosen during the synthesis can have an impact as shown for MIL-53(Al).^[6] MIL-53(Al) is usually synthesized using a hydrothermal synthesis and the resulting material occurs in a narrow pore (*np*) form. Upon adsorption of CO₂ the pores transform into a large pore (*lp*) form. However, it does not breathe in the presence of molecules such as methane. On the other hand, the synthesis with DMF at 120 °C leads to a material with rigid pores already in *lp* form. Such a material showcased no breathing effect but exhibits higher CO₂ adsorption in the 1-20 bar range.^[6]

MIL-53 is a MOF structure which is very often used for the synthesis of bimetallic materials such as Al/Cr^[154], Al/Fe^[155], Al/Ga^[156], Al/V^[157], Cr/Fe^[99], Cr/V^[96], Co/Fe^[158], Fe/Ni^[159] or Fe/V^[160]. Each of these materials have unique properties and usage featuring better performance than the respective monometallic materials. For example, MIL-53(Al,Fe) was investigated as a catalyst in the selective oxidation of H₂S to elemental S.^[161] Monometallic MIL-53(Al) exhibited a yield towards S of only 50 % and MIL-53(Fe) around 70 %. MIL-53(Al,Fe) showed a superior catalytic activity and also stability with a S yield of nearly 100 % and stability for 30 hours. The authors also found out that the conversion to H₂S increased with decreasing Al/Fe ratio and, thus, only a minor amount of aluminum (17 %) in MIL-53(Fe) could have a massive impact on the catalysis.^[161]

1.5.3 CPO-27

CPO-27, also known as MOF-74, is a 3D structure consisting of tetrahedral metal clusters connected by 1,4-benzenedicarboxylate (BDC) linkers creating a hexagonal pore shape. The metals are in +II oxidation state and each metal is bound to two hydroxyl groups and to three carboxylate groups. The last coordination site is occupied by a solvent molecule (**Figure 11**).^[162] CPO-27 was introduced in the year 2005 together with 13 other metal-organic frameworks with rod-shaped secondary building units.^[162]

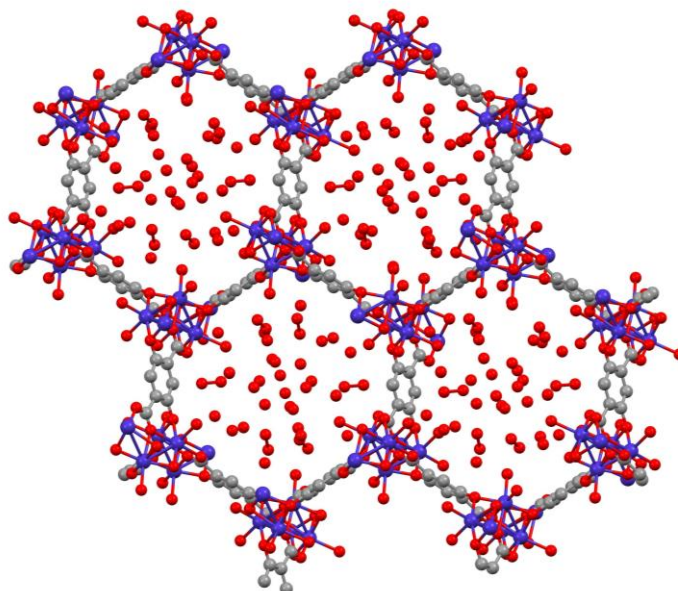


Figure 11. Schematic representation of the CPO-27 structure. Grey: carbon, red: oxygen, dark blue: iron.

The synthesis included dissolving of the zinc salt and the linker in DMF, 2-propanol and water and freezing of the reaction mixture. After evacuation, the tube was flame-sealed, and heated

to 105 °C for 20 hours.^[162] Since then, CPO-27(M) was synthesized by many different ways for example using microwave synthesis^[163] or water-based synthesis at room temperature.^[164] CPO-27(M) is a very versatile material, which was already synthesized with various metals such as Co^[78,164–166], Cu^[78,165], Fe^[163,167], Mg^[78,164,166,168], Mn^[78,166], Ni^[78,164,166] or Zn^[78,164–166]. Each of the material exhibits slightly different values in pore volume or specific surface area, but generally the pore volume is listed around 0.5 cm³/g and the specific surface area varies between 1300 and 1600 m²/g.^[163,164,168] CPO-27 is also often used for the synthesis of bimetallic materials with statistical distribution such as ZnCo,^[169] MnCo^[170] or FeCo^[171] and even with a core-shell structure (CPO-27(Co)@CPO-27(Mn)).^[172] An interesting behavior regarding the adsorption isotherms was described for some monometallic as well as bimetallic materials. The CPO-27 materials possessed a hysteresis loop in the mesoporous region, which was associated with the formation of intercrystalline porosity and with the agglomeration between particles.^[78,166]

The CPO-27 structure contains solvent molecules at the last coordination site but the solvent can be evaporated at elevated temperature without destroying the structure. Therefore, it is a versatile material, which was already used in different chemical fields such as gas adsorption, gas separation or catalysis. CPO-27(Fe) was for example used in the phenol hydroxylation using H₂O₂ as an oxidant.^[167] In this study, the temperature was varied between 10 °C and 50 °C. The optimized temperature was 20 °C, as higher temperatures led to a competitive decomposition of H₂O₂. However, the degree of phenol conversion remained almost constant regardless the temperature of the reaction mixture. The same catalyst was used three times without showing any decrease in activity. Compared to previously used catalyst, CPO-27(Fe) was more active.^[167]

1.6 Metal-organic frameworks with 4,4'-biphenyl-dicarboxylate-based linkers

In this chapter, three different metal-organic structures based on 4,4'-biphenyldicarboxylate (BPDC) linkers and their analogs will be presented. **DUT-5** consisting of [Al(OH)]_n chains bridged by BPDC linkers, **MOF-253** where [Al(OH)]_n chains are connected by 2,2'-bipyridine-5,5'-dicarboxylate linker (BPyDC) and **UiO-67** where 4,4'-biphenyldicarboxylate and Zr oxoclusters are used as building materials.

1.6.1 DUT-5

DUT-5, named after Dresden University of Technology, was first introduced in 2009 by the group of Kaskel.^[173] This MOF is synthesized using a classical solvothermal synthesis, where $\text{Al}(\text{NO}_3)_3 \cdot 9\text{H}_2\text{O}$ is mixed with 4,4'-biphenyldicarboxylic acid dissolved in DMF, sealed in an autoclave or a sealed flask and heated at elevated temperature for 24 hours. In the resulting structure, aluminum is coordinated by six oxygen atoms and the axial positions of the octahedra are occupied by hydroxyl groups (**Figure 12**). The resulting MOF has a rigid 3D structure with one-dimensional pores of approximately $19.2 \times 22.7 \text{ \AA}$.^[173]

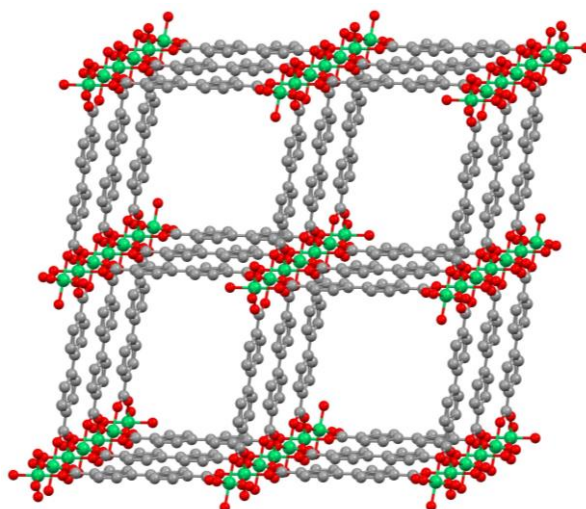


Figure 12. Schematic representation of the DUT-5 structure. Grey: carbon, red: oxygen, green: aluminum.

Solvent molecules can be easily removed from the pore and according to TGA data the structure is thermally stable up to $430 \text{ }^\circ\text{C}$. Another characteristic property is a type I isotherm corresponding to microporous materials and a high specific surface area of $S_{\text{BET}}=1600 \text{ m}^2/\text{g}$.^[173]

More to that, using different types of functionalized linkers it is possible to alter the properties of a parent MOF. Regarding the direct synthesis of functionalized DUT-5, Couck *et al.*^[174] used 2,2'-sulfone-4,4'-biphenyldicarboxylic acid to insert SO_2 groups at the pore walls. The novel material showed a shape selectivity in the adsorption of linear alkanes, unlike pristine DUT-5 which was not selective regarding linear, branched and iso-alkanes. Also post-synthetic modifications of DUT-5 have been reported. In 2015, the Kleist group presented the synthesis of amine-, alkyne- azide- and nitro-functionalized DUT-5 and the possibility to incorporate chelating groups such as salicylaldehyde or maleic anhydride.^[175] Later on, different metals were incorporated into the structure using these chelating groups to synthesize unique single-site catalysts for epoxidation reactions.^[176] Also chiral molecules, such as L-proline can be

introduced into the structure.^[94] Even though, amino acids have not high resistance towards chemicals and elevated temperatures it was possible to use them repeatedly in the aldol reaction of 4-nitrobenzaldehyde and acetone at a slightly elevated temperature of 30 °C.

Not only mixed-linker or mixed-metal ‘mono-structured’ MOF materials can be interesting for industrial usage. Recently, an article by Zhou *et al.*^[177] was presented, where the authors combine DUT-5 and BiOBr (bismuth oxybromide) to obtain a flower-like composite which exhibited high photocatalytic activity and was even reusable maintaining its stability. They used the beneficial properties from both materials – the large porosity, thermostability and low density of DUT-5 and high the catalytic activity in photocatalysis of BiOBr.

1.6.2 MOF-253

MOF-253 is an analogy to the previously introduced DUT-5 and the synthesis conditions are also very similar. $\text{AlCl}_3 \cdot 6\text{H}_2\text{O}$ and 2,2'-bipyridine-5,5-dicarboxylic acid (BPyDC) are dissolved in *N,N*-dimethylformamide and reacted at 120 °C for 24 h, which results in a white powdered material. The MOF is microcrystalline, with a specific surface area of $S_{\text{BET}} = 2160 \text{ m}^2/\text{g}$ and a thermal stability up to 400 °C. Aluminum is coordinated by six oxygen atoms and the axial positions of the octahedra are occupied by hydroxyl groups (**Figure 13**), as the structure is isorecticular to DUT-5.^[124]

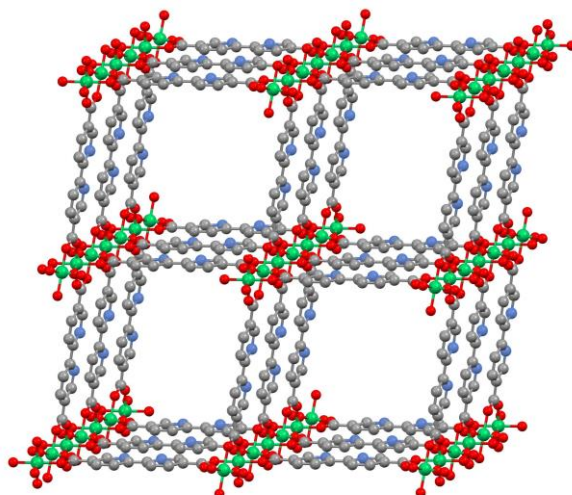


Figure 13. Schematic representation of the MOF-253 structure. Grey: carbon, red: oxygen, blue: nitrogen, green: aluminum.

MOF-253 has a rigid 3D structure with one-dimensional pores and open bipyridine sites, which are mostly used for the direct immobilization of metals such as palladium,^[129,130] copper^[122,130]

and ruthenium.^[131] The principle and examples of post-synthetic immobilization of metals were discussed in **Chapter 1.4.2**.

1.6.3 UiO-67

In 2008, Cavka *et al.*^[178] firstly presented a Zr^{IV}-based UiO-67 with 4,4'-biphenyldicarboxylate linker. Unlike the previously mentioned structures, UiO-67 has two different types of pores – tetrahedral pores with a pore diameter of 16 Å and octahedral pores with a pore diameter of 12 Å (**Figure 14**). However, the pore opening is only ca. 8 Å wide and therefore, the diffusion of substrates is limited.

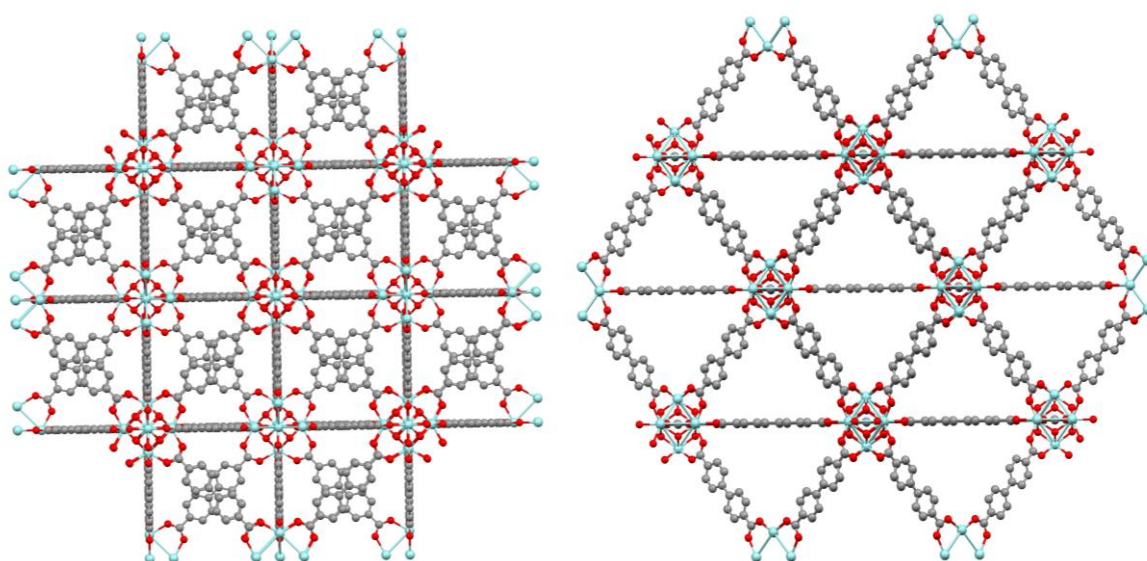


Figure 14. Schematic representation of the UiO-67 structure. Grey: carbon, red: oxygen, light blue: zirconium.

UiO-67 is a very stable MOF with a thermal stability up to 540 °C, resistance towards solvents (such as acetone, DMF or water) and mechanical pressure. The Langmuir surface area of UiO-67 was $S_{\text{Langmuir}} = 3000 \text{ m}^2/\text{g}$. The same stability and resistance is also characteristic for the isorecticular UiO-66 with shorter linker chain (benzene-1,4-dicarboxylate) and also for UiO-68 with elongated linkers (p-terphenyl-4,4''-dicarboxylate). One of the properties, which is changing with the elongation of the linker molecule, is the Langmuir surface area – for UiO-66 $S_{\text{Langmuir}} = 1187 \text{ m}^2/\text{g}$ and for UiO-68 $S_{\text{Langmuir}} = 4170 \text{ m}^2/\text{g}$.^[178] As in the case of MOF-253, the linker molecule can be substituted with the bipyridine analog.^[179,180] Interestingly, a mechanochemical synthesis in a ball-mill with only a very low amount of methanol and DMF was reported for this material. However, as the authors admit, the specific surface area and the also crystallinity was significantly lower in comparison with the classical

solvothermal synthesis due to friction.^[179] Beside that, UiO-67 with amine-^[36,181] and nitro-^[181] functionalized linkers were reported.

1.7 MOF-mediated synthesis of heterogeneous catalysts (controlled decomposition of MOFs)

MOF-mediated synthesis is a process, where parent MOFs are pyrolyzed under an inert, reducing or oxidative atmosphere to produce MOF-derived nanostructures.^[182] The advantages of resulting nanomaterials are that they remain highly porous, the active sites are accessible and, depending on the MOF precursor, the size, shape, and morphology of the nanostructures can be tuned. For example, bimetallic MOF materials can be used for the synthesis of catalytically active materials with specific metal distributions such as segregated, statistically distributed or even core-shell-structured (**Figure 15**). Pyrolysis also enables a higher thermal stability of the resulting catalysts compared to the corresponding MOF, thereby extending the range of possible applications.

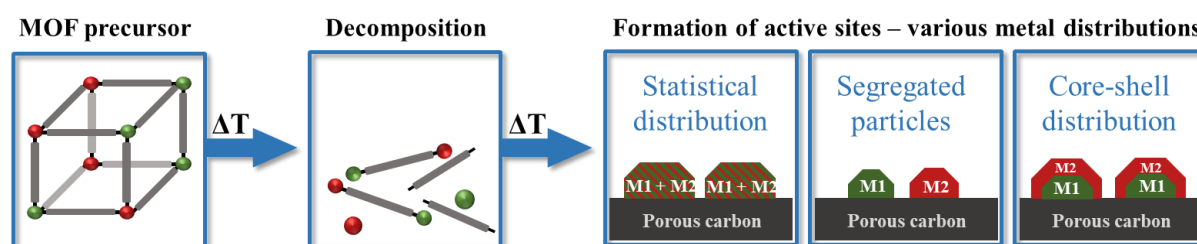


Figure 15. Schematic representation of MOF-mediated synthesis.

The main disadvantage of materials obtained via MOF-mediated synthesis is the high cost, as linker molecules can be expensive and the total amount of material is massively reduced during pyrolysis.^[183] However, the resulting novel materials can be used in various fields, including sensing, gas storage, catalysis and medicine, often with a superior performance than other conventionally produced nanomaterials.^[184–186]

Amali *et al.*^[187] presented the synthesis of ZIF-8, which was prepared by a sonochemical approach, and its subsequent carbonization at 500 °C under argon atmosphere. The resulting carbon nanorods showed excellent solubility in water which is essential for biologically motivated works. Moreover, the synthesized material exhibited a strong and stable luminescence, which, together with the ability to identify the diseased cells, opened the applications of these MOF-derived carbon nanorods in the field of biosafe fluorescent patterning.^[187] Also CPO-27 structures, have been used several times in MOF-mediated

syntheses.^[188,189] In the year 2020, a N-doped porous carbon-supported Ni catalyst was prepared using a CPO-27(Ni) precursor loaded with furfuryl alcohol followed by NH₄OH treatment and pyrolysis under nitrogen atmosphere.^[190] The resulting material was compared with a material prepared by direct pyrolysis of CPO-27(Ni) and catalytically tested in the hydrodechlorination of 1,2-dichloroethane to ethylene in the gas phase. For both materials, the pyrolysis temperature had a direct impact on the carbon content and the growth of Ni particles, but regardless of the decomposition temperatures, the N-doped porous carbon-supported Ni catalyst was ca. 1.5 times more active than pyrolyzed CPO-27(Ni). The selectivities of all catalysts towards ethylene were above 95 %.^[190]

1.8 Metal-organic frameworks as catalysts in liquid phase oxidation reactions

Metal-organic frameworks have been used as catalysts in many liquid phase as well as gas phase reactions because they combine the advantages of both heterogeneous and homogeneous catalysis. On the one hand, they are highly active, highly reproducible and possess high selectivity, which are the advantages of homogeneous catalysts. On the other hand, MOF catalysts can be easily separated from the reaction mixture and can be used repeatedly, which are the advantages of heterogeneous catalysts. The active sites can be located at different positions within the framework – on the metal centres in the form of unsaturated metal sites or functionalized open metal sites (**Figure 16a**), on linker in the form of linker molecules *via* modification of organic linkers with functional groups (**Figure 16b**), or encapsulated in the pores (**Figure 16c**).^[191] The last approach (encapsulation in the pores) is the only approach which does not result in single-site catalyst.

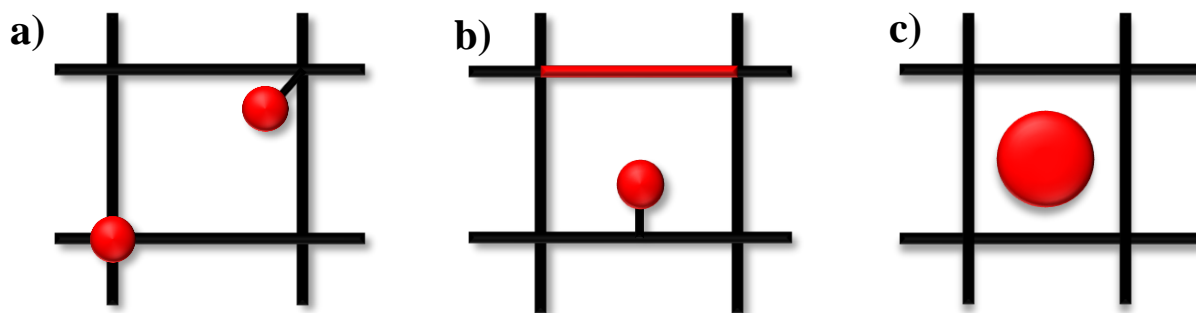
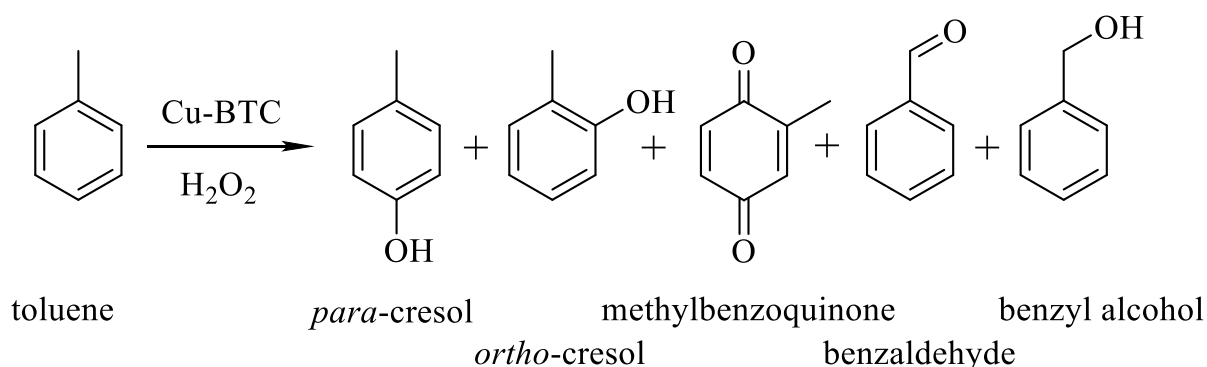


Figure 16. Schematic representation of possible locations of active sites in metal-organic frameworks. **a)** unsaturated metal site or functionalized open metal site; **b)** linker molecule with functional group or post-synthetically modified linker; **c)** encapsulation in the pores.

Liquid phase oxidation reactions are among the most important industrial processes, e.g., in the production of drugs, vitamins and also fragrances. In the recent years, the demand for green chemistry is increasing and therefore, oxidizing agents such as hydrogen peroxide and molecular oxygen from air are used more widely.^[192] However, for the activation of molecular oxygen highly active catalysts are required. In many companies Cr(VI) or Mn(VII) catalysts are still used, which are catalytically active but toxic and problematic for the environment.^[193] Another option is to use catalysts based on other transition metals, such as copper, ruthenium or palladium. The disadvantage of these materials is, however, their price and the possibility of deactivation.^[192] Metal-organic frameworks are nowadays thoroughly studied materials regarding liquid phase oxidation reactions due to their porosity and, thus, the accessibility of active sites.^[194,195] Among these oxidation reactions are for example epoxidations, oxidations of hydrocarbons or oxidations of alcohols to aldehydes, ketones or acids.^[196–198]

A copper-containing MOF material that has frequently been used in catalysis is Cu-BTC, which consists of benzene-1,3,5-tricarboxylate (BTC) linkers and dimeric copper units.^[83] Also mixed-linker materials with 10, 20, 30, 40, 50 mol% of pyridine-3,5-dicarboxylate (PyDC) have been prepared based on Cu-BTC. The resulting catalysts were used in the direct hydroxylation of toluene in the presence of hydrogen peroxide in acetonitrile (**Scheme 1**). It was found out that the Cu-BTC catalyst was highly selective toward *ortho*- and *para*-cresol. However, for all mixed-linker Cu-BTC-PyDC materials, an increase in the methylbenzoquinone selectivity was observed, while the yield of the two cresols decreased. Thus, under the chosen conditions, further oxidation of the aromatic ring was favored over its hydroxylation, compared to Cu-BTC. Independent of these trends, benzaldehyde was the main product for all presented catalysts.^[83]



Scheme 1. Reaction scheme for the oxidation of toluene in the presence of Cu-BTC-based catalysts.

Cobalt-containing MOF materials are broadly investigated in catalysis, as cobalt is highly active and, due to the porosity of metal-organic frameworks, it is also easily accessible within these materials. One of the examples of Co-containing MOF catalysts was presented by Beier *et al.*^[199] STA-12(Co) was used in the aerobic epoxidation of styrene and (*E*)- and (*Z*)-stilbene in DMF. The main products of styrene oxidation are generally styrene oxide, benzaldehyde, and benzoic acid. However, in this specific case, roughly twice the amount of *N*-formyl-*N*-methylformamide (FMF) was formed during the reaction with respect to the converted styrene. It was concluded that the selectivity in styrene epoxidation was low due to substrate oligomerization. In contrast, other substrates, like (*E*)- and (*Z*)-stilbene were epoxidized with high selectivities between 80 and 90 %. During leaching tests, it was confirmed that the reaction proceeded mainly heterogeneously and that the catalyst was reusable with only a small loss of activity.^[199]

Primary and secondary alcohols are used for the production of aldehydes and ketones, respectively. Benzyl alcohol is a primary alcohol which can be oxidized in the first step to benzaldehyde and in the second step to benzoic acid. Hosseini *et al.* used TMU-22(Zn) and introduced Co cations *via* post-synthetic metal exchange for the formation of the mixed-metal TMU-22(Zn/Co).^[200] The crystallinity of bimetallic TMU-22 remained unchanged and various characterization techniques confirmed the successful incorporation of Co into the structure. The catalyst was then used in the photocatalytic oxidation of benzyl alcohol. Almost no conversion was obtained for the reactions without catalyst, light or air. Reaction parameters such as the solvent, catalyst amount, light source, and reaction time were examined and the highest yield was obtained for acetonitrile as the solvent and visible light as the light source. Over time, the conversion increased and the oxidation showcased high selectivity. TMU-22(Zn) showed less than 25 % yield after 3 hours. On the other hand, TMU-22(Zn/Co) obtained more than 60 % yield after 3 h. The catalyst was also tested for its reproducibility – the conversion changed only

slightly between the first and the other 5 consecutive runs. Therefore, it was concluded that the catalyst was recyclable. The leaching test confirmed the heterogeneous nature of the catalytic transformation. Moreover, TMU-22(Zn/Co) was used in other aerobic oxidation of alcohols and aerobic benzylic oxidations confirming that the presence of Co can be beneficial for various oxidation reactions.

Secondary alcohols have typically only one product of oxidation – ketone. Among secondary alcohols belong also 1-phenylethanol which oxidizes to acetophenone. Acetophenone is used as a fragrance and flavoring ingredient, as a special solvent for plastics and resins and also in organic syntheses such as the polymerization of olefins.^[201] Ishida *et al.*^[202] presented the direct deposition of gold clusters onto several MOF structures such as MOF-5, MIL-53 or Cu-BTC. The clusters were deposited by solid grinding with an organogold complex without the usage of a solvent. The resulting materials were active in the oxidation of 1-phenylethanol, with the most active Au/MOF-5 reaching 79 % yield.^[202] Later on, Aryanejad *et al.*^[203] synthesized nanoscale Cu-metal-organic framework with Schiff base as ligand and used it in the oxidation reaction of various primary and secondary alcohols, including 1-phenylethanol with TBHP as oxidation agent. The parameter optimization showed that best results were obtained, when no solvent was used. The yield towards acetophenone was 80 % and generally lower conversion was observed for secondary alcohols than for primary alcohols because of steric effects.

Another other interesting substrate for oxidation reactions is cinnamyl alcohol, which is a primary alcohol possessing an -OH group and a C=C double bond. Therefore, the product of the reaction cannot only be cinnamaldehyde, but also 3-phenylglycidol, the product of epoxidation. Cinnamaldehyde is an important chemical in food and perfume industries. The oxidation of cinnamyl alcohol was already investigated in our group in the year 2019.^[204] In the respective work, palladium nanoparticles were incorporated into defect-engineered bimetallic HKUST-1(Cu,Pd). The results showed that the presence of Pd nanoparticles enhanced the catalytic activity and the fully conversion was obtained after 20 hours. The parent HKUST-1 material was also slightly catalytically active but the synergistic effect of Pd nanoparticles and Pd in the metal-organic framework nodes was profound. The selectivity to cinnamaldehyde was more than 93%, showing that the catalysts can be used for the selective oxidation of cinnamyl alcohol.^[204]

2 Motivation

In the last four decades, the interest in metal-organic frameworks has been steadily increasing. The main reason is their toolbox-like design, in which organic linker molecules and metal centers can be combined to create an almost infinite number of highly crystalline and porous materials. Moreover, in the last years the demand for a rational design of MOFs specific to their usage become more and more significant. Metal-organic frameworks are perfect materials as the choice of linker molecule and metal center can have a direct impact on the performance in the respective application. The complexity of the materials even increases in the cases of mixed-linker or mixed-metal frameworks. MOFs also ally with some principles of green chemistry – they are highly active catalysts, which can contain non-noble metals. Unfortunately, not all materials are possible to synthesize directly during a one-step synthesis and therefore, post-synthetic modification reactions seem to be the answer for more sterically demanding structures. The aim of this work was to synthesize, characterize and test novel mixed-metal materials based on the metal-organic frameworks CPO-27 and DUT-5 and to investigate the differences between their various spatial distributions.

In the first part of this work, bimetallic CPO-27(Co,Fe) catalysts with 1:3, 1:1 and 3:1 Co/Fe ratio should be synthesized, in which a part of the cobalt is substituted by iron. The metals should be incorporated in two different spatial distributions (statistically distributed and core-shell) on equivalent frameworks positions. All catalyst should be first thoroughly characterized using powder X-ray diffraction (PXRD), N₂ physisorption, thermogravimetric analysis (TGA), scanning electron microscope (SEM), X-ray absorption spectroscopy (XAS) and elemental analysis (ICP-OES). Later on, monometallic CPO-27(Co) should be used as a reference material for the parameter optimization in the oxidation of 1-phenylethanol and benzyl alcohol. After the optimization, the bimetallic materials should be tested in both reactions to investigate the influence of the ratios and spatial distribution of the two metals on the catalytic activity.

In the next part, the previously synthesized CPO-27(Co,Fe) materials should be thermally decomposed in inert atmosphere to synthesize materials with unique properties that would not be possible to obtain by any other synthesis way. The catalysts should be characterized by previously mentioned techniques and tested in the oxidation reaction of benzyl alcohol. The aim is to obtain a material where both metals are present within a porous carbonaceous matrix, which should enhance the stability of the catalysts and may have an influence on the catalytic

performance. At the end, the original CPO-27(Co,Fe) MOF materials and the thermally decomposed Co,Fe/C should be compared to investigate the differences in catalytic activity.

In the last part of this thesis, novel DUT-5-based materials should be synthesized using the mixed-metal/mixed-linker concept. Three different linkers should be used, namely 4,4' biphenyldicarboxylate (BPDC), 2,2'-bipyridine-5,5'-dicarboxylate (BPyDC) and 2-amino-4,4'-biphenyldicarboxylate (ABPDC). Also in this part, both statistically distributed and core-shell-structured materials should be synthesized. The statistically distributed material should contain a major amount of unfunctionalized BPDC linker and minor amounts of BPyDC and ABPDC linker, which should be later post-synthetically modified. BPyDC linker should be used for the direct immobilization of cobalt and ABPDC should be modified with a chelating group at which iron can be bound in the next step. The core-shell-structured material should have layers containing the different linkers and the metals would be, thus, spatially separated. The core should consist of BPyDC, the first shell of unfunctionalized BPDC linker and the outer shell of ABPDC linkers. Afterwards, a series of post-synthetic reactions should be performed. In the first PSM reaction, Co should be immobilized at the BPyDC linkers in the core. Next a chelating group should be incorporated at the ABPDC linkers and in the last step, Fe should be immobilized at these chelating groups. In both spatial distributions, Co and Fe are on non-equivalent positions and the different orientation should have an impact on catalytic activity. The materials have to be characterized thoroughly using powder X-ray diffraction, N₂ physisorption, infrared spectroscopy, thermogravimetric analysis, scanning electron microscope, X-ray absorption spectroscopy and elemental analysis (ICP-OES) to reveal the difference in metal orientation. At the end, the catalysts with different spatial distribution should be tested in the oxidation reaction of cinnamyl alcohol.

In summary, this thesis focuses on studies on the influence of iron on the catalytic activity of cobalt-containing MOF materials and the possibility to partially substitute cobalt without decreasing the overall catalytic activity. Moreover, the influence of different metal spatial distributions in MOFs on their catalytic properties will be studied in this thesis.

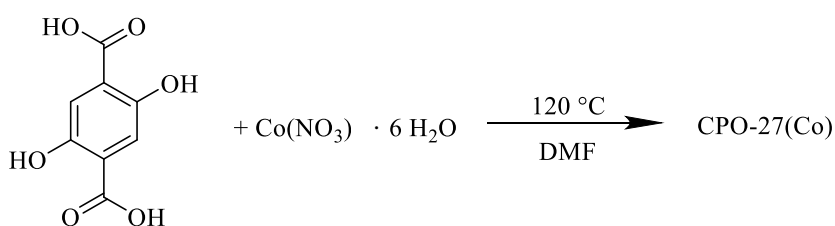
3 Results and discussion

3.1 Synthesis, characterization and catalytic performance of CPO-27 materials

In the following chapters dealing with monometallic MOF materials (**Chapter 3.1.1**) as well as bimetallic MOF materials with statistical distribution (**Chapter 3.1.2**) and their decomposition in inert atmosphere (**Chapter 3.2.2**), some experiments and measurements are included, which have been performed by Benjamin Heider, who was working under the author's supervision on his master thesis in the year 2021. CPO-27(Co)@CPO-27(Fe) materials and their decomposed analogue (**Chapter 3.1.3** and **Chapter 3.2.3**) were synthesized and characterized by Julia Leandro during her bachelor thesis in 2022. Some of the catalytic reactions (**Chapter 3.1.4** and **3.1.4.2**) were performed with the help of Lynn Kirchgatter and Sandra Poplawska during their Forschungspraktika.

3.1.1 Synthesis and characterization of monometallic CPO-27 materials

Monometallic CPO-27(Co) was produced by adjusting the synthesis procedures that were reported in the literature.^[171,205] The specific synthesis is described in **Chapter 5.2.1** and the schematic representation of the reaction can be seen in **Scheme 2**.



Scheme 2. Reaction scheme of the CPO-27(Co) synthesis.

The resulting powder X-ray diffraction pattern of the brown-orange powder confirmed the successful synthesis of a crystalline material and showed a good agreement with the simulated pattern of CPO-27(Co) (see **Figure 17**). Moreover, it did not show any additional reflections and, therefore, the material did not obtain any undesired crystalline phases such as metal oxides or other compounds. The reflection at 20.3° (grey area in **Figure 17**) that was present in the simulated diffraction pattern seemed to be missing in the measured diffractogram. However, the intensity of this reflection is rather low and, therefore, it could be very close to signal to the noise ratio in the measured diffractogram.

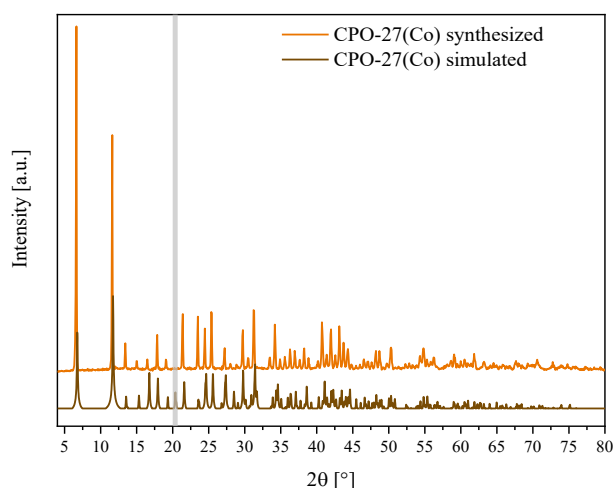
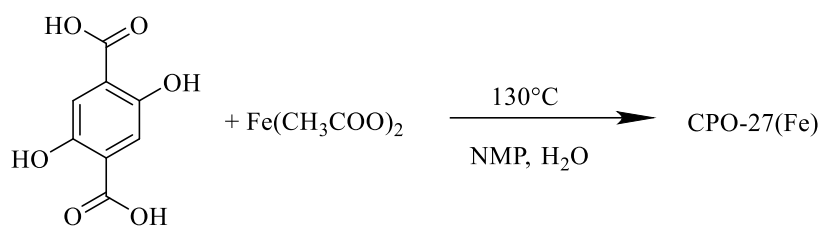


Figure 17. Powder X-ray diffraction patterns of synthesized and simulated CPO-27(Co).^[206]

The synthesis of monometallic CPO-27(Fe) was more challenging. There were several synthesis routes mentioned in the literature^[163,167,171] but none of them was reproducible in our laboratory without modification of the procedures. Therefore, an adjusted synthesis route under reflux in inert atmosphere was developed using 2,5-dihydroxyterephthalic acid and anhydrous iron(II) acetate (see **Scheme 3** and **Chapter 5.2.1** for more details).



Scheme 3. Reaction scheme of the CPO-27(Fe) synthesis.

As can be seen in the powder X-ray diffraction pattern in **Figure 18**, the structure of the resulting black powder was in a good agreement with the simulated pattern. The reflections at 28° and 33° (orange marked area in **Figure 18**) were also listed for the simulated pattern but their intensity was too low to be seen in the respective diffraction pattern of the synthesized material. On the other hand, the reflections at 19° and 28.5° (grey marked area in **Figure 18**) were at the first glance missing in the pattern of the synthesized sample but it was believed that their intensity was only slightly above the background noise. Overall, it could be concluded that the respective structure has successfully been synthesized in a phase-pure form. According to the literature^[163] the resulting material should be stored under inert atmosphere. However, even after several months of storage in air the material did not show any observable changes in the

PXRD pattern. The crystallinity was retained and the diffractogram did not indicate the development of new crystalline phases.

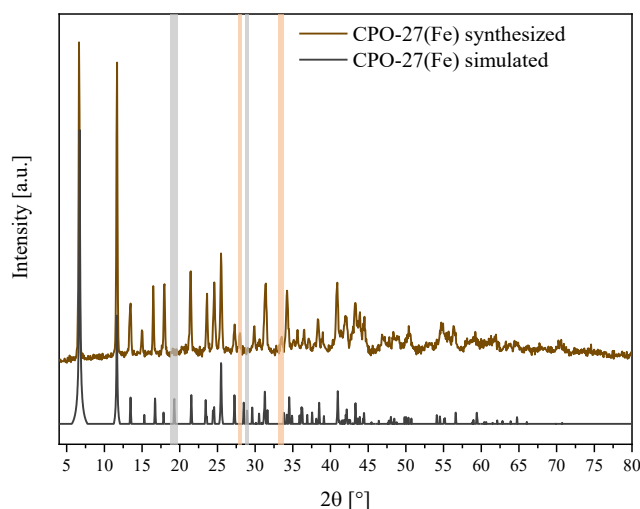


Figure 18. Powder X-ray diffraction patterns of synthesized and simulated CPO-27(Fe).^[163] The major differences in both patterns are marked by grey and orange areas.

Thermogravimetric analysis of the two materials (**Figure 19a**) showed that CPO-27(Fe) was thermally more stable than CPO-27(Co). However, both materials exhibited a significant mass loss already at very low temperatures. Even though, the thermogravimetric analysis was not coupled with a mass spectrometer, the first mass loss with mass loss rate maxima at around 120 °C corresponded probably to the loss of solvent molecules from the pores followed directly by the degradation of the MOF structure. To verify this assumption, CPO-27(Co) was dried in nitrogen atmosphere at 120 °C for 20 hours and a new TG measurement was performed (**Figure 19b**). The resulting graph showed a clear difference between the two measurements, particularly at the beginning. Thus, it could be concluded that the first mass loss corresponded to the evaporation of the solvent from the pores and that the decomposition of the structure began at around 200°C. The DTG curve of CPO-27(Co) showed two other minima which corresponded to the structural decomposition. However, up to now, no TGA-MS measurements were presented in the literature and, thus, the understanding of the step-wise structure decomposition of CPO-27(Co) is very limited. The structure of CPO-27(Fe) decomposed in more steps than CPO-27(Co), which could later help to distinguish bimetallic materials with different Co and Fe ratios.

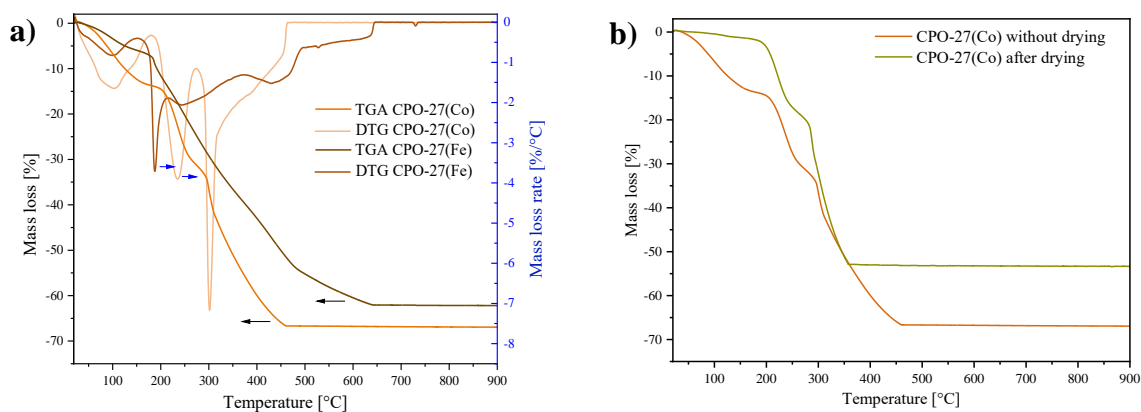


Figure 19. Thermogravimetric analysis (TGA) and their first (DTG) derivatives of **a)** monometallic CPO-27 materials recorded in synthetic air without any pretreatment of the sample, **b)** comparison of CPO-27(Co) recorded in synthetic air without drying and after drying for 20 hours at 120°C in nitrogen atmosphere. Measurement parameters: 10 K/min, 50 ml/min.

For nitrogen physisorption measurements, the material had to be activated first to remove physisorbed water and/or solvent molecules. Activation of CPO-27(Co) was performed at 110 °C for 20 hours and resulted in a black powder with $S_{\text{BET}} = 60 \text{ m}^2/\text{g}$ meaning that the material was already decomposed after this treatment. If the same material was activated at 110 °C only for 5 hours, it featured a specific surface area of $980 \text{ m}^2/\text{g}$. Unlike in the case of CPO-27(Co), *N*-methyl-2-pyrrolidone (NMP) was used for washing of CPO-27(Fe) after the synthesis. The activation was then performed also at 110 °C for 5 hours and the specific surface area was $S_{\text{BET}} = 13 \text{ m}^2/\text{g}$ assuming that solvent molecules could not be removed. Thus, the choice of solvent used in the synthesis or during the washing process could have a massive impact on the activation. NMP has a high boiling point of 203 °C and, therefore, it was believed that the activation temperature was not high enough to remove the solvent molecules from the structure. Because of that, a solvent exchange during the aftertreatment could enable easier activation. Märcz *et al.* reported washing of the compound three times with methanol under argon flushing.^[163] Also Botas^[169] and Calleya^[207] exchanged the solvents by methanol after the synthesis. Therefore, an adjusted aftertreatment procedure using soxhlet extractor was performed, where the powder was treated for 24 hours in pure methanol to replace the solvent molecules in the pores. CPO-27(Fe) did not change its color during the methanol aftertreatment and the PXRD pattern remained the same. After the activation at 110 °C for 5 hours the specific surface area was $340 \text{ m}^2/\text{g}$. Activation for 20 hours at 80 °C resulted in $S_{\text{BET}} = 490 \text{ m}^2/\text{g}$. Higher temperatures or longer time of activation led to specific surface areas lower than $50 \text{ m}^2/\text{g}$, which indicated a structural decomposition of the material. The samples were also activated under nitrogen atmosphere at 90 °C and 110 °C for different times but this led again to non-porous

materials. Therefore, it was not possible to perform the same type of activation for both monometallic materials.

The theoretical amount of the respective metals in the materials should have been 37 wt%. According to the ICP-OES analysis CPO-27(Co) and CPO-27(Fe) contained around 30 wt% in both cases. The theoretical amount of metal was slightly higher because it did not take in consideration the presence of the solvent molecules in the pores. On the other hand, ICP-OES measurements were conducted with the undried samples where the solvent was adsorbed in the structure. In this case, the mass loss assigned to solvent molecules (DMF and NMP) was calculated using the TGA results and the difference between the theoretical and the real amount of the respective metal corresponded to the amount of solvent molecules in the pores.

3.1.2 Synthesis and characterization of bimetallic CPO-27(Co,Fe) materials with statistical distribution

Direct synthesis and post-synthetic metal exchange (PSME) are two well-known principles to synthesize bimetallic MOF materials. Post-synthetic metal exchange is typically used if the direct synthesis of a bimetallic material would be very demanding. Therefore, this approach seemed to be more suitable for CPO-27(Co,Fe). CPO-27(Co) was used as the starting material for PSME in combination with iron(II) chloride. The specific synthesis description can be found in section 5.2.2. After the synthesis, the ICP-OES analysis revealed that, in particular for the samples which aimed at high Fe fractions, only a very low amount of Fe was actually incorporated into the structure (**Table 1**).

Table 1. Desired and measured (ICP-OES) Co:Fe ratio.

Desired ratio (Co:Fe)	Measured ratio
25:75	62:38
50:50	66:33
75:25	80:20

More to that, in **Figure 20a**) an additional reflection was observable when the Fe content or the reaction time were increasing, which corresponded to the most intensive reflection of Fe₂O₃. Therefore, iron was probably partially or fully present in the form of iron oxide and not incorporated directly into the MOF structure as desired. This observation could later be verified during XAS measurements (**Figure 20b**). Only the material with the lowest iron content led to

a slightly shifted radial distance, assuming that CPO-27($\text{Co}_{0.80}\text{Fe}_{0.20}$) - **Figure 20b**) green curve, could have iron incorporated at the desired positions in the crystalline MOF lattice. The low amount of incorporated iron and also the presence of iron in the form of oxides led to an effort to synthesize the bimetallic materials directly.

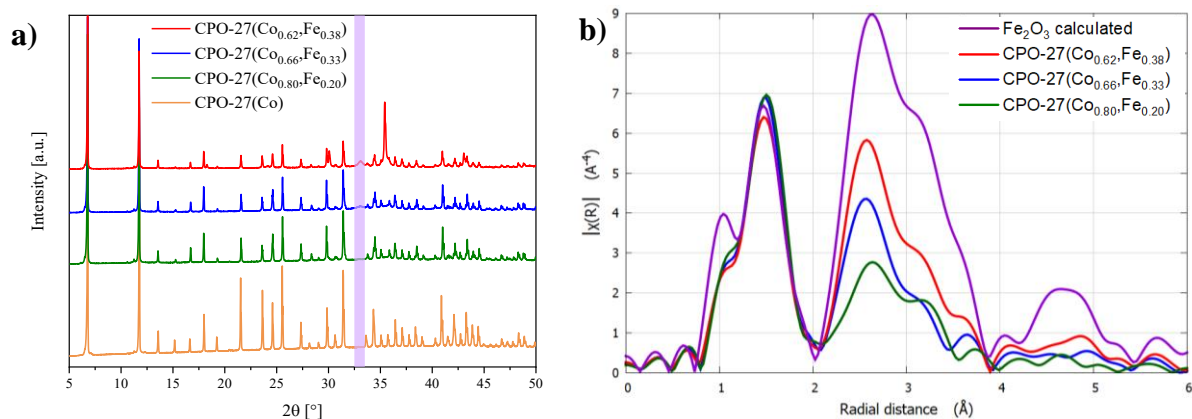


Figure 20. a) PXRD patterns of bimetallic CPO-27(Co,Fe) compared to a CPO-27(Co) reference. Violet area indicates the most intensive reflections of Fe_2O_3 . b) XAS measurements of bimetallic materials and calculated Fe_2O_3 reference.

For the direct synthesis of the bimetallic materials, an adjusted synthesis procedure of monometallic CPO-27 was applied (see **Chapter 5.2.2**). The resulting black-green powders were crystalline and their powder X-ray diffractograms (**Figure 21**) were in good agreement with the CPO-27 structure. No additional crystalline phases were observable.

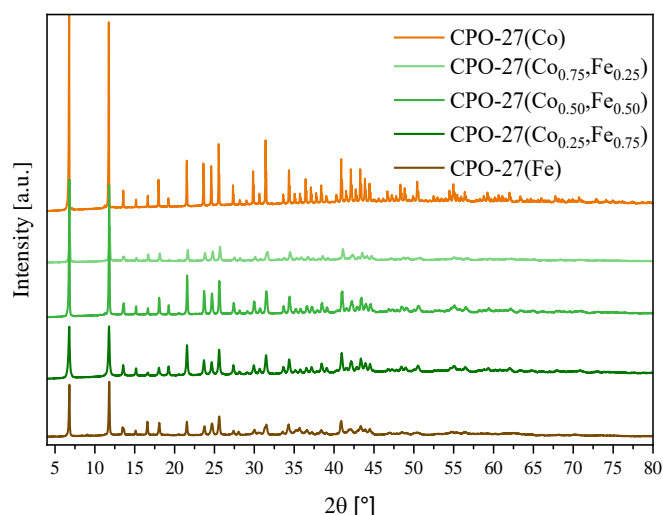


Figure 21. Powder X-ray diffraction patterns of bimetallic materials with CPO-27 structure in comparison to monometallic CPO-27(Co) and CPO-27(Fe).

Thermogravimetric analysis showed that the thermal stability of the bimetallic materials was between monometallic CPO-27 (Co) and CPO-27 (Fe). The first mass loss began already at room temperature, which corresponded to the evaporation of the solvent (**Figure 22**). The structure decomposition started directly afterwards at around 170 °C and featured mostly two steps. (**Figure 22b**). The first minimum of the DTG curve (red area in **Figure 22b**) shifted to higher temperatures with increasing cobalt amount – from 183 °C for CPO-27(Fe), through 187 °C, 208 °C, 221 °C for bimetallic materials, towards 235 °C for CPO-27(Co). The second minimum (blue area in **Figure 22b**) was intensive and easy to distinguish only for materials containing higher amount of cobalt. No trend in the maximal mass loss rate temperature could be observable (302 °C for monometallic CPO-27(Co), 300 °C for CPO-27(Co_{0.75}Fe_{0.25}) and 318 °C for CPO-27(Co_{0.50}Fe_{0.50})). However, the DTG curve was very similar to the DTG curve of monometallic CPO-27(Co). The shape of the DTG curve for CPO-27(Co_{0.25}Fe_{0.75}) was similar to pure CPO-27(Fe) which was in agreement with the higher amount of iron in the sample.

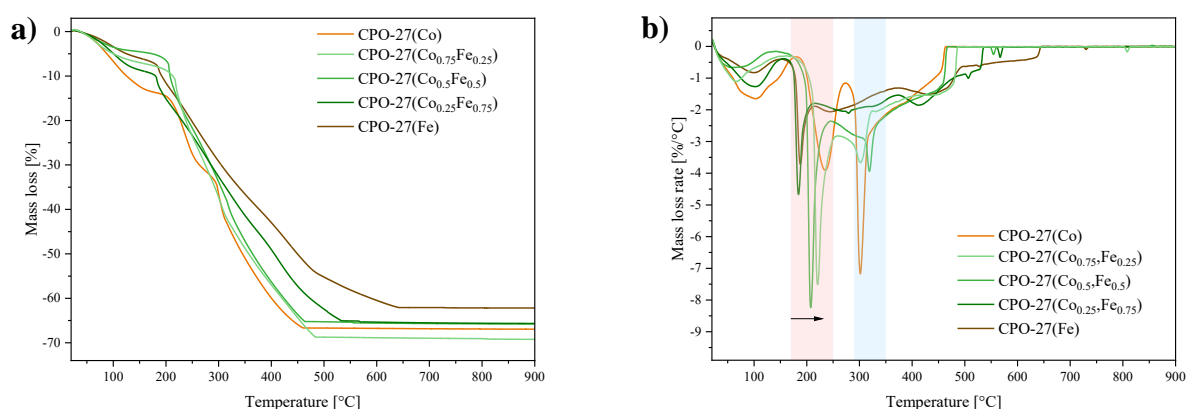


Figure 22. a) Thermogravimetric analysis of monometallic and bimetallic materials recorded in synthetic air. b) First derivative of the TG curves of the respective samples. Measurement parameters: 10 K/min, 50 ml/min.

It was not possible to fully activate the samples for nitrogen physisorption measurements as the activation procedure was either too harsh causing the decomposition of the materials or too mild preventing an effective removal of physisorbed solvent species. Elemental analysis (ICP-OES) confirmed that the Co/Fe ratio was in a good agreement with the desired values even though the cobalt amount was in all materials slightly higher (**Table 2**). This minor difference could be explained as the metals were used in excess compared to the linker (2:1) and the synthesis of the Co variant of CPO-27 was slightly preferred over CPO-27(Fe).

Table 2. Relative Co and Fe contents of statistically distributed CPO-27(Co,Fe) materials determined by ICP-OES.

Material	Co/Fe ratio
CPO-27(Co _{0.25} Fe _{0.75})	29:71
CPO-27(Co _{0.50} Fe _{0.50})	55:45
CPO-27(Co _{0.75} Fe _{0.25})	77:23

3.1.3 Bimetallic CPO-27(Co,Fe) materials with core-shell structure

Bimetallic CPO-27(Co,Fe) can be synthesized not only with statistical distribution but also in a core-shell manner. In this case, either metal can be present in the core or in the shell, respectively. The nomenclature used for core-shell materials is usually “shell@core” in this work. CPO-27(Co)@CPO-27(Fe) had accordingly iron in the core and cobalt in the shell and CPO-27(Fe)@CPO-27(Co) had cobalt in the core and iron in the shell. The synthesis of core-shell materials requires usually two steps: in the first one, the core is synthesized and after washing, drying and characterization it is used for a second step of the synthesis (see **Chapter 5.2.3** for details). Both possible core-shell orientations were synthesized with three different metal ratios (3:1, 1:1 and 1:3) to investigate the differences between these samples and the materials with a statistical distribution of the two metals. All core-shell CPO-27 materials had a PXRD pattern corresponding to the CPO-27 reference (**Figure 23**). As in the case of the statistically distributed materials, no additional crystalline phases were present. Therefore, it seemed that in both types of materials both metals were successfully incorporated into the structure.

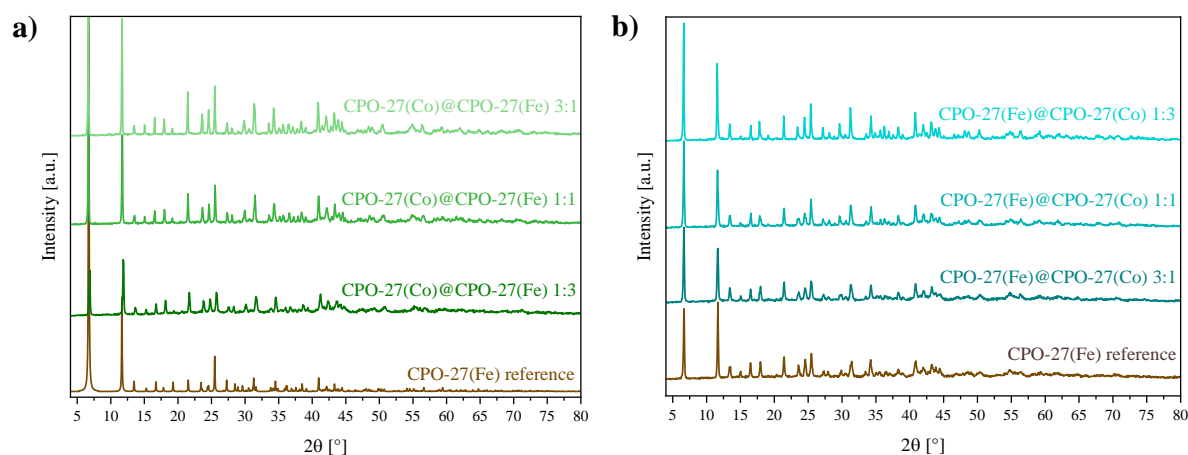


Figure 23. Powder X-ray diffraction patterns of **a)** core-shell-structured CPO-27(Co)@CPO-27(Fe) and **b)** CPO-27(Fe)@CPO-27(Co) and a CPO-27(Fe) reference.

Thermogravimetric measurements were performed for all three metal ratios of CPO-27(Co)@CPO-27(Fe) and two metal ratios (1:1 and 3:1) of CPO-27(Fe)@CPO-27(Co) and the results are presented in **Figure 24a-d)**. The shapes of the TG curves for CPO-27(Co)@CPO-27(Fe) were very similar to the monometallic reference materials and to the statistically distributed bimetallic materials (**Figure 24a)**). The first minima in the DTG curves corresponded to the evaporation of the solvent, which was again almost directly followed by the structure decomposition (**Figure 24b)**). The evaporation temperature of the solvent seemed not to be related to the metal ratio or to the metal distribution. For all three CPO-27(Co)@CPO-27(Fe) materials the structure decomposition after the solvent evaporation had two main minima as for CPO-27(Co) discussed previously.

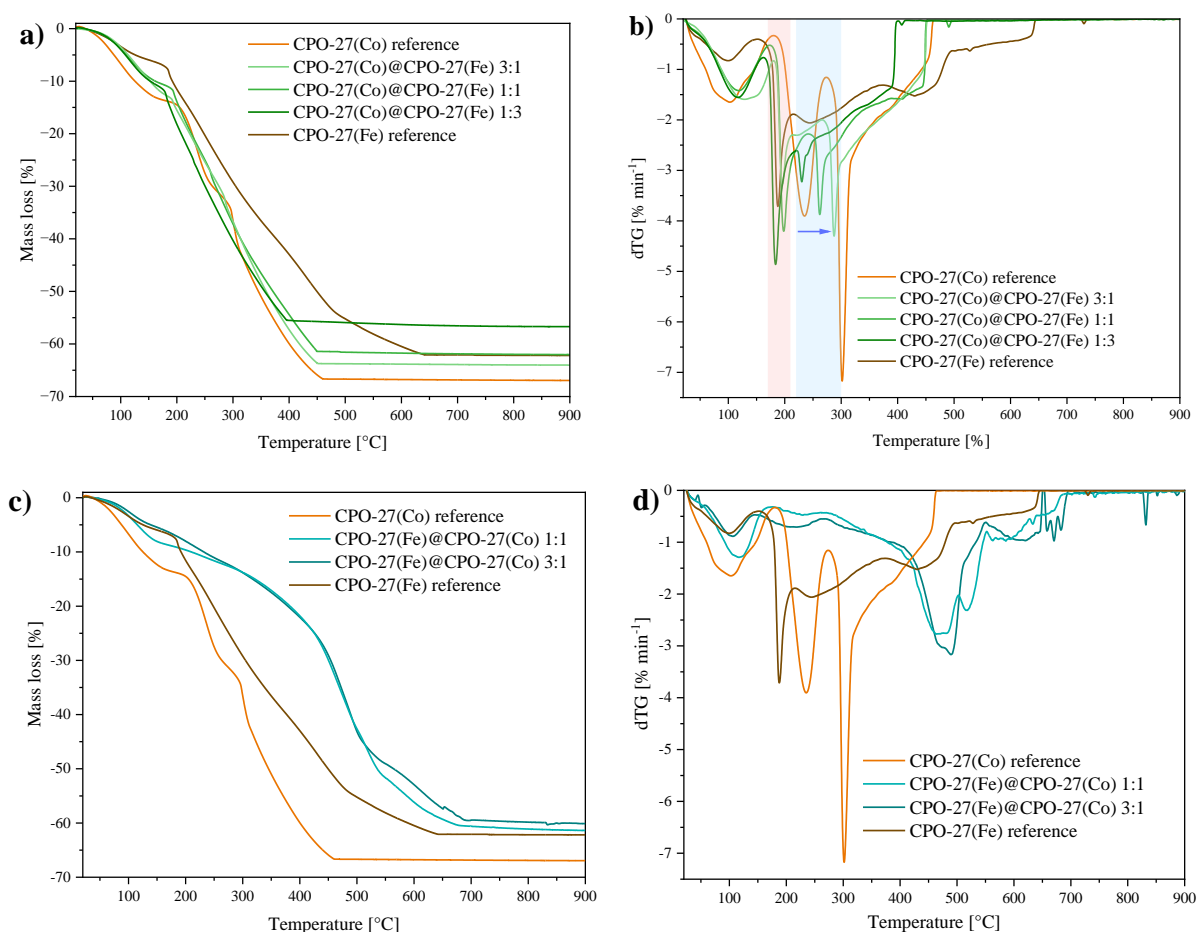


Figure 24. **a)** TG measurements of core-shell-structured CPO-27(Co)@CPO-27(Fe) and a monometallic CPO-27(Fe) reference and **b)** first derivative of TG curves. **c)** TG measurements of core-shell-structured CPO-27(Fe)@CPO-27(Co) and **d)** corresponding DTG. Measurement parameters: 10 K/min, 50 ml/min.

The position of the next observable mass loss (red area in **Figure 24b**) was very similar to CPO-27(Fe) for all materials, including monometallic CPO-27(Fe) and it was observed between 180 °C and 200 °C. The last pronounced mass loss (blue area in **Figure 24b**) shifted towards higher temperatures (see **Table 3**) and became more intense with an increasing cobalt amount. The CPO-27(Co)@CPO-27(Fe) materials decomposed at lower temperature than the monometallic reference materials and also before the bimetallic materials with the statistical distribution. Thus, it could be concluded that the spatial distribution of both sets of samples had to be different.

The results of the thermogravimetric analysis performed with the CPO-27(Fe)@CPO-27(Co) samples are presented in **Figure 24c** and **d**). The solvent removal reached its maximum around 110 °C but afterwards the DTG curves were very different in comparison to the previous materials. The main decomposition of both CPO-27(Fe)@CPO-27(Co) materials started at ca. 400 °C and decomposition was completed at 600 °C. The mass loss rate maxima corresponding

to the structure decomposition were at a significantly higher temperature than for any other CPO-27 material. This phenomenon could not be explained but it made CPO-27(Fe)@CPO-27(Co) very interesting for the usage in catalytic reactions at high temperatures where other CPO-27 materials would not exhibit sufficient thermal stability.

Table 3. Comparison of mass loss rate maxima for monometallic and bimetallic (statistically distributed and core-shell) CPO-27(Co,Fe) materials. N.d. means not determined.

Material	Temperature of maximum mass loss rate [°C]		
	Solvent removal	First maximum of structure decomposition	Second maximum of structure decomposition
CPO-27(Fe)	100	183	-
CPO-27(Co)	102	235	302
CPO-27(Co _{0.25} Fe _{0.75})	101	187	-
CPO-27(Co _{0.50} Fe _{0.50})	66	208	318
CPO-27(Co _{0.75} Fe _{0.25})	66	221	300
CPO-27(Co)@CPO-27(Fe) 1:3	119	183	230
CPO-27(Co)@CPO-27(Fe) 1:1	117	196	264
CPO-27(Co)@CPO-27(Fe) 3:1	128	196	286
CPO-27(Fe)@CPO-27(Co) 3:1	n.d.	n.d.	n.d.
CPO-27(Fe)@CPO-27(Co) 1:1	115	n.d.	n.d.
CPO-27(Fe)@CPO-27(Co) 1:3	106	n.d.	n.d.

All three CPO-27(Co)@CPO-27(Fe) materials had a higher amount of cobalt than desired and all CPO-27(Fe)@CPO-27(Co) showed higher amount of iron than desired (**Table 4**). That means that the core was always slightly smaller than aimed, probably due to the relatively harsh conditions during the synthesis of the shell. As the differences were reproducible, the synthesis could be (if desired) slightly modified to adjust the Co/Fe ratio of the exact values.

Table 4. Co/Fe ratio for core-shell-structured CPO-27(Co,Fe) according to ICP-OES analysis.

Material	Co/Fe ratio determined	Co/Fe ratio targeted
CPO-27(Co)@CPO-27(Fe) 1:3	33:67	25:75
CPO-27(Co)@CPO-27(Fe) 1:1	58:42	50:50
CPO-27(Co)@CPO-27(Fe) 3:1	83:17	75:25
CPO-27(Fe)@CPO-27(Co) 3:1	19:81	25:75
CPO-27(Fe)@CPO-27(Co) 1:1	40:60	50:50
CPO-27(Fe)@CPO-27(Co) 1:3	66:34	75:25

Standard techniques of characterization (mainly TGA) showed differences between statistically distributed and core-shell materials. However, all presented characterization techniques gave only an indirect proof of the spatial distribution of the two metals. To confirm the metal distribution in the samples, TEM/EDX measurements with sufficient resolution would be required, which were not available during this work.

3.1.4 Catalytic applications of CPO-27-based materials

3.1.4.1 Application of statistically distributed CPO-27(Co,Fe) catalysts in the liquid phase oxidation of 1-phenylethanol

For the optimization of the reaction parameters CPO-27(Co) was chosen as a highly active catalyst. As a substrate 1-phenylethanol was used, which is a secondary alcohol and can only be oxidized to acetophenone without the possible formation of an acid as a subsequent product. A parameter optimization was performed using the one-factor method, in which only one parameter was investigated at once with the rest of the parameter fixed. The starting parameters (5 mmol 1-phenylethanol, air flow rate of 200 ml/min, a reaction temperature of 140 °C and 0.010 mmol of Co in 30 ml DMF) were chosen so that CPO-27(Co) was active in catalysis but not reaching full conversion, leaving space for improvements (**Figure 25**). After six hours, the conversion was 71 % and the reaction rate was decreasing after the third hour. That could be explained by substrate limitation. For comparison, a blind reaction with the same parameters

was performed. The conversion without catalyst was significantly lower (only 14 %) and proceeded linear over the whole reaction time.

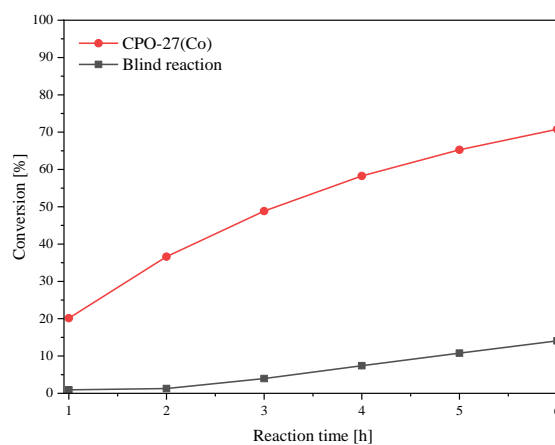


Figure 25. Degree of conversion for reaction with CPO-27(Co) compared to the blind reaction. Reaction parameters: 5 mmol 1-phenylethanol, 140 °C, 0.010 mmol catalyst (0.4 mol% Co with respect to the substrate), 200 ml/min, 30 ml DMF.

The first investigated parameter was the oil bath temperature. For the air flow of 200 ml/min, the oil bath temperature had almost no influence on the degree of conversion (after 6 hours the conversion was between 64 % for 150 °C and 71 % for 140 °C) as can be seen in **Figure 26a**). According to Arrhenius formula, the rate constant should increase exponentially and as this was not the case, some limiting factors had to play a major role. In the next set of experiments, the air flow rate was increased from 200 ml/min to 300 ml/min (**Figure 26b**). In this case, differences in conversion were observable for different temperatures and also the degree of conversion was increasing with the oil bath temperature as expected. Already these experiments suggested that oxygen transport had to play an important role in this reaction.

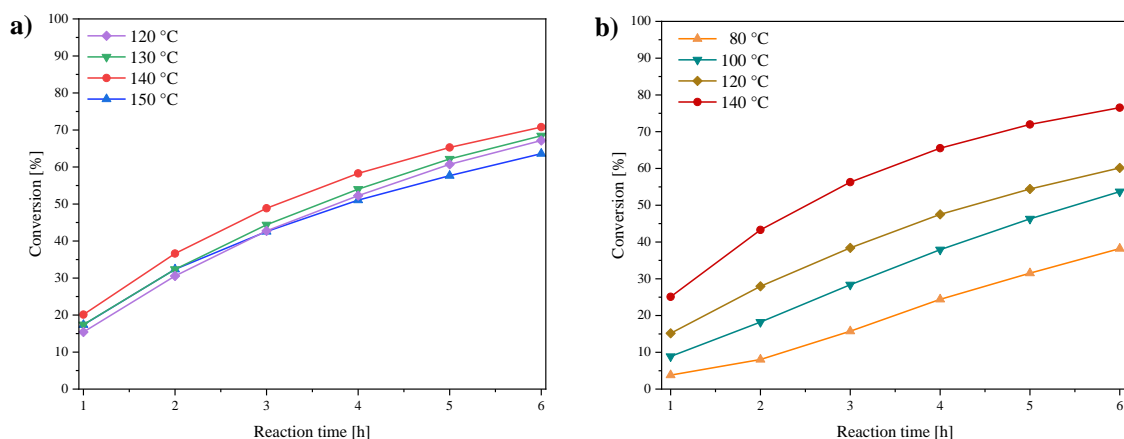


Figure 26. Influence of temperature and air flow rate on degree of conversion for **a)** 200 ml/min and **b)** 300 ml/min. Reaction parameters: 5 mmol 1-phenylethanol, 140 °C, 0.010 mmol catalyst (0.4 mol% Co with respect to the substrate), 30 ml DMF.

Interestingly, for the air flow of 300 ml/min, the degree of conversion was lower than for 200 ml/min at the same temperature (60 % vs 67 % for 120 °C). This could be explained by a drop in temperature as the gas stream through the reaction mixture was not preheated. Thus, a higher air flow rate may have caused a lower temperature inside the reaction flask. The temperatures in the reaction flask were not measured, due to experimental difficulties.

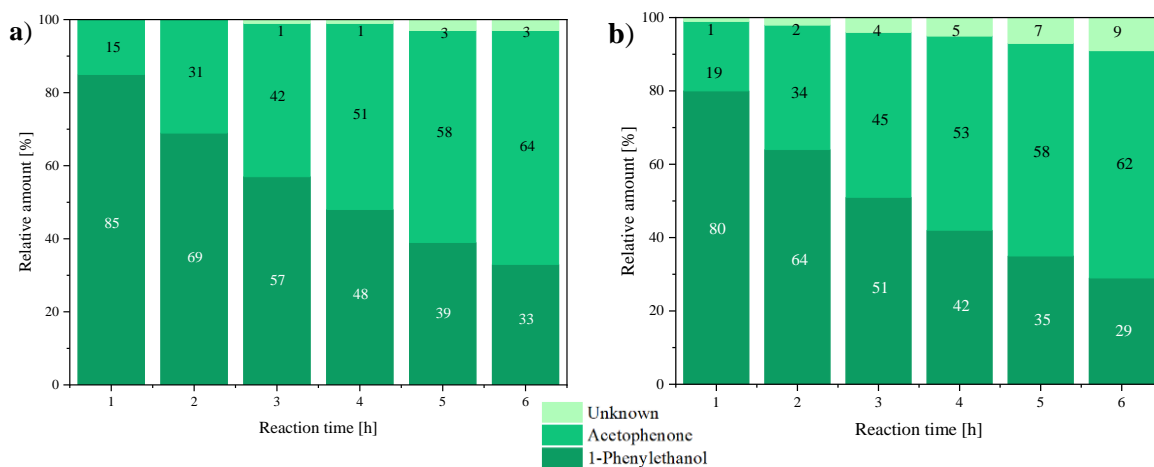


Figure 27. Relative amount of chemicals in the reaction according to GC-MS measurements for **a)** 120 °C and **b)** 140 °C. Reaction parameters: 5 mmol 1-phenylethanol, 200 ml/min, 0.010 mmol catalyst (0.4 mol% Co with respect to the substrate), 30 ml DMF.

The GC-MS analysis of the reaction mixture revealed that the total amount of the product and the reactant did not correspond to 100 % (**Figure 27**). However, no specific side products were observable during the GC-MS analysis itself, which could be explained by the different polarity of the column and the unknown products. It is also possible that volatile species might have been evaporated from the flask during the reaction. Another possibility would be the formation

of high-boiling compounds (e.g. by reaction with the solvent), which could not be vaporized at the inlet of GC. The results showed that the amount of produced acetophenone was almost the same regardless the temperature. With time and temperature, the missing amount was increasing, reaching 9 % after 6 hours at 140 °C.

For the next series of experiments, an oil bath temperature of 140 °C has been chosen and the catalyst amount was varied between 0.008 mmol and 0.015 mmol. The results (**Figure 28**) revealed only very small differences in the product amount, almost in the range of accuracy of the GC analysis (2 %). Theoretically, increasing the catalyst concentration increases the amount of the active sites and therefore, it should lead to significantly higher product yields under otherwise identical conditions.

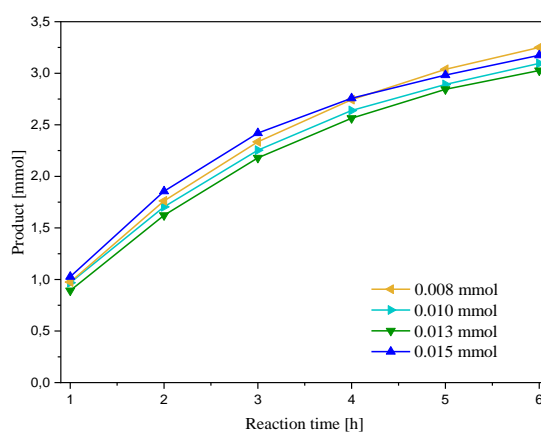


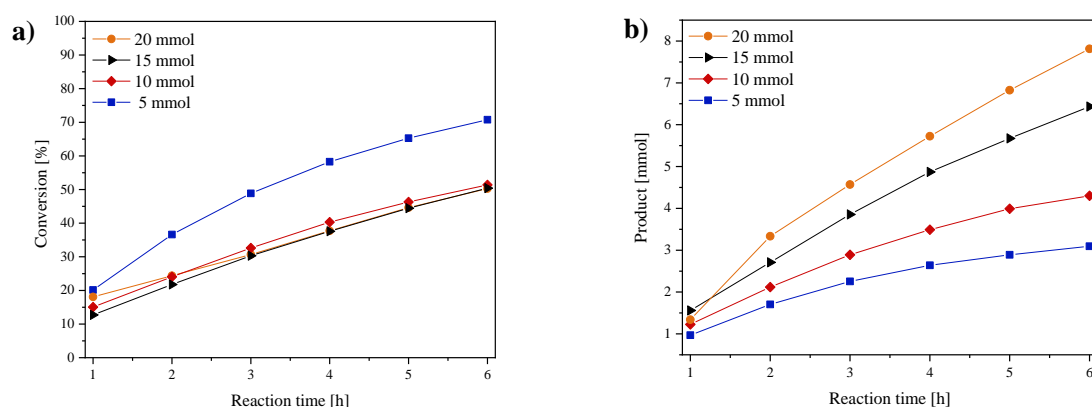
Figure 28. Influence of the catalyst amount on the formation of acetophenone. Reaction parameters: 5 mmol 1-phenylethanol, 140 °C, 200 ml/min, 30 ml DMF.

The turnover numbers (**Table 5**) were decreasing with the increasing catalyst amount. The variation of the catalyst amount led to the conclusion that the limitation was not caused by the concentration of the catalyst in the reaction flask and it had to be caused by other transport limitations. For further investigations, 0.01 mmol catalyst (0.4 mol% Co) was chosen as it was the smallest amount that could be reproducibly weighed into the flask without a significant error.

Table 5. Turnover numbers for each catalyst amount after 6 hours. Reaction parameters: 5 mmol 1-phenylethanol, 140 °C, 200 ml/min, 30 ml DMF.

Catalyst amount [mmol]	Product [mmol]	Turnover number [h ⁻¹]
0.008	3.25	406
0.010	3.10	310
0.013	3.03	233
0.015	3.17	211

The transport limitation could be, therefore, caused by 1-phenylethanol or by oxygen. Firstly, the variation of 1-phenylethanol was investigated. Between 5 and 20 mmol of 1-phenylethanol were used and the results are presented in **Figure 29**. The results were very similar for higher substrate amounts (after six hours the degree of conversion was about 50 %). The highest conversion was obtained for 5 mmol of substrate (71 %). However, it is complicated to compare the degree of conversion because different substrate amounts were used. The absolute amount of product formed (mmol) was the more relevant information. As could be seen in **Figure 29b**), the amount of product was increasing with the substrate amount, as expected. The curve shape indicated that for smaller substrate amount, the gradient was decreasing after longer reaction times and, therefore, the substrate availability was limited. For larger substrate amounts, the curves were almost linear throughout the whole six hours of the reaction and the reaction rate would only decrease after longer reaction times. For the further optimization, 5 mmol of 1-phenylethanol were chosen.

**Figure 29.** Conversion (a) and product formation during the synthesis (b) for different substrate amounts. Reaction parameters: 140 °C, 200 ml/min, 0.010 mmol catalyst (0.4 mol% Co to substrate), 30 ml DMF.

After the temperature, catalyst amount and substrate amount optimization, the influence of the air flow rate was investigated (**Figure 30**). Increasing the flow rate from 100 ml/min to 200 ml/min led to a significant increase in the conversion. However, the difference between 200 ml/min and 300 ml/min was not as significant as expected. This could be caused by an oxygen solubility restriction, i.e. the solubility of oxygen in the solution was limited at 140 °C and the increase of oxygen did not, beyond some point, have any influence.

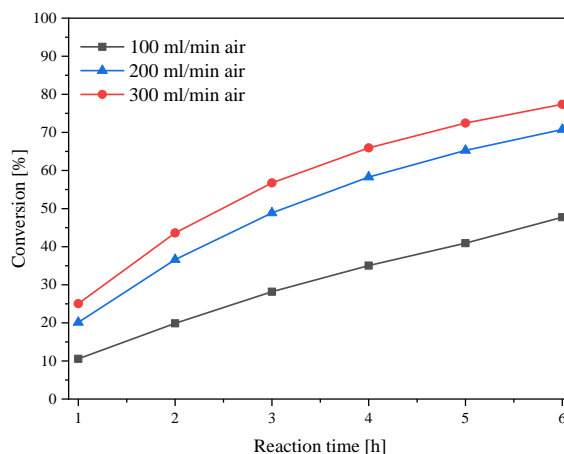


Figure 30. Substrate conversion for different air flow rates. Reaction parameters: 5 mmol 1-phenylethanol, 140 °C, 0.010 mmol catalyst (0.4 mol% Co to substrate), 30 ml DMF.

It seemed that the limitations were caused by the substrate amount and, at higher temperatures, also by the oxygen solubility. To verify this assumption, the temperature experiments were once more repeated with the optimized parameters (5 mmol 1-phenylethanol, 0.010 mmol catalyst, 200 ml/min air flow and 30 ml DMF). **Figure 31** showed that the conversion was increasing up to 130 °C. As these results were significantly different from each other and from the initial experiment presented in **Figure 26a**), it could be concluded that the main limitation throughout this reaction was caused by the substrate transport limitation. Higher oil bath temperatures above 130 °C led again to a lower conversion, which could be explained by the limited solubility of oxygen in a hot solution.

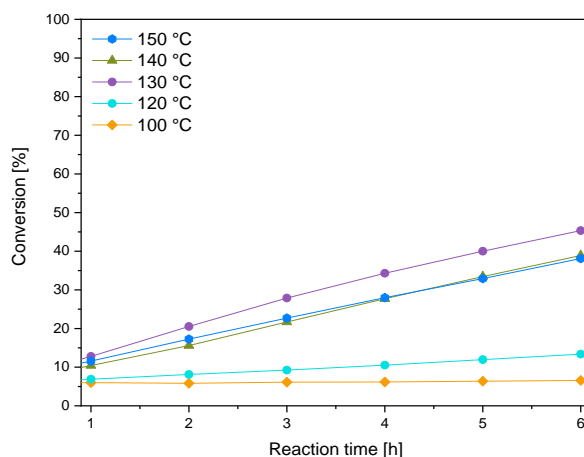


Figure 31. Influence of temperature on oxidation of 1-phenylethanol under optimized conditions. Reaction parameters: 5 mmol substrate, 0.4 mol% Me in catalyst, 200 ml/min air and 30 ml DMF.

To investigate the possibility of the chemicals being carried out of the solution at high gas flow rates (as discussed previously under **Figure 27**), experiments at 120 °C with an air flow of 200 ml/min and 300 ml/min were compared. As presented in **Figure 32**, almost no difference was observable. The accuracy of the GC-MS analysis was 2 % and the difference between 200 ml/min and 300 ml/min was not larger than 3 %. Thus, it seemed unlikely, that a part of the solution would be carried out of the reaction or trapped in the cooler. Probably at least one side product was formed during the reaction (e.g. by reaction with solvent), which was not observable in the gas chromatograph.

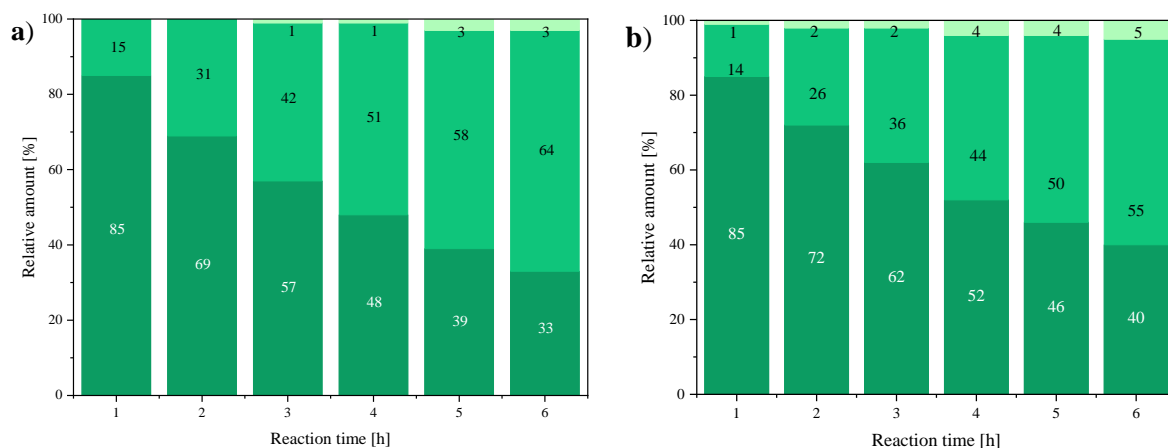


Figure 32. Relative amount of chemicals present in the reaction according GC-MS measurements for **a)** 200 ml/min and **b)** 300ml/min. Reaction parameters: 5 mmol 1-phenylethanol, 120 °C, 0.010 mmol catalyst (0.4 mol% Co to substrate), 30 ml DMF.

To overcome the substrate limitation, 15 mmol of substrate were used in the following experiments with the catalytic testing of the statistically distributed bimetallic catalysts.

Monometallic CPO-27(Co) and CPO-27(Fe) were also tested for comparison. As can be seen in **Figure 33**, CPO-27(Fe) exhibited the lowest degree of conversion (only 4 %). This was even lower than the blind reaction (9 % after six hours) and, thus, CPO-27(Fe) seemed to hinder the reaction. On the other hand, CPO-27(Co) was very active (76 % conversion after six hours). The bimetallic materials featured similar activities as the monometallic CPO-27(Co) reference. Note, however, that CPO-27(Co_{0.75}Fe_{0.25}) exhibited the lowest degree of conversion within these experiments (73 %) even though, it had the highest amount of cobalt of all bimetallic materials. Since total (Co+Fe) metal amount of 0.4 mol% was chosen in all experiments of this series, the absolute amount of cobalt in the reaction was different, according to Co/Fe ratio. Therefore, it would be expected that the bimetallic material with the highest cobalt amount should be also the most active. However, this was not the case.

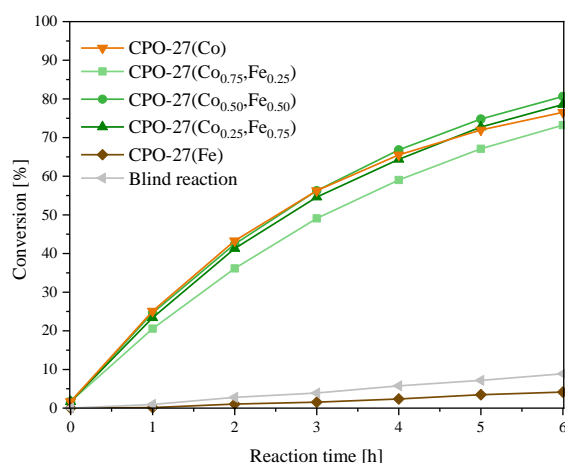


Figure 33. Time-dependent conversion in the oxidation of 1-phenylethanol with CPO-27(Co), CPO-27(Co_{0.75}Fe_{0.25}), CPO-27(Co_{0.50}Fe_{0.50}), CPO-27(Co_{0.25}Fe_{0.75}) and CPO-27(Fe). Reaction parameters: 15 mmol 1-phenylethanol, 140 °C, 30 ml DMF, 0.4 mol% metal in catalyst and air flow of 300 ml/min.

The largest calculated turnover number of 370 was determined for CPO-27(Co_{0.50}Fe_{0.50}). It could be concluded that the presence of iron in the structure was beneficial for the oxidation of 1-phenylethanol and the materials featured a synergistic effect of the two metals.

3.1.4.2 Application of CPO-27-based catalysts in liquid phase oxidation reaction of benzyl alcohol

In the next series of experiments, benzyl alcohol was chosen as a substrate. Benzyl alcohol is a more interesting substrate than 1-phenylethanol, because it is a primary alcohol, for which the formation of benzoic acid is possible *via* an over-oxidation of the aldehyde. Since the metal distribution (statistical *vs.* core-shell) can have an influence on the catalytic activity and selectivity, catalysts with a different spatial distribution of the metals were also investigated in

this study. Also here, CPO-27(Co) was used for a one-factor optimization and first the oil bath temperature was varied from 120 °C to 150 °C. However, to evaluate the kinetics the actual temperature in the reaction mixture (which was between 110 °C to 135 °C) had to be considered (**Figure 34a**). The highest degree of conversion was obtained at 135 °C (89 % after 6 hours). With decreasing temperature, the conversion was also decreasing to 31 % for 110 °C after six hours. The gradient within the conversion curves was usually decreasing with longer reaction times (except for 110 °C) and, thus, only the first two hours were used for the calculation of the initial reaction rate (**Figure 34b**). The initial reaction rate (converted amount of the reactant per hour) showed an increase from 0.3 mmol/h at 110 °C to 1.7 mmol/h at 135 °C. Even though the data were not on a perfect line, a linear fit could be applied, showing that the initial reaction rate increased roughly by 0.055 mmol/h per Kelvin. The over-oxidation to benzoic acid was observable only for higher reaction temperatures (**Figure 34c**) after six hours. For 130 °C and 135 °C, the yield of benzaldehyde was 53 % in both cases but the yield of benzoic acid increased from 5 % to 9 %. For the subsequent parameter optimization, a reaction temperature of 135 °C (150 °C oil bath temperature) has been chosen.

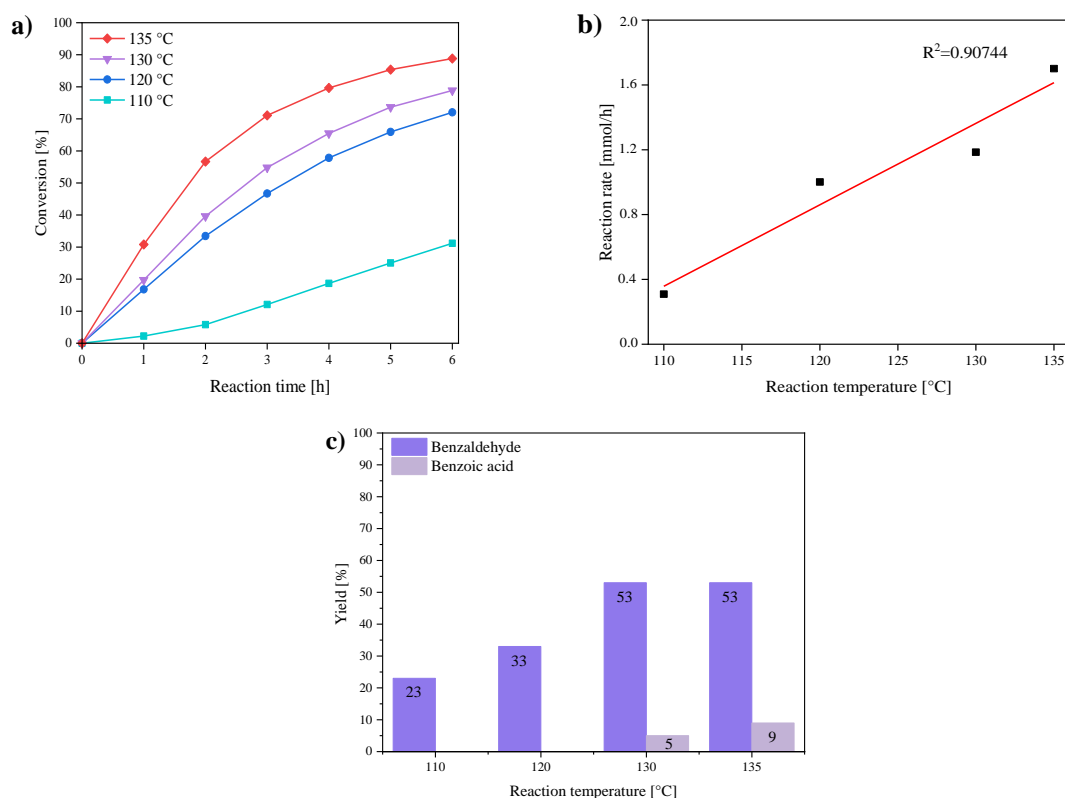


Figure 34. a) Influence of the reaction temperature on conversion, b) linear fit of the initial reaction rate as a function of the reaction temperature and c) influence of reaction temperature on the yield after six hours. Reaction parameters: 6 mmol benzyl alcohol, 0.012 mmol catalyst (0.4 mol% Co to substrate), 200 ml/min air flow, 60 ml DMF.

The variation of the catalyst concentration (**Figure 35a**) revealed a similar trend for the oxidation of benzyl alcohol as previously for 1-phenylethanol. 0.4 mol% of metal in the catalyst, with respect to the substrate amount, showed the highest conversion (89 %) after six hours. When the catalyst amount increased above 0.4 mol% of cobalt, the degree of conversion decreased slightly and the differences between 0.6 and 1.0 mol% were minor after six hours (between 83 % and 85 %). Also, at the beginning of the reaction (after one hour) the differences were not significant. Therefore, it could be concluded that also for this substrate, transport limitations were important. A catalyst amount of 0.4 mol% cobalt has been chosen even though the results showed that the over-oxidation to benzoic acid had the highest yield with this amount of catalyst (**Figure 35b**). In the last step, the air flow rate was investigated (**Figure 35c**). 100 ml/min of air led to a conversion of 68 %. The increase to 200 ml/min showed a significantly better conversion (89 %). However, a further increase to 300 ml/min did not show any improvement. In the case of yields (**Figure 35d**), the over-oxidation to benzoic acid was the same for 200 ml/min and 300 ml/min (9 %). This observation could be interpreted in two different ways. Firstly, the gas flow through the reaction was not preheated. Secondly, also the contact time between the substrate and oxygen was shorter. The latter problem could be solved by introduction of smaller air bubbles to the reaction. Still, the limited solubility of oxygen in the solvent (as discussed in **Chapter 3.1.4.1**) would remain.

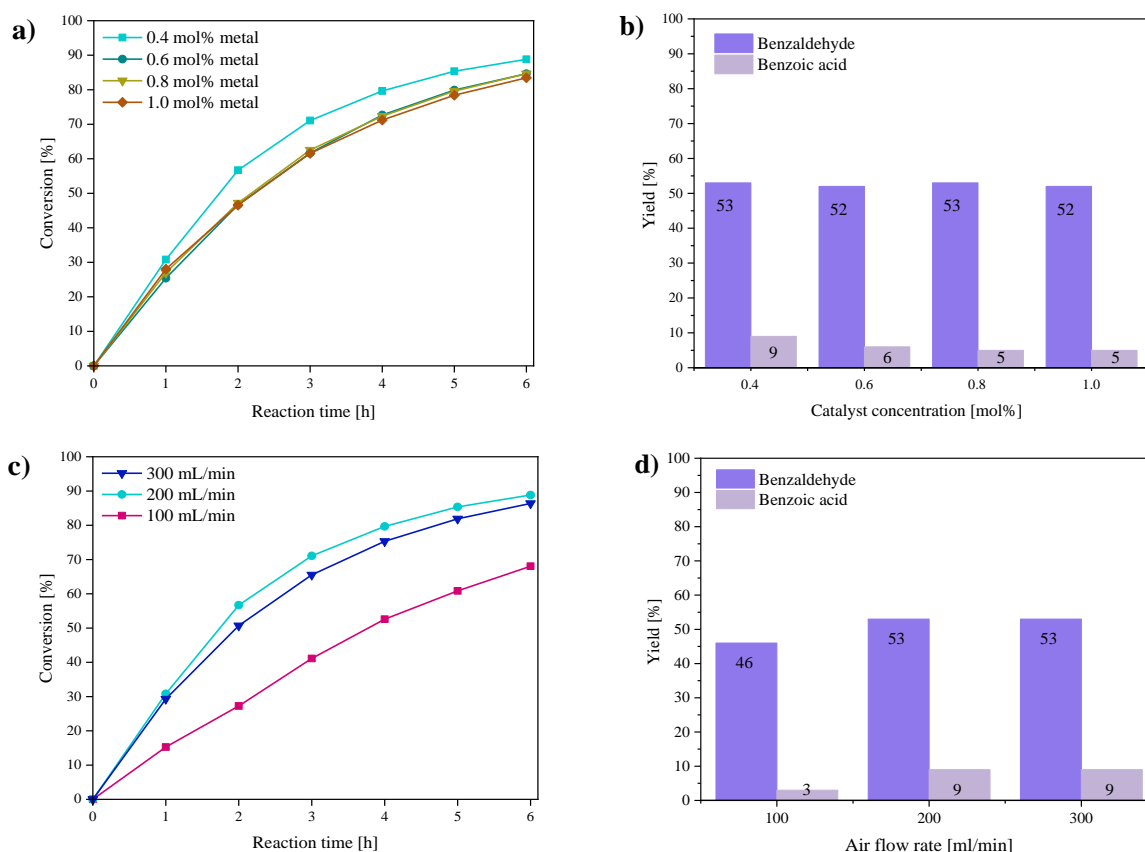


Figure 35. Influence of the catalyst concentration (a) and the air flow rate (b) on the conversion of benzyl alcohol. Reaction parameters: a) 6 mmol benzyl alcohol, 135 °C, 200 ml/min air flow, 60 ml DMF, b) 6 mmol benzyl alcohol, 135 °C, 0.012 mmol catalyst (0.4 mol% Co to substrate), 60 ml DMF.

The best parameters were a reaction temperature of 135 °C (150 °C oil bath temperature), 6 mmol of benzyl alcohol, 0.012 mmol CPO-27(M) catalyst (0.4 mol% of metal to substrate), an air flow rate of 200 ml/min and 60 ml DMF. However, for the catalytic test reactions, a reaction temperature of 120 °C was chosen to monitor the differences between the catalysts.

a) Statistically distributed CPO-27(Co,Fe) catalysts

The blind reaction exhibited a conversion of 34 % after six hours and the monometallic CPO-27(Fe) catalyst yielded only 29 % after six hours. CPO-27(Fe) hindered the reaction, as in the case of 1-phenylethanol. On the other hand, the monometallic cobalt material was highly active featuring a conversion of 72 % after six hours. All bimetallic CPO-27(Co,Fe) catalysts performed very similar. The conversion after six hours was between 77 and 80 % for all three materials. Comparing the monometallic CPO-27(Co) and all statistically distributed bimetallic materials, it could be clearly seen that the bimetallic materials were the more active catalysts, regardless of the cobalt amount. Also here, the amount of cobalt in CPO-27(Co,Fe) did not have

any significant influence on the catalytic performance and, thus, the amount of cobalt could be significantly lowered by using Fe-rich catalysts.

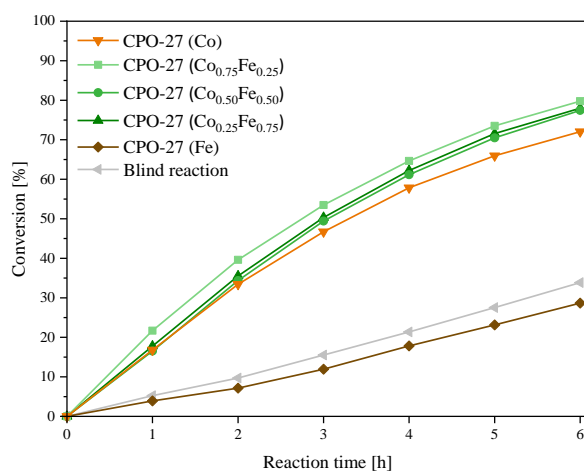


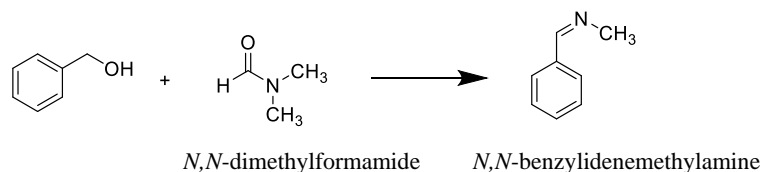
Figure 36. Time-dependent conversion in the benzyl alcohol oxidation with CPO-27(Co), CPO-27(Co_{0.75}Fe_{0.25}), CPO-27(Co_{0.50}Fe_{0.50}), CPO-27(Co_{0.25}Fe_{0.75}) and CPO-27(Fe) in comparison to the blind reaction. Reaction parameters: 6 mmol benzyl alcohol, 120 °C, 0.012 mmol catalyst (0.4 mol% Co to substrate), 200 ml/min, 60 ml DMF.

Regarding the kinetics within the first two reaction hours, the initial reaction rates differed only slightly. CPO-27(Co_{0.5}Fe_{0.5}) showed the lowest value with a rate of 1.0 mmol/h, CPO-27(Co_{0.25}Fe_{0.75}) had a reaction rate of 1.1 mmol/h and CPO-27(Co_{0.75}Fe_{0.25}) 1.2 mmol/h. These minor differences were within the range of the experimental errors and, thus, cannot be considered as significant or even relevant. The selectivities (**Table 6**) were compared at conversions around 35 % and the selectivity to benzaldehyde was between 67 and 70 % for all catalysts (even for the virtually inactive CPO-27(Fe)). At this low conversion level, no over-oxidation to benzoic acid was observable. However, the over-oxidation to benzoic acid took place after longer reaction times. For CPO-27(Co) and also for all bimetallic catalysts, the selectivity to benzoic acid was around 15 %. As there are no big differences in the selectivities between CPO-27(Co) and the bimetallic CPO-27(Co,Fe) catalysts, the latter materials had a positive influence on the catalysis, showing slightly better results regarding the conversion than the monometallic CPO-27(Co). Thus, a real synergistic effect of cobalt and iron was confirmed, which allowed to reduce the amount of the active metal (Co) by the partial substitution with an available and cheap metal (Fe), which is virtually inert in the target reaction.

Table 6 Catalytic performance of the CPO-27-catalysts in the oxidation of benzyl alcohol. Comparison of the selectivity with respect to benzaldehyde at a conversion level of approx. 35 %. Turnover frequency was calculated for the first two hours. Reaction parameters: 6 mmol benzyl alcohol, 120 °C, 0.012 mmol catalyst (0.4 mol% Co to substrate), 200 ml/min, 60 ml DMF.

Catalyst	Conversion [%]	Selectivity to benzaldehyde [%]	Turnover frequency [h ⁻¹]
CPO-27(Co)	33	67	250
CPO-27(Co _{0.75} Fe _{0.25})	40	70	295
CPO-27(Co _{0.50} Fe _{0.50})	34	67	258
CPO-27(Co _{0.25} Fe _{0.75})	36	67	267
CPO-27(Fe)	28	68	53

The combined selectivity towards benzaldehyde and benzoic acid was only around 82 % for all statistically distributed catalysts. This suggested that additional products were generated during the reaction. By using GC-MS analysis *N*-benzylidenemethylamine could be determined as an additional product with a selectivity of 15 %.



Scheme 4. Side reaction of benzyl alcohol with DMF (solvent).

This molecule was produced by a reaction of benzaldehyde with the solvent (**Scheme 4**). Given the accuracy of the analytics, no additional product was detected during the reaction.

b) Core-shell-structured CPO-27 catalysts

The catalytic results for the core-shell materials (**Figure 37**) showed that CPO-27(Co)@CPO-27(Fe) had, in general, a higher conversion than CPO-27(Fe)@CPO-27(Co). The lower conversion of CPO-27(Fe)@CPO-27(Co) was probably caused by the more complicated accessibility of the CPO-27(Co) core through inactive CPO-27(Fe) shell. The most active catalysts were CPO-27(Co)@CPO-27(Fe) with a Co/Fe ratio of 3:1 and CPO-27(Co)@CPO-27(Fe) with a Co/Fe ratio of 1:1 (78 % after six hours), which was even more active than the CPO-27(Co) reference. The selectivity towards benzaldehyde was comparable for all reactions after six hours (46 %) and therefore, it is not shown in a separate figure. Interestingly, during these reactions no over-oxidation to benzoic acid was observed.

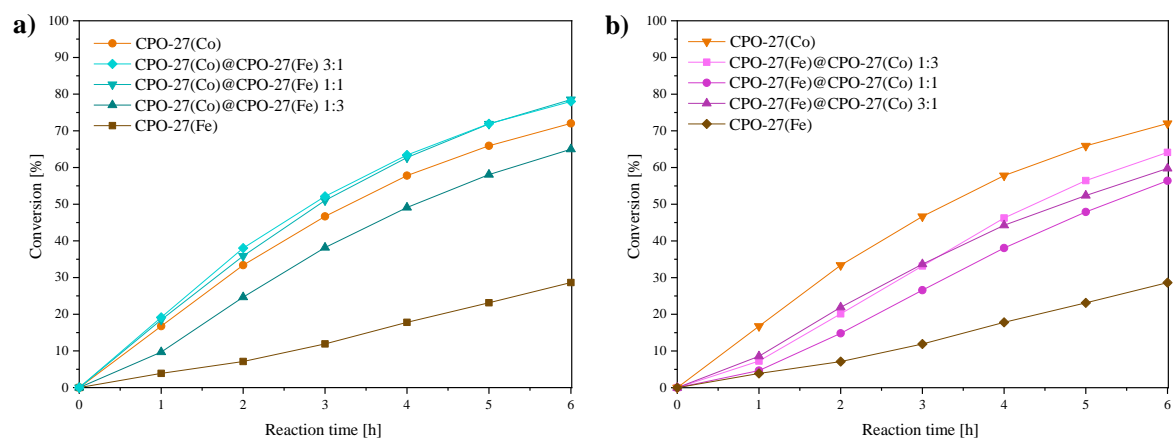


Figure 37. Time-dependent conversion in the benzyl alcohol oxidation with core-shell-structured CPO-27 catalyst compared to a CPO-27(Co) reference material. **a)** CPO-27(Co)@CPO-27(Fe) and **b)** CPO-27(Fe)@CPO-27(Co) Reaction parameters: 6 mmol benzyl alcohol, 120 °C, 0.012 mmol catalyst (0.4 mol% Co to substrate), 200 ml/min, 60 ml DMF

Overall, the most active catalysts in the oxidation of benzyl alcohol were the statistically distributed CPO-27(Co,Fe) with conversions up to 80 % after six hours (green lines in **Figure 38a-c)**). The core-shell-structured materials CPO-27(Co)@CPO-27(Fe) 1:1 and 3:1 reached the same conversion as the statistically distributed materials, but with no over-oxidation. Therefore, it was assumed that the over-oxidation took place only when both metals were in a close vicinity and the usage of core-shell materials with Co in a shell can be beneficial in catalysis to limit the subsequent formation of benzoic acid. On the other hand, CPO-27(Fe)@CPO-27(Co) materials were not as active as the rest of the MOF materials, assuming that the iron shell limited the accessibility of catalytically active core. The materials with a Co/Fe ratio of 1:3 (**Figure 38c)**) reached a high conversion only if the two metals were statistically distributed (78 %). Both core-shell orientations (1:3 Co/Fe ratio) exhibited similar results around 64 % regardless of the metal in core, probably due to their limited cobalt amount.

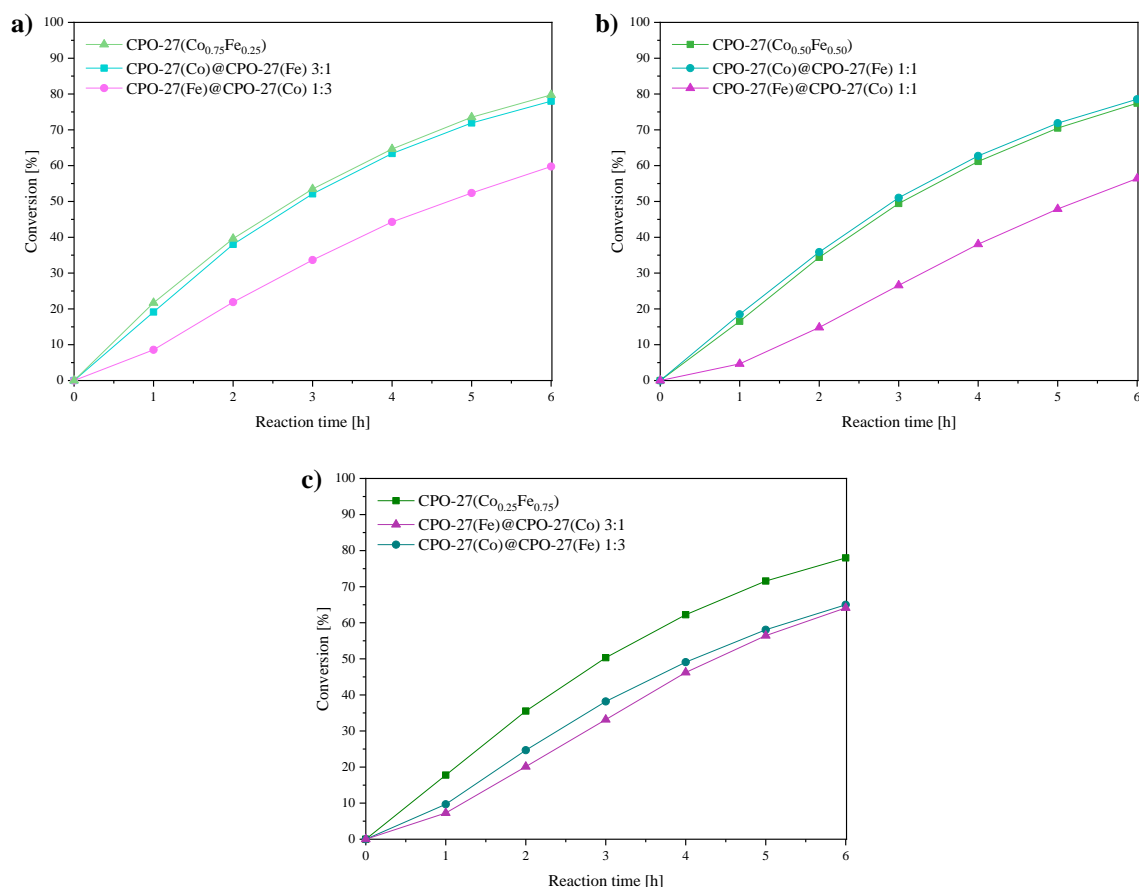


Figure 38. Comparison of CPO-27(Co,Fe) with different metal distribution and Co/Fe ratio of **a)** 3:1, **b)** 1:1 and **c)** 1:3.

3.2 Thermal decomposition of CPO-27 materials

In a subsequent project, the monometallic as well as the bimetallic CPO-27 materials were decomposed under controlled conditions in inert atmosphere. The decomposition temperature (700 °C) was chosen according to the thermogravimetric analysis results discussed in **Chapter 3.1.1**, even though the atmospheres were different (synthetic air vs. inert atmosphere). The decomposed materials were labeled Co/C and Fe/C based on monometallic CPO-27(Co) and CPO-27(Fe). The statistically distributed CPO-27(Co,Fe) materials were used for the creation of CoFe/C samples and the core-shell-structured materials were named Co@Fe/C or Fe@Co/Fe according to shell@core/C nomenclature. The decomposition in an inert atmosphere enables the creation of porous catalysts with a carbonaceous matrix around the metal species, which would be impossible to create by conventional synthesis routes.

3.2.1 Thermal decomposition of monometallic CPO-27 materials

The decomposition of CPO-27(Co) resulted in a fine black powder. According to PXRD the resulting material contained metallic Co in a cubic lattice and an amorphous carbon matrix labeled as Co/C (see **Figure 39a**). After eleven weeks of storage in air, a significant reflection at 44.5° was observable in PXRD pattern revealing that after longer time in air atmosphere the material oxidized towards Co_3O_4 (**Figure 39b**).

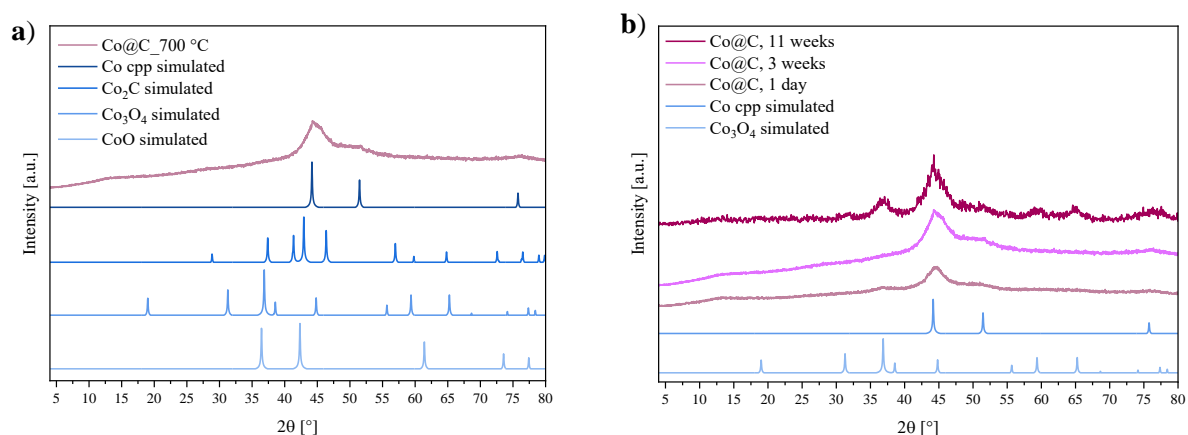


Figure 39. Powder X-ray diffraction pattern of **a**) decomposed CPO-27(Co) at 700°C under nitrogen atmosphere and the comparison with different cobalt containing crystalline phases and **b**) aging process of Co@C.

On the other hand, the PXRD results of the decomposed CPO-27(Fe) showed the formation of a highly crystalline material, which consisted of Fe_3C and cubic Fe (reflection corresponding to Fe bcc is marked by the grey area in **Figure 40**). This material underwent no changes within several months in air atmosphere and was, therefore, believed to be stable. The form of the carbonaceous matrix (amorph vs carbide) probably had an impact on the redox stability of the samples.

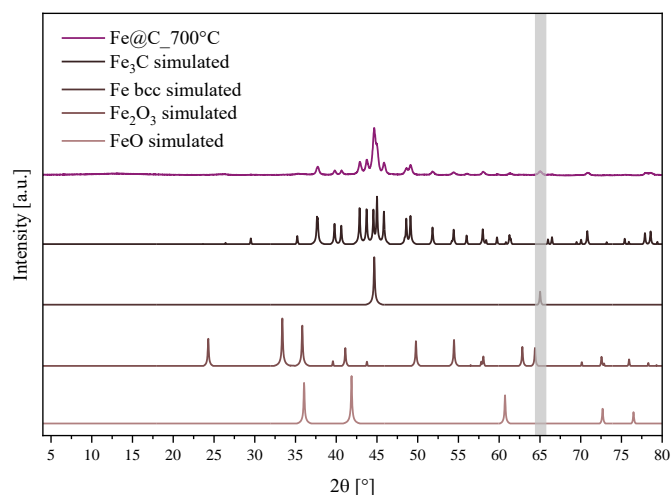


Figure 40. Powder X-ray diffraction pattern of decomposed CPO-27(Fe) at 700°C under nitrogen atmosphere and the comparison with different iron containing crystalline phases.

During the nitrogen physisorption measurements (**Figure 41**), both monometallic materials exhibited a hysteresis between the adsorption and desorption branches of the isotherm. The pore diameters were 6 nm and 8 nm for monometallic Co/C and Fe/C, respectively. The specific surface areas were $S_{\text{BET,Co/C}} = 225 \text{ m}^2/\text{g}$ and $S_{\text{BET,Fe/C}} = 240 \text{ m}^2/\text{g}$. The shape of adsorption and desorption curves indicated the presence of mesoporous materials and they were similar to each other even though the powder X-ray diffraction patterns showed a different nature of both samples. According to the ICP-OES analysis, Co/C contained 37 wt% carbon and Fe/C 35 wt% carbon, which roughly corresponded to the theoretically calculated 31%. The solvent in the pores of the initial MOF structures probably caused the difference.

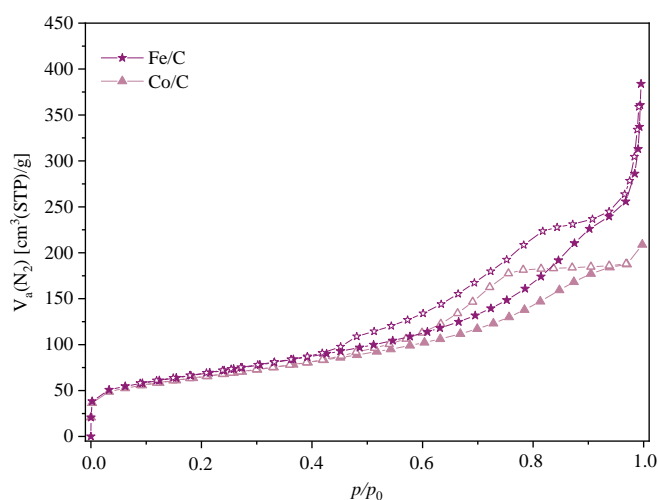


Figure 41. Nitrogen physisorption measurements of Co/C and Fe/C derived from CPO-27 analog.

3.2.2 Thermal decomposition of bimetallic CPO-27(Co,Fe) with statistical distribution

According to the PXRD data, the materials with relatively large amount of iron ($\text{Co}_{0.25}\text{Fe}_{0.75}/\text{C}$ and $\text{Co}_{0.50}\text{Fe}_{0.50}/\text{C}$) corresponded to cubic Fe or CoFe and no reflections corresponding to Fe_3C were observable. On the other hand, for $\text{Co}_{0.75}\text{Fe}_{0.25}/\text{C}$ a diffractogram was obtained, which is in agreement with oxidized forms of Co_3O_4 or Fe_3O_4 (**Figure 42**). The oxidation could be explained by differences in the aftertreatment. After the decomposition, this sample had been removed from the decomposition oven while still hot, which may have caused the oxidation. The material could also be more sensitive to oxidation due to higher Co amounts. The thermally decomposed bimetallic $\text{Co}_{0.25}\text{Fe}_{0.75}/\text{C}$ and $\text{Co}_{0.50}\text{Fe}_{0.50}/\text{C}$ materials underwent no ageing in time.

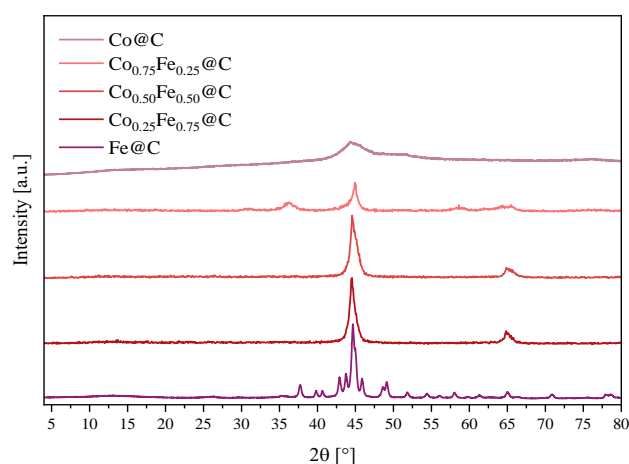


Figure 42. Powder X-ray diffraction patterns of monometallic and bimetallic CoFe@C materials after decomposition at 700°C in inert atmosphere.

Except for $\text{Co}_{0.75}\text{Fe}_{0.25}/\text{C}$, the specific surface areas of the decomposed materials were alike, showing only minor differences in values (**Table 7**). The oxidized sample had about half of the surface area ($S_{\text{BET}} = 130 \text{ m}^2/\text{g}$) of the other samples. The adsorption and desorption branches of the isotherm (**Figure 43**) showed no hysteresis for the bimetallic materials, which indirectly confirmed the creation of a truly bimetallic material, rather than the physical mixture. It seemed that during the decomposition, the spatial distribution of the metals remained the same as in the MOF precursors and no significant clusters were built.

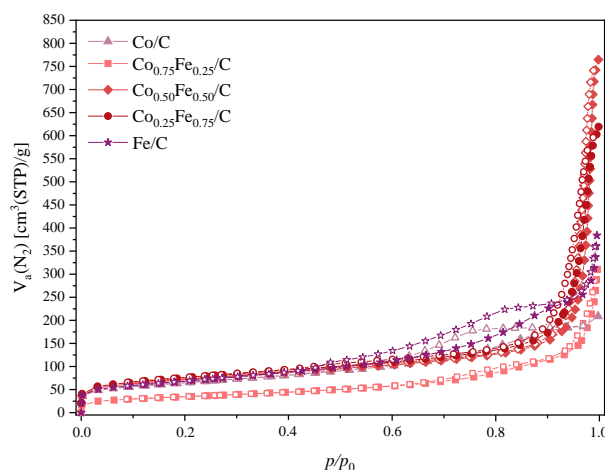


Figure 43. Results of nitrogen physisorption measurements for the monometallic references and the thermally decomposed bimetallic CPO-27(Co,Fe) materials.

All three bimetallic CoFe/C materials exhibited much larger pore diameters (16-18 nm) than the monometallic Co/C and Fe/C (6 and 8 nm). Using elemental analysis (ICP-OES), it was confirmed, that the Co/Fe ratios were almost in agreement with the desired ratio and corresponded to the MOF precursors. All materials contained also between 30-40 wt% of carbon, which roughly matched the theoretically calculated amount (31%). As in the case of monometallic materials, the difference was probably caused by the solvent molecules.

Table 7. Specific surface areas and metal ratios of decomposed samples under inert atmosphere.

Sample	Specific surface area [m ² /g]	Relative Co content [mol%]	Relative Fe content [mol%]
Co@C	225	0	100
Co _{0.75} Fe _{0.25} @C	230	78	22
Co _{0.50} Fe _{0.50} @C	250	53	47
Co _{0.25} Fe _{0.75} @C	130	29	71
Fe@C	240	100	0

3.2.3 Thermal decomposition of CPO-27(Co,Fe) materials with core-shell structure

3.2.3.1 Co@Fe/C materials decomposed from CPO-27(Co)@CPO-27(Fe)

The thermally decomposed Co@Fe/C material with a Co/Fe ratio of 1:3 corresponded, according to the PXRD (**Figure 44a**), to *Fe bcc*. With an increasing amount of Co, the

crystallinity was decreasing and the powder X-ray diffractogram changed towards *Co ccp*. The materials oxidized slightly over time and the reflections of Co_3O_4 became more visible in PXRD. The oxidation behavior of the CPO-27(Co)@CPO-27(Fe) samples indirectly supported the core-shell orientation as the outer shell consisted of CPO-27(Co), which seemed to be less stable in air.

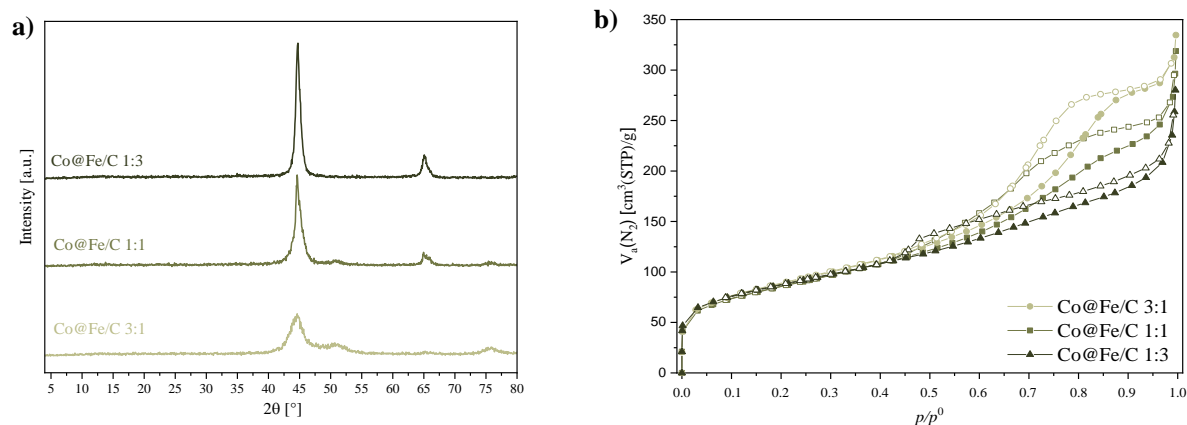


Figure 44. a) Powder X-ray diffractograms and b) nitrogen physisorption measurements of the thermally decomposed core-shell CPO-27(Co)@CPO-27(Fe) materials.

The nitrogen physisorption measurements (**Figure 44b**) showed significant differences in comparison to the measurements of the statistically distributed samples (**Figure 43**). In this case, the hysteresis between the adsorption and the desorption branch was very profound and even increasing with the cobalt amount. The hysteresis was previously assigned to monometallic materials. The specific surface area, regardless of the Co/Fe ratio was $300 \text{ m}^2/\text{g}$, which was slightly larger than for the statistically distributed samples and the pore diameter was around 5 nm. Thus, the core-shell-structured materials had a significantly smaller pore-diameter, similar to their monometallic analog. According to ICP-OES, the Co/Fe ratio was in an agreement with the previously measured CPO-27 precursors and the amount of carbon matched the theoretically calculated amount. SEM/EDX measurements, which would directly confirm the core-shell distribution, were not possible within this project.

3.2.3.2 Fe@Co/C materials decomposed from CPO-27(Fe)@CPO-27(Co)

All three Co/Fe ratios of Fe@Co/C resulted in metallic *Fe bcc* (**Figure 45a**) after the thermal decomposition. In this case, an intermetallic CoFe phase, which would feature very similar positions of the reflections, was not probable as core-shell materials have both metals spatially distributed. With increasing cobalt amount, the *Co ccp* reflections became more distinguishable and the overall crystallinity was decreasing. Unlike in the previous core-shell-structured

materials, these samples exhibited no oxidation after several months in air, regardless of the iron amount. The difference in the ageing behavior, thus, indirectly confirms the core-shell orientation, where Fe is located in the shell and, thus, preventing the oxidation.

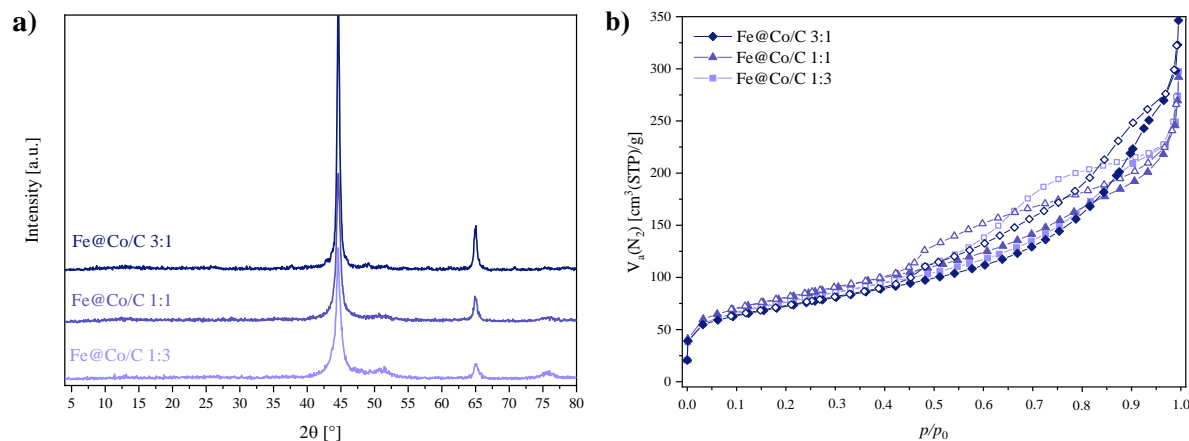


Figure 45. a) Powder X-ray diffractograms and b) nitrogen physisorption measurements for thermally decomposed core-shell CPO-27(Fe)@CPO-27(Co) materials.

Nitrogen physisorption measurements (**Figure 45b**) revealed a hysteresis for all three samples regardless of the Co/Fe ratio. It seemed that the hysteresis was typical for the core-shell materials and for the monometallic Co/C and Fe/C samples. The specific surface areas were comparable for all Fe@Co/C samples and varied from 250 m²/g to 290 m²/g. In addition, the pore diameters were similar to their Co@Fe/C and monometallic analog. Using results from ICP-OES (**Table 8**), it could be concluded that all materials have almost the same Co/Fe ratio as the respective MOF-precursors.

Table 8. Results of the elemental analysis for core-shell bimetallic materials.

Sample	Specific surface area [m ² /g]	Relative Fe content [mol%]	Relative Co content [mol%]
Fe@Co/C 3:1	250	80	20
Fe@Co/C 1:1	290	58	42
Fe@Co/C 1:3	265	34	66

In summary, the nitrogen physisorption measurements exhibited a significant difference in the isotherms according to the spatial distribution of the two metals. The isotherms of the core-shell-structured materials showed a hysteresis, which was also observable for the monometallic Co/C and Fe/C. On the other hand, the statistically distributed bimetallic materials exhibited no hysteresis, which would assume, that the spatial organization in these samples were different.

Surprisingly, the randomly distributed samples had significantly larger pore diameters than the core-shell-structured samples. ICP-OES analysis showed that the Co/Fe ratio was in agreement with the MOF precursors regardless of their metal orientation. For the confirmation of the metal distribution SEM/EDX measurements would be necessary.

3.2.4 Application of thermally decomposed MOF materials in the oxidation of benzyl alcohol

Benzyl alcohol has been chosen as a substrate for the comparison of the catalysts derived from the controlled decomposition of CPO-27-based precursors. In the case of the decomposed materials, the amount of catalyst was chosen as 0.4 mol% cobalt to substrate (and not 0.4 mol% of total metal (Co+Fe)) with respect to the substrate. This meant that the amount of active cobalt was the same in every oxidation reaction and the amount of the almost inactive iron was changed. This decision enabled the direct comparison of the decomposed materials with different metal ratios and the direct observation of possible synergy effects of the two metals.

3.2.4.1 Statistically distributed Co,Fe/C catalysts

As could be seen in **Figure 46**, Fe/C was within the first two hours inactive and after six hours only about 10 % of benzyl alcohol were oxidized. On the other hand, Co/C was highly active resulting in 73 % conversion after six hours. The statistically distributed $\text{Co}_{0.25}\text{Fe}_{0.75}/\text{C}$ and $\text{Co}_{0.50}\text{Fe}_{0.50}/\text{C}$ catalysts showed a slightly lower conversion (70 and 68 %, respectively). $\text{Co}_{0.75}\text{Fe}_{0.25}/\text{C}$, which oxidized during its aftertreatment, was treated under reducing conditions prior to the catalytic test but it exhibited a significantly lower conversion (53 %). This difference was probably caused by the limited porosity, which did not change during the additional reduction. Thus, the material was not as active as the rest of the bimetallic catalysts. According to the GC-MS data, no over-oxidation to benzoic acid was observable but *N*-benzylidenemethylamine was produced as the main side product with selectivity of 15 %. The selectivity to benzaldehyde was, regardless of the Co/Fe ratio, 46 ± 2 %. It seemed that in this case, no beneficial influence of iron in the materials could be observed.

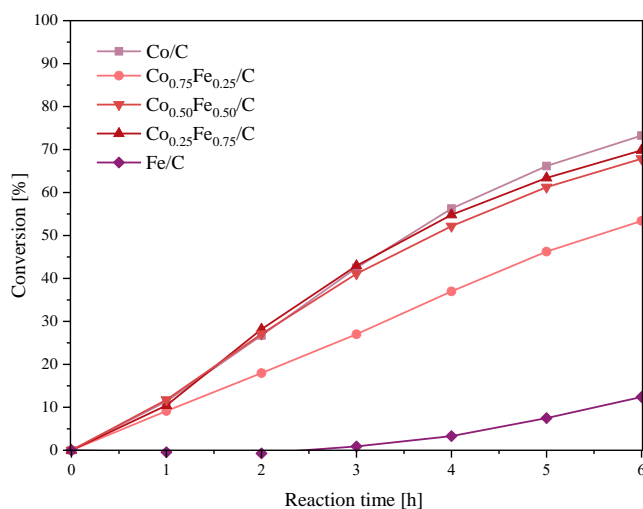


Figure 46. Catalytic results of the benzyl alcohol oxidation with statistically distributed Co,Fe/C catalysts. Parameters: 6 mmol substrate, 130 °C oil bath temperature, 200 ml/min air, 0.4 mol% cobalt in catalyst regarding to substrate amount, 60 ml DMF.

3.2.4.2 Core-shell-structured Co,Fe/C catalysts

The Co@Fe/C catalysts with a Co/Fe ratio of 1:3 and 3:1 a slightly higher conversion (80 % and 78 %) than the monometallic Co/C reference (73 %). Generally, the accuracy of the GC-MS analysis is ± 2 percent points and, thus, the differences between these two core-shell materials seemed to be not significant. Co@Fe/C 1:1 exhibited only 71 % conversion after six hours (**Figure 47a**) and is comparable to Co/C. Interestingly, all Co@Fe/C catalysts were more active than Co/C at the beginning of the oxidation and after longer reaction times, the oxidation capability of Co@Fe/C 1:1 slowed down. The selectivity to benzaldehyde was around 45 ± 2 % with *N*-benzylidenemethylamine as the main site product (selectivity 15 ± 3 %). In addition, no over-oxidation to benzoic acid was observable.

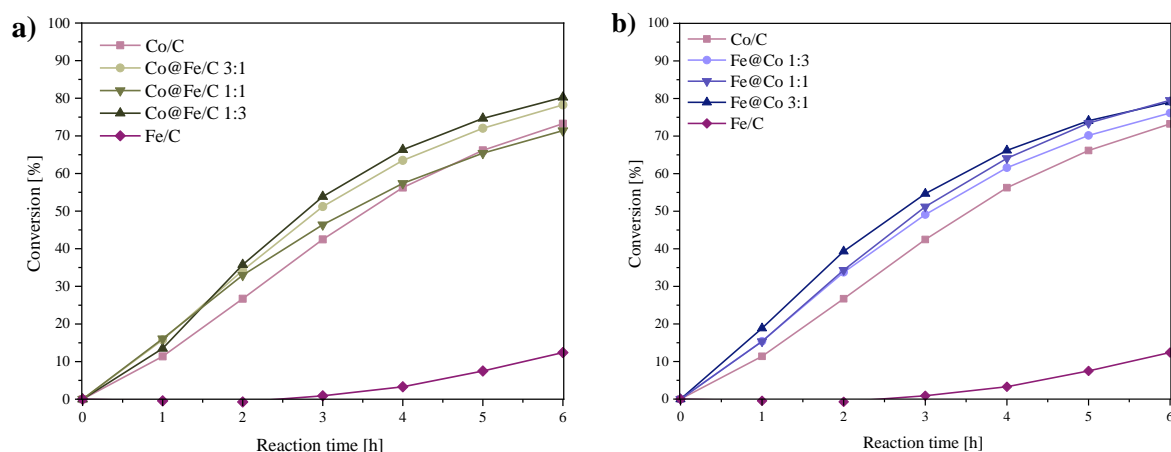


Figure 47. Liquid phase oxidation reactions of benzyl alcohol for core-shell distributed catalysts with **a)** Co@Fe/C catalysts and **b)** Fe@Co/C catalysts. Reaction conditions: 6 mmol substrate, 130 °C oil bath temperature, 200 ml/min air flow, 0.4 mol% cobalt in catalyst regarding to substrate amount, 60 ml DMF.

In the case of the Fe@Co/C materials (**Figure 47b**)), all three Co/Fe ratios featured a slightly higher activity than Co/C at the beginning of the reaction. After longer reaction times, the activity of the bimetallic catalysts decreased. After six hours Fe@Co/C 3:1 and 1:1 reached conversions of 79 % and Fe@Co/C 1:3 of 76 % but given the measurement and calibration uncertainty, the differences between the materials were not significant. The selectivity to benzaldehyde was also similar (45 ± 1 %), which meant that the order of the metals had neither an influence on selectivity nor reactivity. Also in this case, no over-oxidation to benzoic acid was observable. For future studies, it could be beneficial to choose another solvent to restrict the formation of *N*-benzylidenemethylamine.

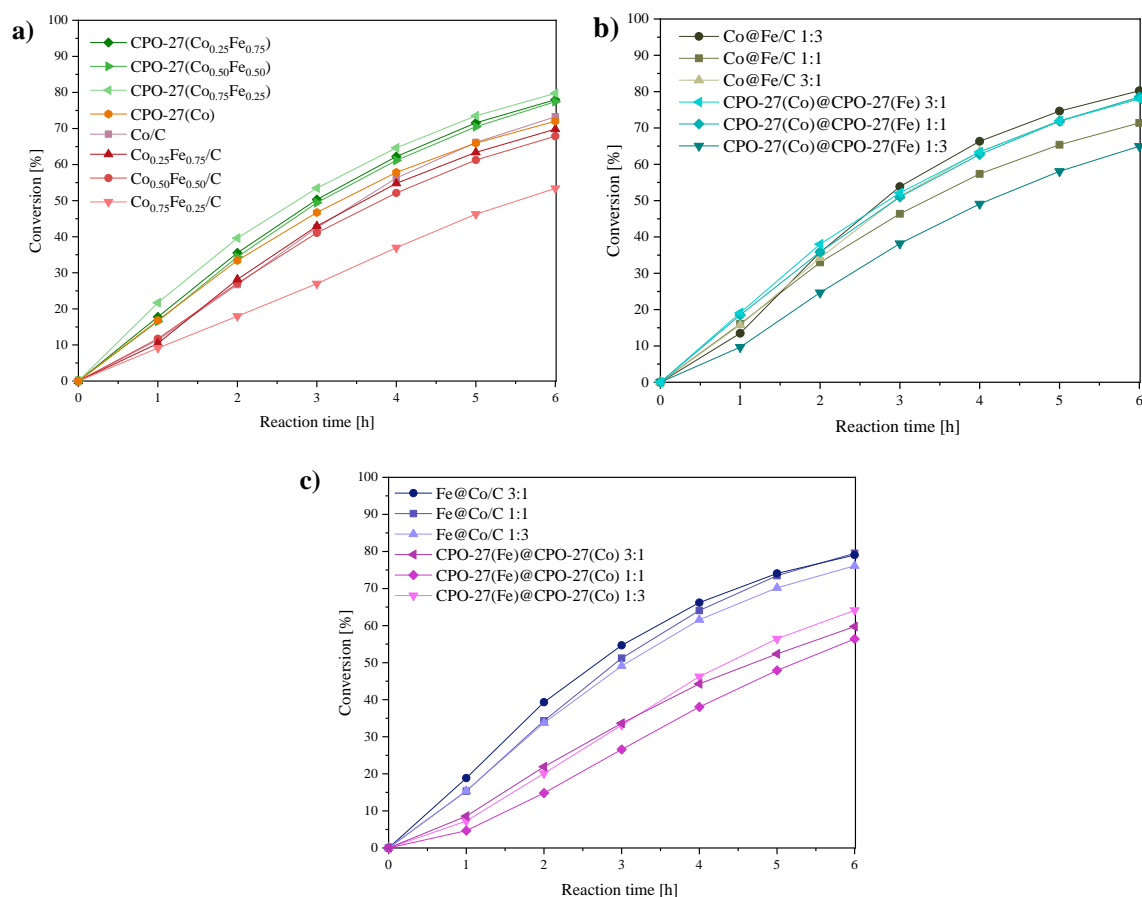


Figure 48. Liquid phase oxidation reactions of benzyl alcohol. **a)** Comparison of statistically distributed MOF precursors and corresponding decomposed materials, **b)** comparison of core-shell materials with iron in the shell and **c)** comparison of core-shell materials with cobalt in the shell. Parameters: 6 mmol substrate, 130 °C oil bath temperature, 200 ml/min air flow, 0.4 mol% cobalt in catalyst regarding to substrate amount, 60 ml DMF.

The statistically distributed CPO-27(Co,Fe) catalysts and their thermally decomposed analogs were compared in **Figure 48a)** together with CPO-27(Co) and Co/C. CPO-27(Co) exhibited almost the same activity as the decomposed analog after six hours (73 % vs 72 %). In the case of the bimetallic materials, the decomposed analogues were less active in the catalysis. The lowest activity was assigned to Co_{0.75}Fe_{0.25}/C but, as already mentioned in **Chapter 3.2.2**, this material oxidized in air and also its specific surface area was significantly lower than for all other materials. CPO-27(Co)@CPO-27(Fe) (**Figure 48b**)) did not show any trend. In the case of CPO-27(Fe)@CPO-27(Co), higher activities were reached with its decomposed analogues and the two groups (MOF vs decomposed) were clearly distinguishable (**Figure 48c**)). It seemed that in the case of Fe@Co/C, the thermal decomposition enabled a better accessibility of the catalytically active cobalt through the catalytically inactive Fe shell. The absolute amount of active cobalt in all oxidation reactions did not play an important role as assumed and the

differences between different metal ratios in one group were typically within the limits of accuracy.

3.3 Synthesis, characterization and catalytic performance of DUT-5-based materials

The aim of this project was to synthesize MOF materials containing three different linkers, namely BPDC, BPyDC and ABPDC in two different spatial distributions. Firstly, in the statistical distribution (**Chapter 3.3.1**) where all three linkers were randomly distributed (**Figure 49a**) and secondly, core-shell arrangement (**Chapter 3.3.2**) where each linker type was present only in one layer of the material (**Figure 49b**). Subsequently, these materials were used for the post-synthetic immobilization of cobalt and iron at specific sites. The resulting catalysts were then tested in oxidation of cinnamyl alcohol (**Chapter 3.3.3**) to give a mechanistic insight into the importance of spatial distribution for heterogeneous catalysts.

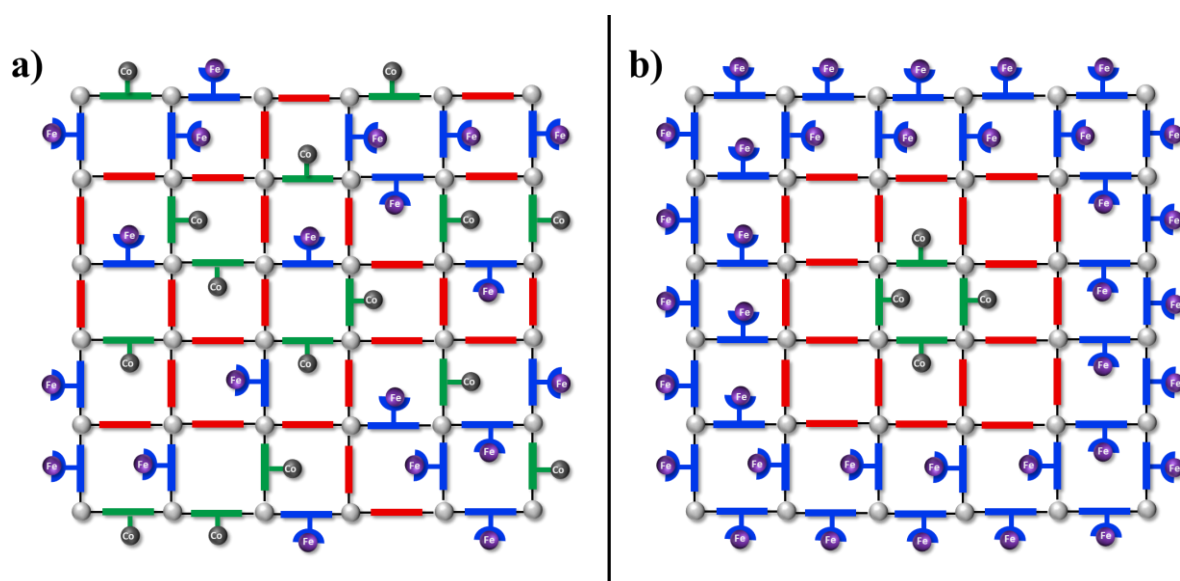
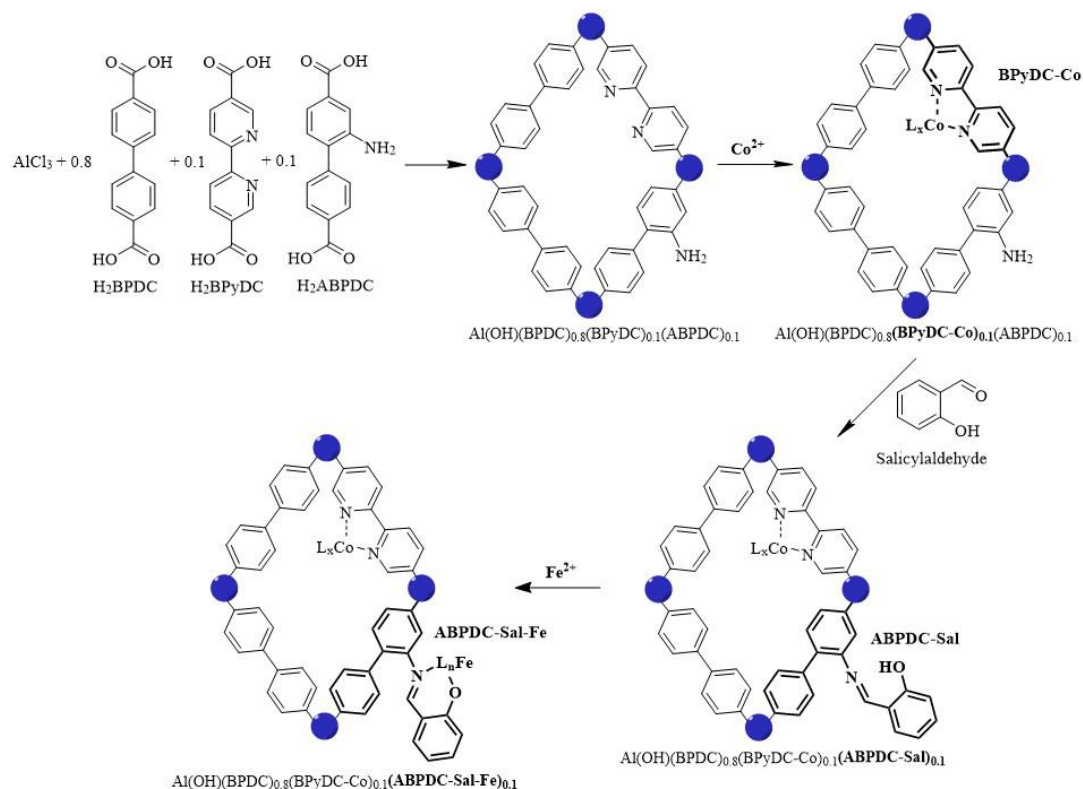


Figure 49. DUT-5-based materials with **a**) statistically distributed linkers and **b**) core-shell arrangement. Blue: ABPDC, green: BPyDC and red: BPDC.

3.3.1 DUT-5-based materials with statistical distribution

The statistically distributed materials were always synthesized using a majority of unfunctionalized linker and the same amount of both functionalized linkers. The structure synthesis was followed by a series of post synthetic modification reactions where cobalt and iron were inserted into the structure. In the first step, Co^{2+} was directly immobilized at the BPyDC linkers. In the second step, salicylaldehyde was used to modify the ABPDC linkers and

in the last step, this newly created chelating group was used for immobilization of iron (see **Scheme 5** and **Chapter 5.2.5** for more details).



Scheme 5. Four-step reaction scheme of the DUT-5-BPyDC(10)-Co-ABPDC(10)-Sal-Fe synthesis.

^1H NMR measurements of digested samples after the structure synthesis enabled the assignment of all signals to the respective hydrogen atoms in the linker molecules and also the determination of the linker ratio. The material, which should theoretically contain 80% of BPDC and 10% of each functionalized linker, contained in reality 83% of BPDC, 10% of BPyDC and 7% of ABPDC, which was in a good agreement with targeted values.

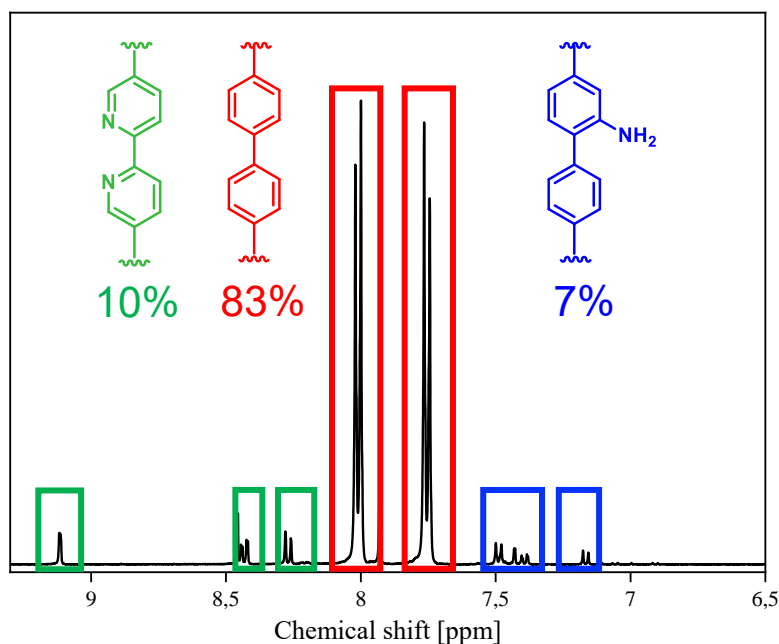


Figure 50. ^1H NMR of digested DUT-5-BPyDC(10)-ABPDC(10) sample with assigned signals of each linker.

The reaction mixture was filtered off and the resulting white powder was thoroughly washed, dried and characterized after each synthesis step. Using PXRD (**Figure 51a**) it could be concluded that the material remained highly crystalline during the whole synthesis route. The reflections were in a good agreement with the reference DUT-5 material and no additional metal phases were observable after the immobilization. Nitrogen physisorption measurements (**Figure 51b**) confirmed the high porosity of the material and that the specific surface areas were slightly decreasing (from $1770\text{ m}^2/\text{g}$ to $1450\text{ m}^2/\text{g}$) after each step (**Table 9**). This decrease was expected as the pores were partially filled with chelating groups and the immobilized metal complexes.

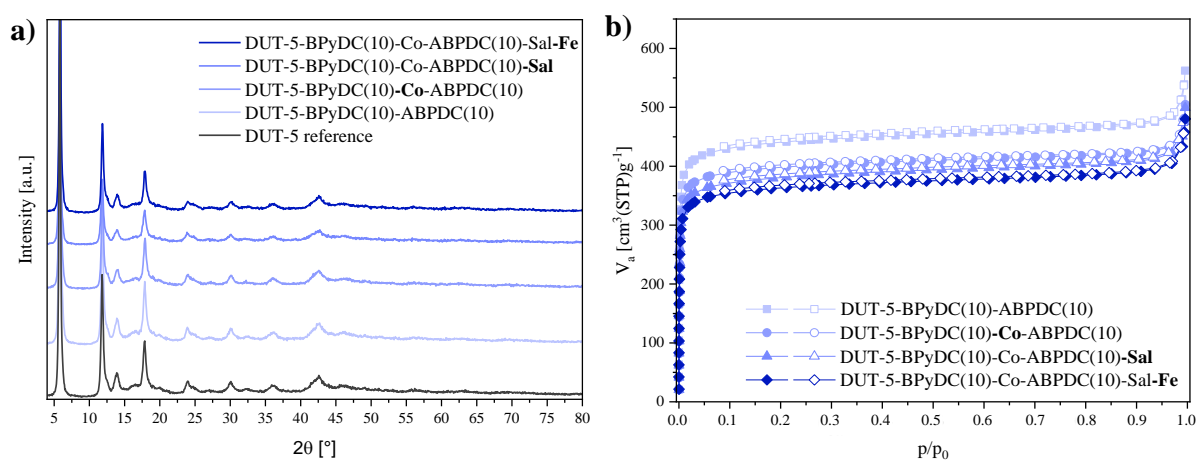


Figure 51. a) PXRD patterns and b) nitrogen physisorption measurements of statistically distributed DUT-5 materials after each synthesis step.

Using ICP-OES, the content of Co and Fe was calculated and the results showed that the cobalt amount decreased significantly after the last step of the synthesis. It seemed that cobalt was washed out during the iron immobilization. Moreover, the iron content was significantly larger than the amount of cobalt. The ICP-OES results were used to calculate which percentage of the functionalized linker molecules was used for the chelation of metal species. After the Co immobilization, 35 % of all BPyDC linkers were modified. After the PSM reaction with salicylaldehyde, 36 % of the BPyDC linkers were modified. The 1 percent point difference can be assigned to method uncertainty, showing that no cobalt was washed out during this step. On the other hand, after the iron immobilization, the amount of Co-containing BPyDC units decreased massively (from 36 % to 18 %). The degree of salicylaldehyde immobilization was only theoretically calculated as it could not completely be ruled out that iron was also partially immobilized at some of the remaining BPyDC linkers.

Table 9. Results of nitrogen physisorption and ICP-OES measurements. The amount of modified linkers represents the relative amount of functionalized linker modified with respective metal.

Catalyst	S_{BET} [m²/g]	Metal content [wt%]	Amount of modified linkers [%]
DUT-5-BPyDC(10)- ABPDC(10)	1770	-	-
DUT-5-BPyDC(10)-Co- ABPDC(10)	1620	Co: 0.40	Co: 35
DUT-5-BPyDC(10)-Co- ABPDC(10)-Sal	1540	Co: 0.42	Co: 36
DUT-5-BPyDC(10)-Co- ABPDC(10)-Sal-Fe	1450	Co: 0.21, Fe: 0.63	Co: 18, Fe: 63

ATR-IR spectra were measured after washing and drying to compare all spectra and to exclude the presence of residual molecules in the pores. All materials showed very similar spectra with only small differences, which were caused by a very low amount of post-synthetically introduced species. Two bands were of significant interest: a band at around 1685 cm⁻¹, which would indicate the presence of free linkers (C=O stretching vibrations) and a band at around 1650 cm⁻¹ which could be assigned to DMF and correspond to the C=O stretching vibration (see **Figure 52**). The results revealed that almost no free linker was present in the materials and thus, the washing with hot DMF was able to dissolve any residual linker molecules which did not participate in the structure formation. The absence of a band at 1650 cm⁻¹ meant that the

drying process was sufficient. Overall, the absence of both bands meant that the pores were not blocked for the next post-synthetic modification reactions or for the catalytic tests.

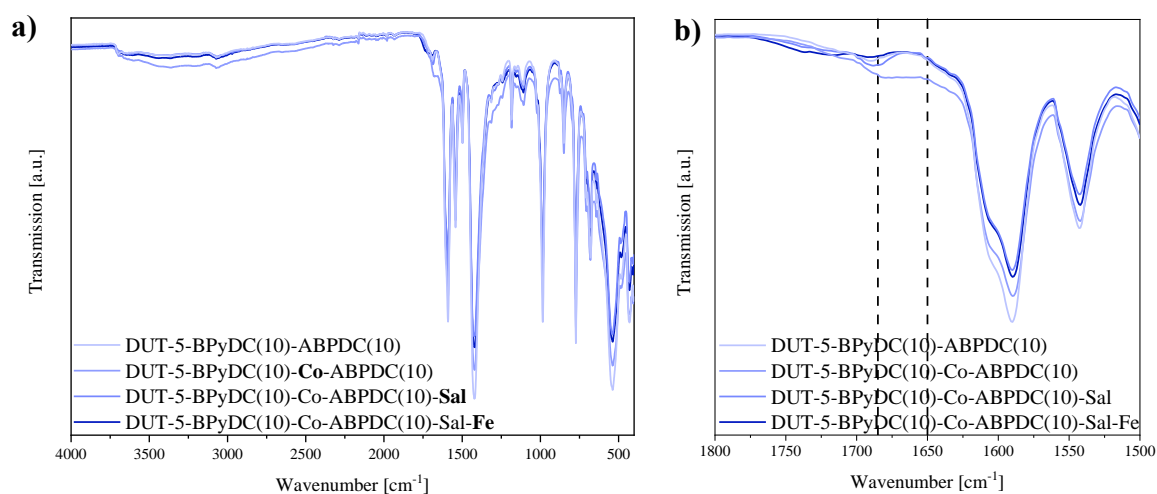
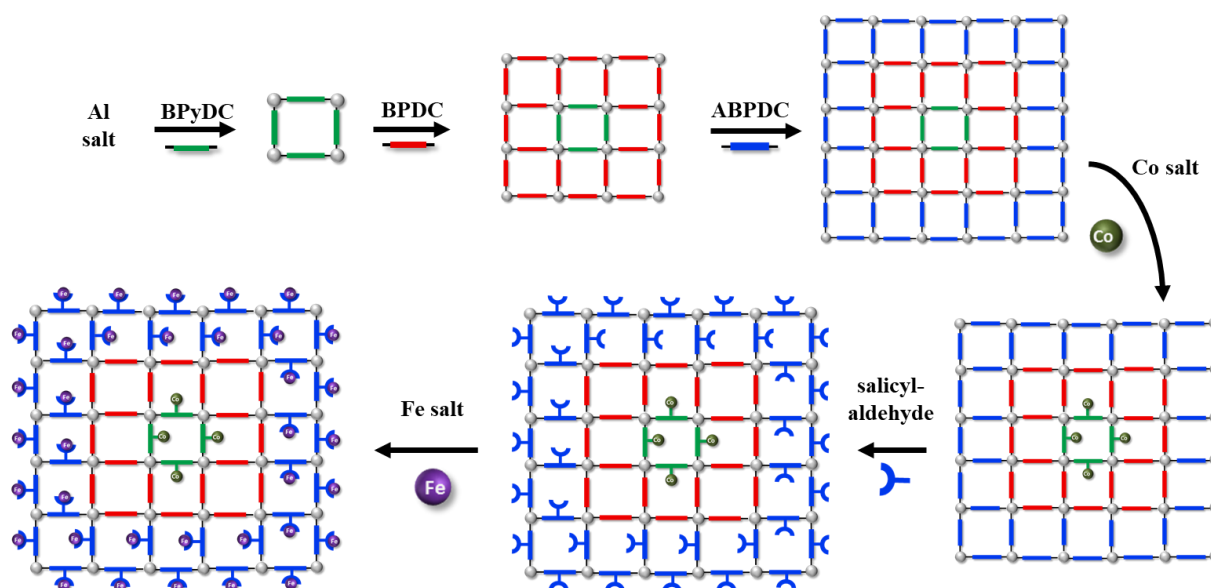


Figure 52. ATR-IR spectra of DUT-5-based materials with statistic distribution of the linkers after washing and drying. **a)** full spectra in the range of 400 – 4000 cm^{-1} **b)** zoom into the region between 1800 cm^{-1} and 1500 cm^{-1} .

3.3.2 DUT-5-based materials with core-shell structure

The aim of the core-shell-structured materials was the spatial separation of Co and Fe in the structure to investigate if close vicinity of the two metals is required for the synergistic effects. The core of the material should consist of functionalized BPyDC linker, the first shell of unfunctionalized BPDC linker and the second shell of functionalized ABPDC linker. Subsequently, a series of PSM reactions should be performed, where Co complexes would be present only in the core and Fe complexes only in the shell, spatially separated by the layer of BPDC linkers (see **Scheme 6**).



Scheme 6. Schematic representation of the synthesis of the core-shell-structured DUT-5-based material.

Initial synthesis tests revealed that the immobilization of cobalt into a MOF-253 material, which consists only of BPyDC linkers, was not possible under the applied conditions. PXRD data (**Figure 53**) showed that after the successful synthesis of MOF-253, the cobalt immobilization led to the destruction of the structure, resulting in a non-crystalline and non-porous material. Therefore, the concept of the core-shell material had to be adjusted and the core of the material consisted not only of BPyDC linkers but also of the unfunctionalized BPDC linkers. A material with 25 % BPyDC and 75 % of BPDC was chosen as a starting point.

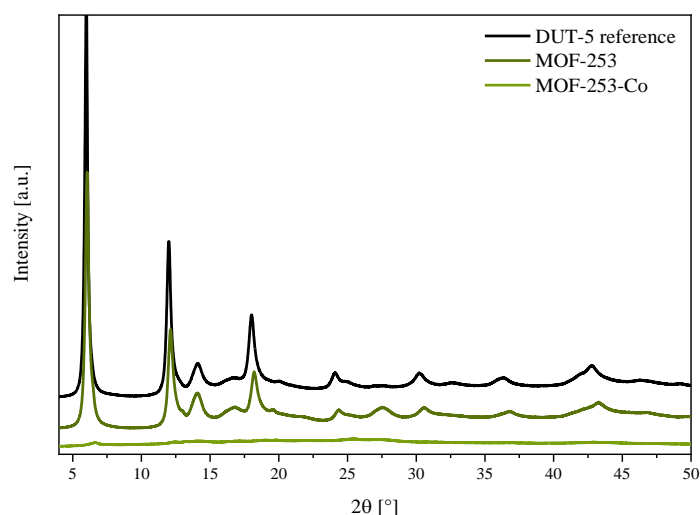


Figure 53. Powder X-ray diffraction patterns of MOF-253 before and after the cobalt immobilization and comparison with a DUT-5 reference material.

The linker ratios were determined after each layer synthesis (**Figure 54** and **Table 10**) because after the PSM reactions the NMR signals were broadened due to the presence of the metals and the exact calculations would not be possible. It was, therefore, assumed that the linker ratio did

not change during the post-synthetic modification. After the core synthesis the material should theoretically contain 25 % of BPyDC linkers and 75% of unfunctionalized BPDC linker. The measured amount was 23 % and 77 %, respectively, which was in a good agreement with the targeted values. This precursor was later mixed with aluminum chloride and BPDC linker molecules to create DUT-5@DUT-5-BPyDC(25) material with shell/core ratio of 1:1. Therefore, after the synthesis of the first shell, the sample should contain 12.5 % of BPyDC and 87.5 % of BPDC. The real determined amount was 11 % of BPyDC and 89 % of BPDC.

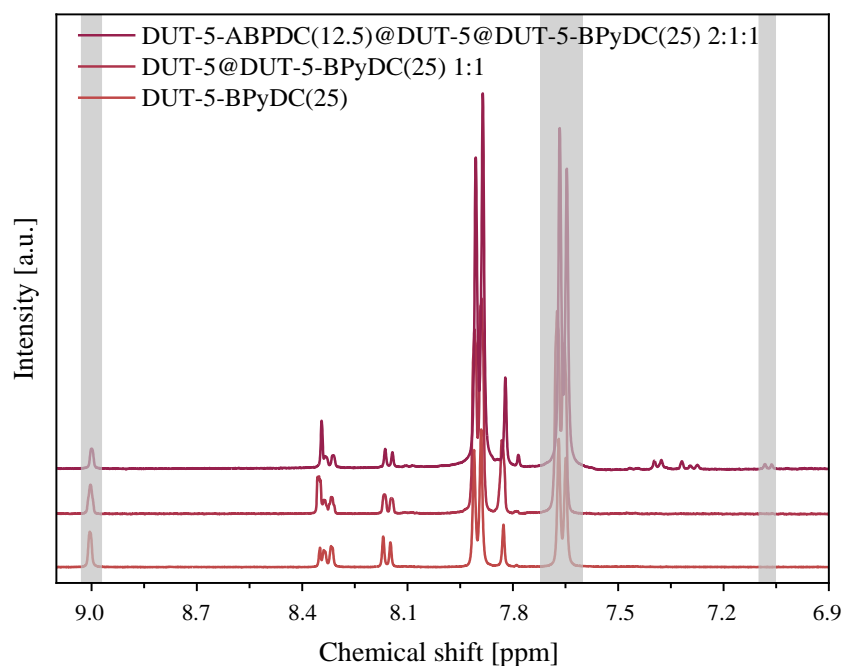


Figure 54. ^1H NMR of digested core-shell DUT-5-based samples after the creation of each layer. Grey areas represent hydrogen signals used for calculations – 9.0 ppm corresponds to BPyDC, 8.65 ppm to BPDC and 7.1 ppm to ABPDC.

During the synthesis of the second shell unfunctionalized BPDC linkers and functionalized ABPDS linkers were used. The complete synthesis of the DUT-5-based core-shell-structured material aimed at 6.5 % BPyDC, 6.5 % ABPDC and 87 % BPDC but after the synthesis of the second shell, the amount of functionalized linkers was larger than desired: 9 % of BPyDC and 12 % of ABPDC. It seemed that almost all ABPDC molecules were used during the synthesis for the creation of a shell but only a limited amount of the unfunctionalized linkers (BPDC) were incorporated. Therefore, the amount of the functionalized linkers with respect to the unfunctionalized BPDC was higher than expected.

According to the PXRD data, the crystallinity of the material decreased slightly after the synthesis of the first shell (**Figure 55a**) and increased again after the synthesis of the second shell. Cobalt immobilization led to a decrease in crystallinity but no additional crystalline

phases were observable. The salicylaldehyde incorporation seemed to have a positive influence on the crystallinity. After the last step of the synthesis, the crystallinity decreased significantly. However, the reflections corresponding to the DUT-5 structure were still observable and no additional reflections were observed.

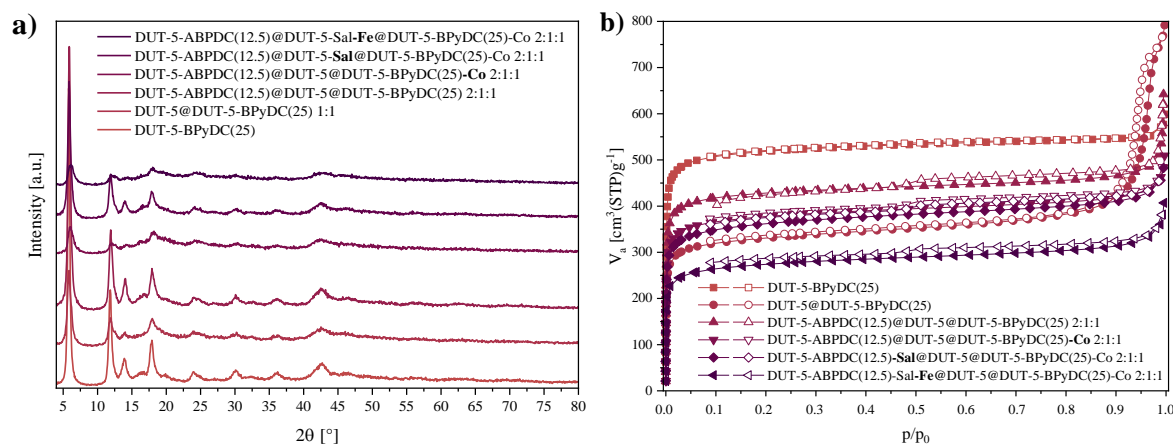


Figure 55. a) Powder X-ray diffraction patterns and b) N₂ physisorption isotherms after each synthesis step of DUT-5-based core-shell material.

The nitrogen physisorption measurements (**Figure 55b**) revealed type I isotherms corresponding to microporous materials. In addition, the average pore size was calculated as 2 nm after each synthesis step and did not decrease during the post synthetic modification reactions. The specific surface areas presented in **Table 10** were decreasing with each synthesis step. The only exception was the material after the synthesis of the first shell, where the specific surface area and also the crystallinity decreased significantly. However, after the synthesis of the next layer, the specific surface area of the material increased. This was probably caused by insufficient washing and drying of the material during aftertreatment. At the end, after all PSM reactions, a white-grey powder was obtained with a specific surface area S_{BET} of 1070 m²/g. Even though, the material was not as crystalline as the statistically distributed analogue, the material was still highly porous with micropores and, therefore, the material was suitable for the subsequent catalytic testing. ICP-OES analysis was performed to determine the amount of both metals and to calculate how much of the material would be needed for the catalysis (**Table 10**).

Table 10. Relative amount of functionalized linkers, specific surface areas and metal content of DUT-5-based core-shell-structured materials obtained via ^1H NMR, nitrogen physisorption and elemental analysis (ICP-OES), respectively.

Catalyst	^1H NMR	S_{BET} [m ² /g]	Metal content [wt%]	Amount of modified linkers [%]
DUT-5-BPyDC(25)	23 % BPyDC	2060	-	-
DUT-5@DUT-5- BPyDC(25) 1:1	11 % BPyDC	1300	-	-
DUT-5-ABPDC(12.5)@ DUT-5@DUT-5- BPyDC(25) 2:1:1	9 % BPyDC, 12 % ABPDC	1710	-	-
DUT-5-ABPDC(12.5)@ DUT-5@DUT-5- BPyDC(25)-Co 2:1:1	-	1480	Co: 0.64	Co: 73
DUT-5-ABPDC(12.5)-Sal @DUT-5@DUT-5- BPyDC(25)-Co 2:1:1	-	1400	Co: 0.99	Co: 92
DUT-5-ABPDC(12.5)-Sal- Fe@DUT-5@DUT-5- BPyDC(25)-Co 2:1:1	-	1070	Co: 0.17, Fe: 0.68	Co: 16, Fe: 66

After the cobalt immobilization, 73% of all BPyDC linkers present in the materials carried cobalt atoms. However, after the PSM reaction with salicylaldehyde, the cobalt amount increased, which was not possible as salicylaldehyde contained no cobalt. The only explanation of such a behavior was that one of the measurements did not correspond to the real amount of Co. Therefore, it could only be concluded that during the iron incorporation, the amount of cobalt decreased significantly, meaning it was washed out during the last synthesis step as observable for statistically distributed analog.

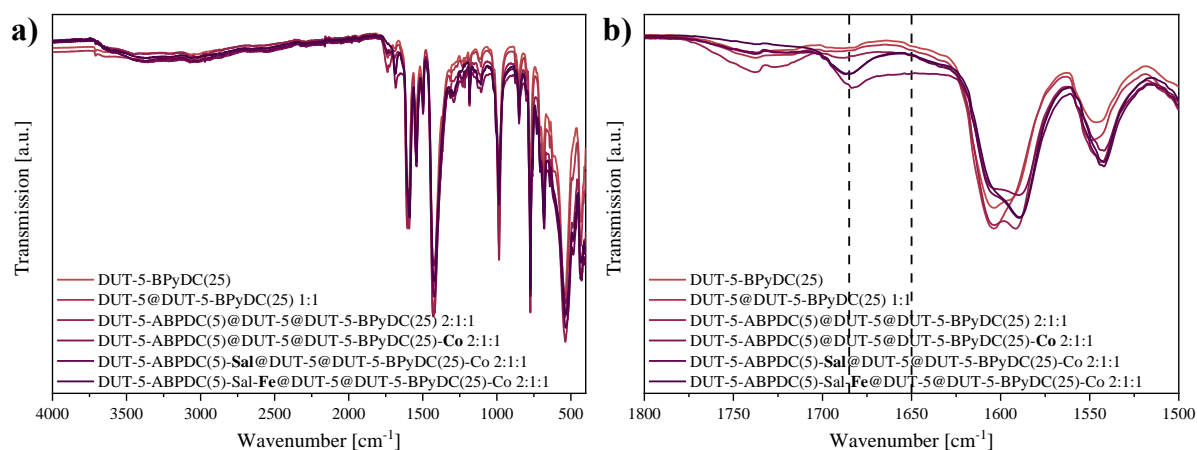


Figure 56. ATR-IR spectra of core-shell-structured DUT-5 after each synthesis step.

ATR-IR spectra were measured to investigate the presence or absence of free linker molecules (C=O stretching vibrations at around 1685 cm^{-1}) or DMF (C=O stretching vibrations at around 1650 cm^{-1}) in the pores (see **Figure 56**). It seemed that especially the materials after the PSM steps (Co immobilization, salicylaldehyde incorporation and Fe immobilization) contained some free linker molecules. As no linker molecules were added during the according syntheses, the bands would indicate that the minor amounts of the crystalline material were decomposed during these steps. Moreover, hot DMF could not be used for the washing process because the structure would decompose completely under these conditions. As a result, free linkers could not be removed completely.

To compare the catalytic activity of the statistically distributed materials and the core-shell-structured samples, the percentage of modified linkers should be similar. Therefore, the syntheses were planned accordingly. After all PSM reactions, 18 % of BPyDC were modified for the statistically distributed material and 16 % for the core-shell material. 66 % and 63 % of ABPDC linkers were chelated with iron on the statistically distributed material and the core-shell material, respectively.

3.3.3 Application of DUT-5 materials in oxidation of cinnamyl alcohol

The oxidation of cinnamyl alcohol was performed using the same parameters as for benzyl alcohol. Cinnamyl alcohol is a primary alcohol with an additional double bond and, thus, can be oxidized not only at the hydroxyl groups but also of the C=C double bond. The main product of the oxidation can, therefore, be cinnamaldehyde or 3-phenylglycidol. The results showed in **Figure 57** proved that the reference material was more active than the catalyst with statistic distribution. Both of the catalysts were highly active and full conversion was obtained after

4 hours for DUT-5-BPyDC(10)-Co and after 6 hours for the DUT-5-BPyDC(10)-Co-ABPDC(10)-Sal-Fe. The core-shell analog showed a significantly lower activity reaching only 62 % after six hours.

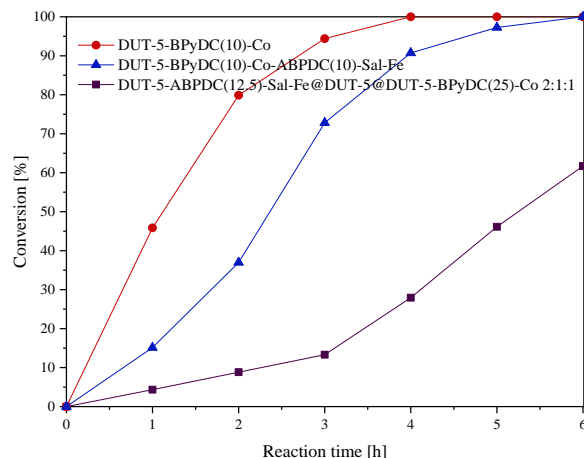


Figure 57. Catalytic results of cinnamyl alcohol oxidation for DUT-5-based catalysts. Reaction parameters: 2 mmol substrate, 130 °C oil bath temperature, 200 ml/min air flow, 0.01 mol% cobalt in catalyst with respect to substrate amount, 30 ml DMF.

The selectivities to the two main products (and benzaldehyde) (**Figure 58**) were compared at about 40 % conversion for the three catalysts. The highest selectivity to cinnamaldehyde (24 %) was obtained for DUT-5-BPyDC(10)-Co. The highest 3-phenylglycidol selectivity (18 %) was reached with the core-shell-structured DUT-5-ABPDC(12.5)-Sal-Fe@DUT-5@DUT-5-BPyDC(25)-Co 2:1:1. During the reaction, also other side products were observable such as benzaldehyde (calibrated), hydrocinnamylalcohol (after even longer reaction times), 2-phenylpropanal and phenylacetaldehyde (both not calibrated).

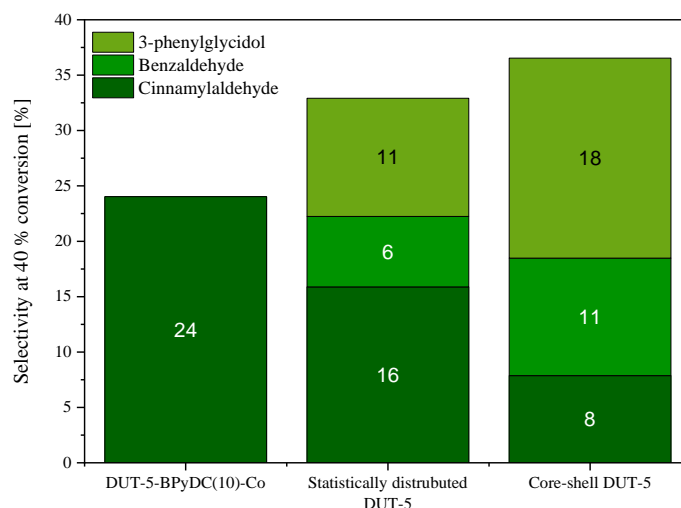


Figure 58. Product selectivity to cinnamaldehyde, benzaldehyde and 3-phenylglycidol at 40 % conversion for the three catalysts.

Overall, the statistically distributed material exhibited a high catalytical activity, which was comparable or slightly lower than for the monometallic Co reference system. The core-shell material displayed a significantly lower conversion, meaning that the cobalt-containing core was probably hardly accessible for the substrate molecules. Moreover, the close vicinity of Co and Fe was necessary for highly active systems. Even though, the aim of the work was to synthesize more active catalysts than the reference (which was not successful) it could be still concluded that the seven-step synthesis of the core-shell material was successful.

4 Summary and Conclusions

In this thesis, bimetallic CPO-27 and DUT-5 materials containing Co and Fe were prepared. CPO-27(Co,Fe) materials were synthesized with three different Co/Fe ratios and two different spatial distributions of the two metals. A novel direct synthesis was developed for bimetallic CPO-27(Co,Fe). In the first phase of the project, statistically distributed MOFs were synthesized and PXRD analysis revealed that the resulting materials were highly crystalline and that both metals were incorporated into the structure. The thermal stability of all bimetallic materials was between the values for monometallic CPO-27(Co) and CPO-27(Fe) and the structural decomposition started around 170 °C for all Co/Fe ratios. Elemental analysis (ICP-OES) revealed that the materials contained slightly more cobalt than targeted. Core-shell-structured CPO-27(Co)@CPO-27(Fe) and CPO-27(Fe)@CPO-27(Co) were also synthesized with the same Co/Fe ratios. PXRD confirmed the crystallinity of all materials and the resulting diffractograms corresponded to the CPO-27 structure. Calculations based on the ICP-OES results showed that in both cases the cores were slightly smaller than desired.

Catalytic tests of these CPO-27-based catalysts were performed using the oxidation of 1-phenylethanol and benzyl alcohol as target reactions. The results were compared to a highly active CPO-27(Co) material and the almost inactive CPO-27(Fe). In general, the statistically distributed materials and core-shell-structured CPO-27(Co)@CPO-27(Fe) catalysts were more active in the oxidation reaction of benzyl alcohol than monometallic CPO-27(Co) and thus, the presence of iron in the structure was beneficial. CPO-27(Fe)@CPO-27(Co) on the other hand, was less active than CPO-27(Co) regardless of the Co/Fe ratio. This behavior could be explained by the different accessibility of the catalytically active cobalt due to the different spatial orientations.

In the second part of the thesis, CPO-27(Co,Fe) materials were transformed into bimetallic Co,Fe-based catalysts within a porous carbonaceous matrix *via* MOF-mediated synthesis. PXRDs of the thermally decomposed bimetallic materials showed that materials with a statistical distribution of the two metals corresponded to a CoFe alloy. The specific surface areas (with the exception of one oxidized material) were comparable to the monometallic Co/C and Fe/C references. The core-shell-structured materials revealed that both Co@Fe/C and Fe@Co/C corresponded to Fe *bcc* for larger iron content and Co *ccp* for larger Co content. Co@Fe/C was oxidized after long-term storage in air probably due to exposed Co species,

confirming the difference between the two core-shell materials. During the benzyl alcohol oxidation, it was found out that statistically distributed Co,Fe MOF materials were more active than their thermally decomposed analogs. Moreover, the Fe@Co/C catalysts were more active than their MOF precursors in the benzyl alcohol oxidation.

In the final part of the PhD project, DUT-5 based catalysts were also synthesized with both distributions. The statistically distributed DUT-5-BPyDC(10)-Co-ABPDC(10)-Sal-Fe contained 10 % of BPyDC, 7 % of ABPDC and 83 % of BPDC according to ^1H NMR. PXRD confirmed the DUT-5 structure, even though the crystallinity was slightly decreasing after each synthesis step. Nitrogen physisorption showed a type I isotherm with decreasing specific surface areas after each synthesis step as the pores were occupied with cobalt, salicylaldehyde and iron. Elemental analysis revealed that only 35% of all BPyDC linkers were modified with cobalt and after iron immobilization this amount decreased significantly. Infrared spectroscopy confirmed that no free linker or DMF molecules were present in the pores after the synthesis.

DUT-5-ABPDC(12.5)-Sal-Fe@DUT-5@DUT-5-BPyDC(25)-Co 2:1:1 was stepwise synthesized to obtain a core-shell-structured analog of the material with statistic distribution. The Co-containing core and the Fe-containing outer shell were separated by an unfunctionalized first shell to avoid a close contact of the two metals in this material. According to ^1H NMR the core-shell-structured material contained 9 % of BPyDC and 12 % of ABPDC. As in the previous case, the crystallinity, the specific surface area and the porosity were steadily decreasing. The cobalt amount decreased significantly after the iron immobilization and free linker molecules were detected in the infrared spectra. This confirmed that the structure slightly decomposed after each PSM step.

Both materials and a monometallic DUT-5-BPyDC(10)-Co reference material were used in oxidation of cinnamyl alcohol. DUT-5-BPyDC(10)-Co and DUT-5-BPyDC(10)-Co-ABPDC(10)-Sal-Fe were highly active in the oxidation of cinnamyl alcohol. A full conversion of 100 % was reached already after 4 hours for the monometallic catalyst and after 6 hours for the catalyst with statistic distribution. The core-shell-structured catalyst reached only 62 % conversion after six hours. The main products of the cinnamyl alcohol oxidation were: cinnamaldehyde, 3-phenylglycidol, benzyl alcohol, hydrocinnamylalcohol, phenylacetaldehyde and 2-phenylpropanal.

In summary, novel Co, Fe-containing materials were synthesized and thoroughly characterized. Co and Fe were incorporated on equivalent as well as non-equivalent positions within the

catalysts and their catalytic performance was tested during oxidation reactions of alcohols. The results revealed that the presence of iron could decrease the amount of highly active cobalt in catalysts retaining (in some cases) the catalytic activity.

5 Experimental part

5.1 Chemicals

All chemicals used for synthesis and catalysis were purchased from Alfa Aesar, abcr, Merck, Fisher Scientific or TCI. An exception was 2-amino-4,4'-biphenyldicarboxylic acid which was synthesized in Karlsruhe Institute of Technology by the group of professor Bräse. All chemicals were used without further purification or drying.

5.2 Syntheses

5.2.1 Monometallic CPO-27 materials

Synthesis of CPO-27(Co): 2,5-Dihydroxyterephthalic acid (0.2774 g, 1.4 mmol, 1.00 eq) was dissolved in 49.5 ml *N,N*-dimethylformamide (DMF). Cobalt(II) nitrate hexahydrate (0.8154 g, 2.8 mmol, 2.00 eq) was dissolved in 5.5 ml water. Both solutions were combined and stirred in a sealed glass vessel at 120 °C in an oil bath for 24 hours. The resulting material was separated from the hot suspension by using a glass filter, washed 2 x 20 ml of DMF and 1 x 20 ml water and dried in air at a room temperature.

Synthesis of CPO-27(Fe): 2,5-Dihydroxyterephthalic acid (0.1486 g, 0.75 mmol, 1 eq) was weighed into round-bottom flask under air atmosphere. The flask was inserted into a glovebox, where iron(II) acetate anhydrous (0.2609 g, 1.4 mmol, 2 eq) was added under inert gas atmosphere. Afterwards, 9 ml of *N*-methylpyrrolidone (NMP) and 4.5 ml of water were filled into the flask under nitrogen and stirred for 18 hours at 130 °C under inert condition (nitrogen). The solid was separated from the hot suspension by using a glass filter, washed with 3 x 20 ml of NMP and dried in air at room temperature. The resulting material was stored under air atmosphere.

5.2.2 CPO-27-based materials with statistical distribution

Synthesis of CPO-27(Co_x,Fe_{1-x}) via post-synthetic exchange: Monometallic CPO-27(Co) (0.2000 g, 0.6413 mmol, 1 eq) was dissolved in 20 ml of *N,N*-dimethylformamide (DMF) for 3 hours at 100 °C in a sealed glass vessel. Iron(II) chloride tetrahydrate was dissolved in 2 ml of H₂O and later added to the solution of CPO-27(Co). The whole mixture was stirred for 24 hours at 100 °C in a sealed glass vessel. The resulting material was separated from the hot

suspension by using a glass filter, washed with 2 x 20 ml of NMP and 2 x 20 ml of ethanol and dried in air at room temperature. The specific amount of iron(II) chloride tetrahydrate can be seen in **Table 11**.

Table 11. Masses and molar amounts of iron(II) chloride tetrahydrate for the synthesis of CPO-27(Co_x,Fe_{1-x}) materials.

Synthesized material	FeCl ₂ ·4H ₂ O
	0.2550 g
CPO-27(Co_{0.25},Fe_{0.75})	1.2826 mmol 2 eq
	0.1275 g
CPO-27(Co_{0.50},Fe_{0.50})	0.6413 mmol 1 eq
	0.0637 g
CPO-27(Co_{0.75},Fe_{0.25})	0.3207 mmol 0.5 eq

Direct synthesis of CPO-27(Co_x,Fe_{1-x}): 2,5-Dihydroxyterephthalic acid (0.1486 g, 0.75 mmol, 1.00 eq) and cobalt(II) nitrate hexahydrate were weighed under air atmosphere into a round-bottom flask. The flask was inserted into a glovebox, where iron(II) acetate anhydrous was added under inert atmosphere (nitrogen). Afterwards, 4.5 ml of *N*-methylpyrrolidone (NMP), 4.5 ml of *N,N*-dimethylformamide (DMF) and 4.5 ml of water were filled into the flask under nitrogen and stirred for 18 hours at 130 °C under inert atmosphere (nitrogen). The specific amounts of metal salts for each Co/Fe ratio are presented in **Table 12**. The solid was separated from the hot suspension by using a glass filter, washed with 3 x 20 ml of NMP and dried in air at room temperature.

Table 12. Masses and molar amounts of metal salts for the direct synthesis of CPO 27($\text{Co}_x\text{Fe}_{1-x}$) materials.

Synthesized material	$\text{Fe}(\text{C}_2\text{H}_3\text{O}_2)_2$	$\text{Co}(\text{NO}_3)_2 \cdot 6\text{H}_2\text{O}$
CPO-27($\text{Co}_{0.25}\text{Fe}_{0.75}$)	0.1957 g	0.1091 g
	1.125 mmol	0.375 mmol
	1.5 eq	0.5 eq
CPO-27($\text{Co}_{0.50}\text{Fe}_{0.50}$)	0.1304 g	0.2183 g
	0.75 mmol	0.75 mmol
	1 eq	1eq
CPO-27($\text{Co}_{0.75}\text{Fe}_{0.25}$)	0.0652 g	0.3274 g
	0.375 mmol	1.125 mmol
	0.5 eq	1.5 eq

5.2.3 CPO-27-based materials with core-shell structure

In this work, both possible orders of CPO-27(Fe) and CPO-27(Co) in a core-shell structure were synthesized. The first one was **CPO-27(Fe)@CPO-27(Co)**, with CPO-27(Co) in the core was synthesized using the previously mentioned synthesis from Chapter 5.2.1. After that, the core and 2,5-dihydroxyterephthalic acid were weighted into a round-bottom flask and inserted into glovebox, where iron(II) acetate anhydrous was added under inert gas atmosphere. Afterwards, 36 ml of NMP and 18 ml of water were filled into the flask under nitrogen and stirred for 18 hours at 130 °C under inert condition (nitrogen). The solid was separated from the hot suspension by using a glass filter, washed with 3 x 20 ml of NMP and dried in air at room temperature. The resulting material was stored under air atmosphere. The specific amounts of chemicals for each Co/Fe ratio is presented in **Table 13**.

Table 13. Masses and molar amounts of core, linker and iron salt for core-shell CPO-27(Fe)@CPO-27(Co) materials with different core-shell ratios.

Synthesized material	Core	Linker	Fe(C ₂ H ₃ O ₂) ₂
CPO-27(Fe)@CPO-27(Co) 3:1	0.3119 g	0.5944 g	1.0436 g
	1 mmol	3 mmol	6 mmol
	1 eq	3 eq	6 eq
CPO-27(Fe)@CPO-27(Co) 1:1	0.6237 g	0.3963 g	0.6957 g
	2 mmol	2 mmol	4 mmol
	2 eq	2 eq	4 eq
CPO-27(Fe)@CPO-27(Co) 1:3	0.9356 g	0.1981 g	0.3479 g
	3 mmol	1 mmol	2 mmol
	3 eq	1 eq	2 eq

The second core-shell material, **CPO-27(Co)@CPO-27(Fe)**, with CPO-27(Fe) in the core was synthesized using the previously mentioned synthesis from Chapter 5.2.1. After that, the core, 2,5-dihydroxyterephthalic acid and cobalt(II) nitrate hexahydrate were weighted into a reaction vessel under air atmosphere. Afterwards, 60 ml DMF and 30 ml water were added and the mixture was stirred for 24 hours at 130 °C in an oil bath. The solid was separated from the hot suspension by using a glass filter, washed once with 20 ml water and 3 x 20 ml of DMF and dried in air at room temperature. The resulting material was stored under air atmosphere. The specific amounts of chemicals for each Co/Fe ratio is presented in **Table 14**.

Table 14. Masses and molar amounts of core, linker and cobalt salt for core-shell CPO-27(Co)@CPO-27(Fe) materials with different core-shell ratios.

Synthesized material	Core	Linker	Co(NO ₃) ₂ · 6H ₂ O
CPO-27(Fe)@CPO-27(Co) 3:1	0.5000 g	0.9723 g	2.8561 g
	1.64 mmol	4.9 mmol	9.84 mmol
	1 eq	3 eq	6 eq
CPO-27(Fe)@CPO-27(Co) 1:1	1.000 g	0.6482 g	1.9041 g
	3.27 mmol	3.27 mmol	6.54 mmol
	1 eq	1 eq	2 eq
CPO-27(Fe)@CPO-27(Co) 1:3	1.5000 g	0.3241 g	0.9520 g
	4.9 mmol	1.64 mmol	3.27 mmol
	3 eq	1 eq	2 eq

5.2.4 Thermal decomposition of CPO-27 materials

CPO-27 precursors were thermally decomposed under inert atmosphere. Quartz wool was inserted into a glass tube and a known amount of MOF precursor was placed into the tube. The tube was then adjusted vertically in a reduction oven and inert gas was flushed for 10 minutes with a flow rate of 10 ml/min. Afterwards, the total flow rate of 100 ml/min was adjusted. The oven was heated with a heating rate of 5 K/min up to 700 °C and held for one hour. Afterwards, the oven was cooled to room temperature under inert atmosphere.

5.2.5 DUT-5-based materials with statistical distribution

Synthesis of DUT-5-BPyDC(10)-ABPDC(10): 4,4'-biphenyldicarboxylic acid (0.6104 g, 2.52 mmol, 8 eq), 2-amino-4,4'-biphenyldicarboxylic acid (0.0811 g, 0.315 mmol, 1 eq), 2,2'-bipyridine-5,5'-dicarboxylic acid (0.0769 g, 0.315 mmol, 1 eq) and aluminum chloride hexahydrate (AlCl₃·6H₂O, 0.7605 g, 3.15 mmol, 10 eq) were mixed with 50 ml of DMF and stirred in a sealed glass vessel at 120 °C in an oil bath for 24 hours. After the synthesis, the material was filtered off in hot state and washed with 3 x 20 ml of hot (100 °C) DMF and dried at 130 °C for three days.

Synthesis of DUT-5-BPyDC(5)-ABPDC(5) was an analog to the previously described synthesis, only the ratios were adjusted to targeted linker ratio. 4,4'-biphenyldicarboxylic acid (0.6867 g, 2.835 mmol, 9 eq), 2-amino-4,4'-biphenyldicarboxylic acid (0.0405 g, 0.1575 mmol, 0.5 eq), 2,2'-bipyridine-5,5'-dicarboxylic acid (0.0385 g, 0.1575 mmol, 0.5 eq) and aluminum chloride hexahydrate ($\text{AlCl}_3 \cdot 6\text{H}_2\text{O}$, 0.7605 g, 3.15 mmol, 10 eq) were mixed with 50 ml of DMF and stirred in a sealed glass vessel at 120 °C in an oil bath for 24 hours. After the synthesis, the material was filtered off in hot state and washed with 3 x 20 ml of hot (100 °C) DMF and dried at 130 °C for three days.

5.2.6 DUT-5-based materials with core-shell distribution

Two materials with different core-shell-shell ratios and linker amount were synthesized. DUT-5-ABPDC(5)@DUT-5@DUT-5-BPyDC(25) 6:5:1 and DUT-5-ABPDC(15)@DUT-5@DUT-5-BPyDC(25) 2:1:1. After each layer the material was characterized regarding its crystallinity, porosity and the real linker amount was determined.

DUT-5-ABPDC(5)@DUT-5@DUT-5-BPyDC(25) 6:5:1 was synthesized as follows: 4,4'-biphenyldicarboxylic acid (0.5677 g, 2.3438 mmol, 3 eq), 2,2'-bipyridine-5,5'-dicarboxylic acid (0.1908 g, 0.7813 mmol, 1 eq) and aluminum chloride hexahydrate ($\text{AlCl}_3 \cdot 6\text{H}_2\text{O}$, 0.7545 g, 3.125 mmol, 4 eq) were mixed with 50 ml of DMF and stirred in a sealed glass vessel at 120 °C in an oil bath for 24 hours. After the synthesis, the material was filtered hot in a hot state and washed with 3 x 20 ml of hot (100 °C) DMF and dried at 130 °C for three days. The first shell was synthesized using the core (0.2846 g, 1 mmol, 1 eq), 4,4'-biphenyldicarboxylic acid (1.2112 g, 5 mmol, 5 eq) and aluminum chloride hexahydrate ($\text{AlCl}_3 \cdot 6\text{H}_2\text{O}$, 1.2072 g, 5 mmol, 5 eq). The core was suspended in 20 ml of hot DMF, the linker was dissolved in 120 ml of hot DMF and the salt in 20 ml of DMF. Afterwards, all three mixtures were combined in a sealed glass vessel and reacted for 24 hours at 120 °C in an oil bath. After the synthesis, the material was filtered off in a hot state and washed with 3 x 20 ml of hot (100 °C) DMF and dried at 130 °C for three days. In the last step, the outer shell was synthesized. The core-shell material (0.8000 g, 2.8121 mmol, 1 eq) was suspended in 20 ml of DMF. 4,4'-biphenyldicarboxylic acid (0.6471 g, 2.6715 mmol, 0.95 eq) and 2-amino-4,4'-biphenyldicarboxylic acid (0.0362 g, 0.1406 mmol, 0.05 eq) were dissolved in 120 ml of DMF. Aluminum chloride hexahydrate ($\text{AlCl}_3 \cdot 6\text{H}_2\text{O}$, 0.6789 g, 2.8121 mmol, 1 eq) was dissolved in 20 ml DMF. All three mixtures were then added to a closed reaction glass vessel and reacted

for 24 hours at 120 °C in an oil bath. After the synthesis, the material was filtered off in a hot state and washed with 3 x 20 ml of hot (100 °C) DMF and dried at 130 °C for three days.

DUT-5-ABPDC(15)@DUT-5@DUT-5-BPyDC(25) 2:1:1 was synthesized as follows: 4,4'-biphenyldicarboxylic acid (0.5677 g, 2.3438 mmol, 3 eq), 2,2'-bipyridine-5,5'-dicarboxylic acid (0.1908 g, 0.7813 mmol, 1 eq) and aluminum chloride hexahydrate ($\text{AlCl}_3 \cdot 6\text{H}_2\text{O}$, 0.7545 g, 3.125 mmol, 4 eq) were mixed with 50 ml of DMF and stirred in a sealed glass vessel at 120 °C in an oil bath for 24 hours. After the synthesis, the material was filtered off in a hot state and washed with 3 x 20 ml of hot (100 °C) DMF and dried at 130 °C for three days. The first shell was synthesized using the core (0.2879 g, 1 mmol, 1 eq), 4,4'-biphenyldicarboxylic acid (1.2112 g, 5 mmol, 5 eq) and aluminum chloride hexahydrate ($\text{AlCl}_3 \cdot 6\text{H}_2\text{O}$, 1.2072 g, 5 mmol, 5 eq). The core was suspended in 20 ml of hot DMF, the linker was dissolved in 120 ml of hot DMF and the salt in 20 ml of DMF. Afterwards, all three mixtures were combined in a sealed glass vessel and reacted for 24 hours at 120 °C in an oil bath. After the synthesis, the material was filtered off in a hot state and washed with 3 x 20 ml of hot (100 °C) DMF and dried at 130 °C for three days. In the last step, the outer shell was synthesized. Core-shell material (0.5000 g, 1.7576 mmol, 1 eq) was suspended in 20 ml of DMF. 4,4'-biphenyldicarboxylic acid (0.3619 g, 1.4940 mmol, 0.85 eq) and 2-amino-4,4'-biphenyldicarboxylic acid (0.0679 g, 0.2636 mmol, 0.15 eq) were dissolved in 120 ml of DMF. Aluminum chloride hexahydrate ($\text{AlCl}_3 \cdot 6\text{H}_2\text{O}$, 0.4243 g, 1.7576 mmol, 1 eq) was dissolved in 20 ml DMF. All three mixtures were then added to a closed reaction glass vessel and reacted for 24 hours at 120 °C in an oil bath. After the synthesis, the material was filtered off in a hot state and washed with 3 x 20 ml of hot (100 °C) DMF and dried at 130 °C for three days.

5.2.7 Post-synthetic modification reaction

After their characterization, the resulting DUT-5-based materials (whether statistically distributed or core-shell) were used for post-synthetic modification reactions. In the first step, the BPyDC linkers were modified with cobalt. MOF precursor was suspended in DMF (0.5000 g MOF material in 45 ml of DMF). Cobalt(II) nitrate hexahydrate (2 eq with regard to the BPyDC linker) was dissolved in DMF (0.0342 g metal salt in 15 ml DMF) and both mixtures were then put together and shaken in a sealed glass vessel at 60 °C for 6 hours. The resulting material was then filtered off, washed with 3 x 20 ml of DMF, dried overnight at room temperature and then in oven at 130 °C for 3 hours. In the second step of PSM, the ABPDC linkers were modified with salicylaldehyde. The MOF precursor was activated for 4 hours

under vacuum and then suspended under inert atmosphere in toluene (0.3500 g material in 30 ml DMF). Salicylaldehyde (8 eq with regard to the ABPDC linker) was dissolved in toluene (15 ml for 0.199 g salicylaldehyde) and the pH was adjusted with acetic acid to pH = 4-5. Both mixtures were put together in a sealed glass vessel and shaken at 60 °C for 3 days. The mixture was afterwards filtered off and the solid product was washed with 3 x 20 ml of toluene, dried overnight at room temperature and afterwards for 3 hours at 130 °C. The previously incorporated salicylaldehyde groups were in the last step used for the chelation of iron species. The MOF material was suspended in DMF (0.2000 g material in 15 ml). Iron(II) chloride tetrahydrate (1 eq based on the percentage of salicylaldehyde modification) was also dissolved in DMF and both mixtures were mixed in a sealed glass vessel and shaken for 6 hours at 60 °C. After the synthesis, the resulting material was filtered off, washed with 3 x 20 ml of DMF, dried overnight and then at 130 °C for 3 hours. After each PSM step the powders were thoroughly characterized.

5.3 Analytical methods

5.3.1 Attenuated total reflection infrared spectroscopy (ATR-IR)

ATR-IR spectra were collected on an IR spectrometer from Thermo Fisher Scientific with a diamond crystal in the range between 4000 cm^{-1} and 400 cm^{-1} . Before the measurements the background was collected and subtracted. One spectrum consisted of 16 scans.

5.3.2 Gas chromatography coupled with mass spectrometry

The probes obtained during the oxidation reactions were analyzed on a HP Agilent 6890 gas chromatograph, which was combined with a mass spectrometer. The specific parameters can be seen in **Table 15**.

Table 15. GC-MS specifications.

Parameter	Specification
Column	CP-Sil PONA CB (Agilent)
	Length: 100 m
	Film thickness: 0.5 μm
	Column diameter: 0.25 mm
Stationary phase	5 % Biphenyl, 95 % Polydimethylsiloxane
Injection volume	1 μl
Column pressure	2.6 bar
Split ratio	20:1
Split flow	28.2 ml/min
Carrier gas	Helium
Carrier gas flow	1.4 ml/min
Temperature program	Start at 80 °C, held for 1.5 min
	From 80 °C up to 250 °C with a 10 K/min rate
	10 min at 250 °C
Detector	Temperature: 270 °C
	Air flow: 450 ml/min
	Hydrogen flow: 40 ml/min
	Make-up flow (He): 45 ml/min

5.3.3 Inductively coupled plasma optical emission spectrometry (ICP-OES)

The analysis was performed on an iCAP 6000 spectrometer from Thermo Scientific. For the quantitative evaluation, a six-point calibration was used and the results were analyzed using the iTEVA9.8 software.

The materials had to be diluted prior to the analysis. For each type of material, a specific procedure was developed. 3.3 mg of CPO-27 materials were directly diluted in 5 ml HNO₃, put in a 100 ml volumetric flask which was then filled with distilled water.

3.3 mg of thermally decomposed CPO-27 materials were firstly oxidized in an oven at 600 °C and afterwards mixed with 2 ml H₂SO₄ and heated with a heat gun. This was usually repeated twice. After the dilution, the sample was put into a 100 ml volumetric flask which was then filled with water.

3.3 mg of DUT-5 materials were firstly heated in an oven up to 700 °C to burn out the organic linkers. Afterwards the powder was mixed twice with 2 ml HCl and evaporated over a heat gun in between. At the end 5 ml HNO₃ was added and the resulting mixture was put into 100 ml volumetric flask which was then filled with water.

5.3.4 Nitrogen physisorption

The samples were activated under vacuum for several hours at different temperatures prior to the measurement. Specifically, DUT-5 frameworks and thermally decomposed CPO-27 were activated for 20 hours at 130 °C under vacuum. DUT-5-based materials with incorporated metals were activated only for 3 hours at 130°C under vacuum to preserve the structure. The physisorption measurements were performed at a Microtrac Belsorp Mini x. Specific surface areas as well as pore volumes and pore diameters were determined using BET method within the BELMaster – Ver 7.3.2.0 software.

5.3.5 Nuclear magnetic resonance spectroscopy (NMR)

5 mg of DUT-5 based samples were diluted in 75 µl of NaOD, 425 µl of D₂O and 200 µl of DMF-d₇. Spectra were collected on a Bruker Ascend 400 MHz NMR spectrometer. Chemical shifts were referenced to DMF-d₇ and reported relative to tetramethylsilane. The assignment of signals and the determination of peak areas were done in the program MestReNova, which was later used for the determination of the linker ratios.

5.3.6 Powder X-ray Diffraction

PXRD patterns were collected on a powder diffractometer D5005 from Siemens/Brucker with Cu K α radiation in the 2θ range between 4° and 80° with a step width of $2\theta = 0.04^\circ$ and collection time of 10 s/step.

5.3.7 Thermogravimetric analysis (TGA)

The thermal stability and decomposition profile of the samples was measured on a Setys 16/18 from Seteram in synthetic air (20% oxygen in nitrogen). 20-30 mg of the material were heated from 20°C to 900 °C with a heating rate of 10 K/min if not indicated otherwise.

5.3.8 X-ray absorption spectroscopy (XAS)

XAS experiments were performed at PETRA III Extension beamline P65 (energy range: 4 – 44 keV) at DESY (Deutsches Elektronensynchrotron) in Hamburg (Germany).^[208] All samples were prepared in a form of a pellet using cellulose as a binder. The amount of sample needed for the pellets was calculated using XAFS Mas software package. For all measurements a Si(111) C-type double crystal monochromator was used and all spectra were recorded at ambient temperature and pressure in transmission mode in the range of -150 eV to 1000 eV around the edge in 180 sec. Simultaneously with the samples, corresponding metal foils were measured as a reference.

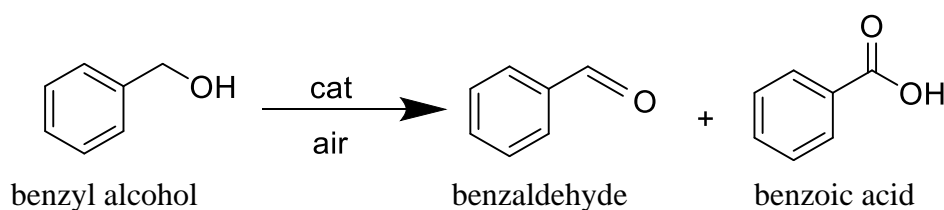
5.4 Catalytic tests

Catalytic tests were performed using three different substrates. Benzyl alcohol as a primary alcohol, 1-phenylethanol as a secondary alcohol and cinnamyl alcohol as a primary alcohol with an additional functional group. Substrate, catalyst and internal standard were combined with DMF in a three-necked flask and attached to a reflux cooler. One opening was used for a septum with a Teflon tube ($\varnothing = 0.5$ cm) through which air was provided into the liquid. The second opening was sealed and each hour a probe was taken. The flask was inserted into a pre-heated oil bath.

5.4.1 Oxidation of benzyl alcohol

CPO-27 materials and CPO-27-based materials were tested in the oxidation of benzyl alcohol using 6 mmol of benzyl alcohol, 0.4 mol% of metal in catalyst and 0.56 eq of biphenyl in 60 ml of DMF. Every hour 200 μ l of the reaction mixture were taken for GC analysis, diluted to 2 ml

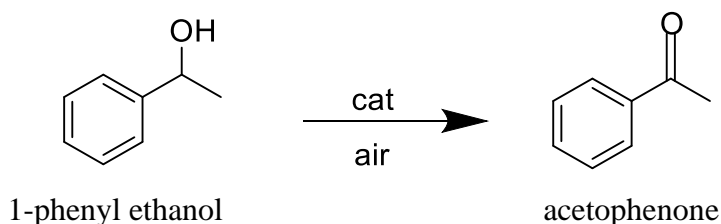
with DCM and directly analyzed. The reaction was performed at 130 °C with an air flow rate of 200 ml/min. DUT-5 based materials were tested in the oxidation of benzyl alcohol using 2 mmol of benzyl alcohol, 0.01 mol% of Co in the catalyst and 0.56 eq of biphenyl in 30 ml of DMF. The reaction was performed at 130 °C with an air flow rate of 200 ml/min. Every hour, 200 μ l of the reaction mixture was taken for GC analysis, diluted to 2 ml with DCM and directly analyzed. The main product of the reaction was benzaldehyde (**Scheme 7**) with a retention time $T_r = 15.6$ min. Besides, benzoic acid as the product of over-oxidation was observable, and also *N*-benzylidenemethylamine ($T_r = 15.5$ min) as a side product.



Scheme 7. Oxidation of benzyl alcohol.

5.4.2 Oxidation of 1-phenylethanol

CPO-27-based materials were applied in the oxidation of 1-phenylethanol. 15 mmol of 1-phenylethanol, 0.4 mol% of metal in the catalyst and 0.33 eq of biphenyl were dissolved in 30 ml of DMF. Every hour, 200 μ l of the mixture were taken for GC analysis, diluted to 2 ml with DCM and directly analyzed. The reaction was performed at 140 °C with an air flow rate of 300 ml/min. The only product was acetophenone (**Scheme 8**) with a retention time of 17.5 min.

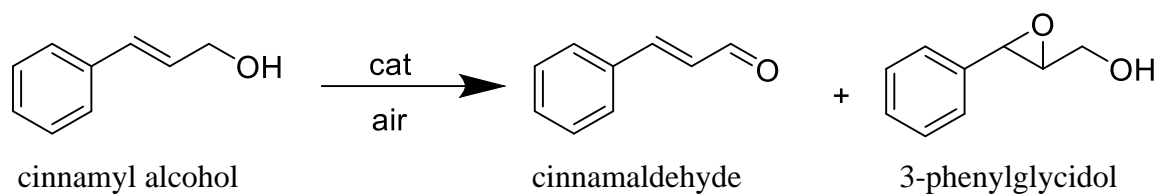


Scheme 8. Oxidation of the secondary alcohol 1-phenylethanol.

5.4.3 Oxidation of cinnamyl alcohol

DUT-5-based materials were tested in the oxidation of cinnamyl alcohol using 2 mmol of cinnamyl alcohol, 0.01 mol% of Co in the catalyst, 0.56 eq of biphenyl and 30 ml of DMF. Every hour, 100 μ l of the mixture were taken for GC analysis, diluted to 2 ml with DCM and

directly analyzed. The reaction was performed at 130 °C, with an air flow rate of 200 ml/min. The two main products (**Scheme 9**) were cinnamaldehyde ($T_r = 21.0$ min) and 3-phenylglycidol ($T_r = 22.4$ min). During the reaction also other side products were observable, such as hydrocinnamylalcohol ($T_r = 20.7$ min), benzaldehyde ($T_r = 15.6$ min), 2-phenylpropanal ($T_r = 19.0$ min) and phenylacetaldehyde ($T_r = 17.0$ min).



Scheme 9. Oxidation of cinnamyl alcohol.

6 Abbreviations and symbols

Abbreviation	Meaning
AAS	Atomic absorption spectroscopy
ABPDC	2-Aminobenzene-1,4-dicarboxylate
ATR-IR	Attenuated total reflection infrared spectroscopy
BDC	Benzene-1,4-dicarboxylate
BET	Brunauer-Emmett-Teller
BiOBr	Bismuth oxybromide
b.p.	Boiling point
BPDC	4,4'-Biphenyldicarboxylate
BPyDC	2,2'-Bipyridine-5,5'-dicarboxylate
BTC	Benzene-1,3,5-tricarboxylate
cat	Catalyst
Co <i>ccp</i>	Cobalt cubic closed packed crystal structure
CPO	Coordination polymer of Oslo
D ₂ O	Deuterium oxide
DCM	Dichloromethane
DESY	Deutsches Elektronensynchrotron

Abbreviations and symbols

DFT/GIPAW	Density functional theory/ Gauge Including Projector Augmented Waves
DMF	<i>N,N</i> -Dimethylformamide
DMF-d ₇	<i>N,N</i> -Dimethylformamide-d ₇ (deuterated)
DTG	First derivative of the thermogravimetric analysis curve
DUT	Dresden University of Technology
DMOF	1,4-Diazabicyclo[2.2.2]octane metal-organic framework
EDX	Energy dispersive X-ray spectroscopy
EXAFS	Extended X-ray absorption fine structure
Fe <i>bcc</i>	Iron body-centered cubic crystal structure
FMF	<i>N</i> -Formyl- <i>N</i> -methylformamide
FT-IR	Fourier-transform infrared spectroscopy
GC-MS	Gas chromatography coupled with mass spectroscopy
HKUST	Hong Kong University of Science and Technology
I-bdc	2-Iodobenzene-1,4-dicarboxylate
ICP-OES	Inductively coupled plasma optical emission spectrometry
IR	Infrared spectroscopy

Abbreviations and symbols

IRMOF	Isorecticular metal-organic framework
LG-HETCOR	Lee-Goldburg heteronuclear correlation spectroscopy
<i>lp</i>	Large pore
Mal	Maleic anhydride
MIL	Matériaux de l'Institut Lavoisier
MIX-MOF	Mixed metal-organic framework
MOF	Metal-organic framework
MS	Mass spectroscopy
NaOD	Sodium deuterioxide
NMP	<i>N</i> -methyl-2-pyrrolidone
NMR	Nuclear magnetic resonance
<i>np</i>	Narrow pore
PCP	Porous coordination polymer
PSLE	Post-synthetic linker exchange
PSM	Post-synthetic modification
PSME	Post-synthetic metal exchange
PXRD	Powder X-ray diffraction
PyDC	Pyridine-3,5-dicarboxylate
RBS	Rutherford backscattering spectrometry

Abbreviations and symbols

Sal	Salicylaldehyde
SEM/EDX	Scanning electron microscopy coupled with energy-dispersive X-ray spectroscopy
S_{BET}	Specific surface area according to Brunauer-Emmett-Teller
SBU	Secondary building unit
S_{Langmuir}	Langmuir surface area
TEM/EDX	Transmission electron microscopy coupled with energy-dispersive X-ray spectroscopy
TG	Thermogravimetry
TGA	Thermogravimetric analysis
TGA-MS	Thermogravimetric analysis coupled with mass spectroscopy
$\text{Ti}(\text{O}^i\text{Pr})_4$	Titanium isopropoxide
TON	Turn over number
T_r	Retention time
UiO	University of Oslo
UMCM	University of Michigan Crystalline Material
UV-VIS	Ultraviolet–visible spectroscopy
XAS	X-ray absorption spectroscopy
Z	Atomic number

Abbreviations and symbols

ZIF	Zeolitic imidazolate framework
ZnEt ₂	Diethylzinc
∅	Diameter
θ	Angle

7 References

- [1] C. Janiak, *Angew. Chem. Int. Ed. Engl.* **1997**, *36*, 1431–1434.
- [2] J. Gascon, A. Corma, F. Kapteijn, F. X. Llabrés I Xamena, *ACS Catal.* **2014**, *4*, 361–378.
- [3] O. K. Farha, I. Eryazici, N. C. Jeong, B. G. Hauser, C. E. Wilmer, A. A. Sarjeant, R. Q. Snurr, S. T. Nguyen, A. Ö. Yazaydin, J. T. Hupp, *J. Am. Chem. Soc.* **2012**, *134*, 15016–15021.
- [4] G. Férey, C. Serre, *Chem. Soc. Rev.* **2009**, *38*, 1380.
- [5] F. Millange, C. Serre, N. Guillou, G. Férey, R. I. Walton, *Angew. Chem. Int. Ed.* **2008**, *47*, 4100–4105.
- [6] W. P. Mounfield, K. S. Walton, *J. Colloid Interface Sci.* **2015**, *447*, 33–39.
- [7] G. Férey, *Chem Soc Rev* **2008**, *37*, 191–214.
- [8] D. Riou, G. Férey, *J. Mater. Chem.* **1998**, *8*, 2733–2735.
- [9] F. Serpaggi, G. Férey, *J. Mater. Chem.* **1998**, *8*, 2737–2741.
- [10] C. Livage, C. Egger, M. Nogues, G. Férey, *J. Mater. Chem.* **1998**, *8*, 2743–2747.
- [11] F. Serpaggi, G. Férey, *J. Mater. Chem.* **1998**, *8*, 2749–2755.
- [12] M. Kondo, T. Yoshitomi, H. Matsuzaka, S. Kitagawa, K. Seki, *Angew. Chem. Int. Ed. Engl.* **1997**, *36*, 1725–1727.
- [13] S. Kitagawa, R. Kitaura, S. Noro, *Angew. Chem. Int. Ed.* **2004**, *43*, 2334–2375.
- [14] A. Bavykina, N. Kolobov, I. S. Khan, J. A. Bau, A. Ramirez, J. Gascon, *Chem. Rev.* **2020**, *120*, 8468–8535.
- [15] O. M. Yaghi, D. A. Richardson, G. Li, C. E. Davis, T. L. Groy, *MRS Proc.* **1994**, *371*, 15.
- [16] O. M. Yaghi, G. Li, H. Li, *Nature* **1995**, *378*, 703–706.
- [17] O. M. Yaghi, H. Li, M. O’Keeffe, *MRS Proc.* **1996**, *453*, 127.
- [18] H. Li, M. Eddaoudi, M. O’Keeffe, O. M. Yaghi, *Nature* **1999**, *402*, 276–279.
- [19] C. W. Jones, *JACS Au* **2022**, *2*, 1504–1505.
- [20] J. Ren, N. M. Musyoka, H. W. Langmi, B. C. North, M. Mathe, X. Kang, *Int. J. Hydrog. Energy* **2014**, *39*, 14912–14917.
- [21] A. K. Adhikari, K.-S. Lin, M.-T. Tu, *J. Taiwan Inst. Chem. Eng.* **2016**, *63*, 463–472.
- [22] P. D. C. Dietzel, B. Panella, M. Hirscher, R. Blom, H. Fjellvåg, *Chem. Commun.* **2006**, 959.
- [23] S. Bourrelly, P. L. Llewellyn, C. Serre, F. Millange, T. Loiseau, G. Férey, *J. Am. Chem. Soc.* **2005**, *127*, 13519–13521.
- [24] T. Kundu, B. B. Shah, L. Bolinois, D. Zhao, *Chem. Mater.* **2019**, *31*, 2842–2847.
- [25] Y. Lin, C. Kong, Q. Zhang, L. Chen, *Adv. Energy Mater.* **2017**, *7*, 1601296.
- [26] B. Pato-Doldán, M. H. Rosnes, P. D. C. Dietzel, *ChemSusChem* **2017**, *10*, 1710–1719.
- [27] M. Mendt, B. Jee, D. Himsl, L. Moschkowitz, T. Ahnfeldt, N. Stock, M. Hartmann, A. Pöpl, *Appl. Magn. Reson.* **2014**, *45*, 269–285.
- [28] P. Horcajada, C. Serre, G. Maurin, N. A. Ramsahye, F. Balas, M. Vallet-Regí, M. Sebban, F. Taulelle, G. Férey, *J. Am. Chem. Soc.* **2008**, *130*, 6774–6780.
- [29] W. Cai, C.-C. Chu, G. Liu, Y.-X. J. Wang, *Small* **2015**, *11*, 4806–4822.
- [30] X. Gao, M. Zhai, W. Guan, J. Liu, Z. Liu, A. Damirin, *ACS Appl. Mater. Interfaces* **2017**, *9*, 3455–3462.
- [31] Y.-B. Huang, J. Liang, X.-S. Wang, R. Cao, *Chem. Soc. Rev.* **2017**, *46*, 126–157.
- [32] A. Corma, H. García, F. X. Llabrés I Xamena, *Chem. Rev.* **2010**, *110*, 4606–4655.
- [33] A. Dhakshinamoorthy, Z. Li, H. Garcia, *Chem. Soc. Rev.* **2018**, *47*, 8134–8172.
- [34] D. Farrusseng, S. Aguado, C. Pinel, *Angew. Chem. Int. Ed.* **2009**, *48*, 7502–7513.
- [35] I. Cota, F. Fernandez Martinez, *Coord. Chem. Rev.* **2017**, *351*, 189–204.

- [36] A. Schaate, P. Roy, A. Godt, J. Lippke, F. Waltz, M. Wiebcke, P. Behrens, *Chem. – Eur. J.* **2011**, *17*, 6643–6651.
- [37] T. A. Mulyati, R. Ediati, A. Rosyidah, *Indones. J. Chem.* **2015**, *15*, 101–107.
- [38] Y.-X. Sun, W.-Y. Sun, *Chin. Chem. Lett.* **2014**, *25*, 823–828.
- [39] W. Shen, X. Guo, H. Pang, *Molecules* **2022**, *27*, 8226.
- [40] A. Buragohain, S. Couck, P. Van Der Voort, J. F. M. Denayer, S. Biswas, *J. Solid State Chem.* **2016**, *238*, 195–202.
- [41] A. Laybourn, J. Katrib, R. S. Ferrari-John, C. G. Morris, S. Yang, O. Udoudo, T. L. Easun, C. Dodds, N. R. Champness, S. W. Kingman, M. Schröder, *J. Mater. Chem. A* **2017**, *5*, 7333–7338.
- [42] J. Ge, L. Liu, L. Qiu, X. Jiang, Y. Shen, *J. Porous Mater.* **2016**, *23*, 857–865.
- [43] E. Haque, N. A. Khan, J. H. Park, S. H. Jhung, *Chem. - Eur. J.* **2010**, *16*, 1046–1052.
- [44] M. Homae, H. Hamadi, V. Nobakht, M. Javaherian, B. Salahshournia, *Polyhedron* **2019**, *165*, 152–161.
- [45] W.-J. Son, J. Kim, J. Kim, W.-S. Ahn, *Chem. Commun.* **2008**, 6336.
- [46] R. Sanz, F. Martínez, G. Orcajo, L. Wojtas, D. Briones, *Dalton Trans* **2013**, *42*, 2392–2398.
- [47] W. Kleist, M. Maciejewski, A. Baiker, *Thermochim. Acta* **2010**, *499*, 71–78.
- [48] P. A. Julien, K. Užarević, A. D. Katsenis, S. A. J. Kimber, T. Wang, O. K. Farha, Y. Zhang, J. Casaban, L. S. Germann, M. Etter, R. E. Dinnebier, S. L. James, I. Halasz, T. Friščić, *J. Am. Chem. Soc.* **2016**, *138*, 2929–2932.
- [49] J. Beamish-Cook, K. Shankland, C. A. Murray, P. Vaqueiro, *Cryst. Growth Des.* **2021**, *21*, 3047–3055.
- [50] K. Watts, A. Baker, T. Wirth, *J. Flow Chem.* **2015**, *4*, 2–11.
- [51] O. J. De Lima Neto, A. C. D. O. Frós, B. S. Barros, A. F. De Farias Monteiro, J. Kulesza, *New J. Chem.* **2019**, *43*, 5518–5524.
- [52] W. W. Lestari, I. D. Winarni, F. Rahmawati, *IOP Conf. Ser. Mater. Sci. Eng.* **2017**, *172*, 012064.
- [53] U. Mueller, M. Schubert, F. Teich, H. Puetter, K. Schierle-Arndt, J. Pastré, *J Mater Chem* **2006**, *16*, 626–636.
- [54] A. Martinez Joaristi, J. Juan-Alcañiz, P. Serra-Crespo, F. Kapteijn, J. Gascon, *Cryst. Growth Des.* **2012**, *12*, 3489–3498.
- [55] R. Ameloot, L. Stappers, J. Fransaer, L. Alaerts, B. F. Sels, D. E. De Vos, *Chem. Mater.* **2009**, *21*, 2580–2582.
- [56] T. R. C. Van Assche, G. Desmet, R. Ameloot, D. E. De Vos, H. Terryn, J. F. M. Denayer, *Microporous Mesoporous Mater.* **2012**, *158*, 209–213.
- [57] F. J. Claire, M. A. Solomos, J. Kim, G. Wang, M. A. Siegler, M. F. Crommie, T. J. Kempa, *Nat. Commun.* **2020**, *11*, 5524.
- [58] C. Young, J. Wang, J. Kim, Y. Sugahara, J. Henzie, Y. Yamauchi, *Chem. Mater.* **2018**, *30*, 3379–3386.
- [59] T. Stassin, I. Stassen, J. Marreiros, A. J. Cruz, R. Verbeke, M. Tu, H. Reinsch, M. Dickmann, W. Egger, I. F. J. Vankelecom, D. E. De Vos, R. Ameloot, *Chem. Mater.* **2020**, *32*, 1784–1793.
- [60] S. Han, C. B. Mullins, *ChemSusChem* **2020**, *13*, 5433–5442.
- [61] P. M. Barron, C. A. Wray, C. Hu, Z. Guo, W. Choe, *Inorg. Chem.* **2010**, *49*, 10217–10219.
- [62] R. K. Tonnah, M. Chai, M. Abdollahzadeh, H. Xiao, M. Mohammad, E. Hosseini, M. Zakertabrizi, D. Jarrahbashi, A. Asadi, A. Razmjou, M. Asadnia, *ACS Nano* **2023**, *17*, 12445–12457.
- [63] S. Yuan, L. Zou, H. Li, Y. Chen, J. Qin, Q. Zhang, W. Lu, M. B. Hall, H. Zhou, *Angew. Chem. Int. Ed.* **2016**, *55*, 10776–10780.
- [64] M. Ding, G. Chen, W. Xu, C. Jia, H. Luo, *Nano Mater. Sci.* **2020**, *2*, 264–280.

- [65] J. Bitzer, W. Kleist, *Chem. – Eur. J.* **2019**, *25*, 1866–1882.
- [66] M. Eddaoudi, J. Kim, N. Rosi, D. Vodak, J. Wachter, M. O’Keeffe, O. M. Yaghi, *Science* **2002**, *295*, 469–472.
- [67] A. Dhakshinamoorthy, A. M. Asiri, H. Garcia, *Catal. Sci. Technol.* **2016**, *6*, 5238–5261.
- [68] X.-L. Zhao, W.-Y. Sun, *CrystEngComm* **2014**, *16*, 3247.
- [69] Z. Yin, Y.-L. Zhou, M.-H. Zeng, M. Kurmoo, *Dalton Trans.* **2015**, *44*, 5258–5275.
- [70] L. Feng, K.-Y. Wang, G. S. Day, H.-C. Zhou, *Chem. Soc. Rev.* **2019**, *48*, 4823–4853.
- [71] J. Hui, H. Chu, W. Zhang, Y. Shen, W. Chen, Y. Hu, W. Liu, C. Gao, S. Guo, G. Xiao, S. Li, Y. Fu, D. Fan, W. Zhang, F. Huo, *Nanoscale* **2018**, *10*, 8772–8778.
- [72] L. Feng, S. Yuan, L.-L. Zhang, K. Tan, J.-L. Li, A. Kirchon, L.-M. Liu, P. Zhang, Y. Han, Y. J. Chabal, H.-C. Zhou, *J. Am. Chem. Soc.* **2018**, *140*, 2363–2372.
- [73] S. Abednatanzi, P. Gohari Derakhshandeh, H. Depauw, F.-X. Coudert, H. Vrielinck, P. Van Der Voort, K. Leus, *Chem. Soc. Rev.* **2019**, *48*, 2535–2565.
- [74] W. Kleist, F. Jutz, M. Maciejewski, A. Baiker, *Eur. J. Inorg. Chem.* **2009**, *2009*, 3552–3561.
- [75] S. N. Jaluddin, K. Kassim, W. N. W. Ibrahim, *Procedia Chem.* **2015**, *16*, 8–14.
- [76] J. F. Blandez, A. Santiago-Portillo, S. Navalón, M. Giménez-Marqués, M. Álvaro, P. Horcajada, H. García, *J. Mol. Catal. Chem.* **2016**, *425*, 332–339.
- [77] X. Gu, C. Huang, Z. Xu, H. Wu, R. Dong, R. Liu, J. Chen, H. Zhu, *J. Solid State Chem.* **2021**, *294*, 121803.
- [78] J. G. Flores, J. Aguilar-Pliego, N. Martin-Guaregua, I. A. Ibarra, M. Sanchez-Sanchez, *Catal. Today* **2022**, *394–396*, 295–303.
- [79] S. Marx, W. Kleist, J. Huang, M. Maciejewski, A. Baiker, *Dalton Trans.* **2010**, *39*, 3795.
- [80] D. H. Hong, M. P. Suh, *Chem. - Eur. J.* **2014**, *20*, 426–434.
- [81] A. Naeem, V. P. Ting, U. Hintermair, M. Tian, R. Telford, S. Halim, H. Nowell, M. Holyńska, S. J. Teat, I. J. Scowen, S. Nayak, *Chem. Commun.* **2016**, *52*, 7826–7829.
- [82] J. Bitzer, W. Kleist, *Chem. – Eur. J.* **2019**, *25*, 1866–1882.
- [83] S. Marx, W. Kleist, A. Baiker, *J. Catal.* **2011**, *281*, 76–87.
- [84] J. Yang, X. Yan, T. Xue, Y. Liu, *RSC Adv.* **2016**, *6*, 55266–55271.
- [85] C. Guo, J. Guo, Y. Zhang, D. Wang, L. Zhang, Y. Guo, W. Ma, J. Wang, *CrystEngComm* **2018**, *20*, 7659–7665.
- [86] T. Li, J. E. Sullivan, N. L. Rosi, *J. Am. Chem. Soc.* **2013**, *135*, 9984–9987.
- [87] H. H.-M. Yeung, W. Li, P. J. Saines, T. K. J. Köster, C. P. Grey, A. K. Cheetham, *Angew. Chem. Int. Ed.* **2013**, *52*, 5544–5547.
- [88] M. Taddei, D. Tiana, N. Casati, J. A. Van Bokhoven, B. Smit, M. Ranocchiari, *Phys. Chem. Chem. Phys.* **2017**, *19*, 1551–1559.
- [89] C. H. Hendon, J. Bonnefoy, E. A. Quadrelli, J. Canivet, M. B. Chambers, G. Rousse, A. Walsh, M. Fontecave, C. Mellot-Draznieks, *Chem. - Eur. J.* **2016**, *22*, 3713–3718.
- [90] X. Kong, H. Deng, F. Yan, J. Kim, J. A. Swisher, B. Smit, O. M. Yaghi, J. A. Reimer, *Science* **2013**, *341*, 882–885.
- [91] A. Krajnc, T. Kos, N. Zabukovec Logar, G. Mali, *Angew. Chem. Int. Ed.* **2015**, *54*, 10535–10538.
- [92] T.-H. Park, K. Koh, A. G. Wong-Foy, A. J. Matzger, *Cryst. Growth Des.* **2011**, *11*, 2059–2063.
- [93] Y. K. Hwang, D.-Y. Hong, J.-S. Chang, S. H. Jhung, Y.-K. Seo, J. Kim, A. Vimont, M. Daturi, C. Serre, G. Férey, *Angew. Chem. Int. Ed.* **2008**, *47*, 4144–4148.
- [94] S. Nießing, C. Janiak, *Mol. Catal.* **2019**, *467*, 70–77.
- [95] L. J. Wang, H. Deng, H. Furukawa, F. Gándara, K. E. Cordova, D. Peri, O. M. Yaghi, *Inorg. Chem.* **2014**, *53*, 5881–5883.

- [96] H. Depauw, I. Nevjestić, J. De Winne, G. Wang, K. Haustraete, K. Leus, A. Verberckmoes, C. Detavernier, F. Callens, E. De Canck, H. Vrielinck, P. Van Der Voort, *Chem. Commun.* **2017**, *53*, 8478–8481.
- [97] D. Sun, F. Sun, X. Deng, Z. Li, *Inorg. Chem.* **2015**, *54*, 8639–8643.
- [98] D. Denysenko, T. Werner, M. Grzywa, A. Puls, V. Hagen, G. Eickerling, J. Jelic, K. Reuter, D. Volkmer, *Chem Commun* **2012**, *48*, 1236–1238.
- [99] F. Nouar, T. Devic, H. Chevreau, N. Guillou, E. Gibson, G. Clet, M. Daturi, A. Vimont, J. M. Grenèche, M. I. Breeze, R. I. Walton, P. L. Llewellyn, C. Serre, *Chem. Commun.* **2012**, *48*, 10237.
- [100] S. M. Cohen, *Chem. Rev.* **2012**, *112*, 970–1000.
- [101] K. K. Tanabe, S. M. Cohen, *Chem Soc Rev* **2011**, *40*, 498–519.
- [102] Z. Wang, S. M. Cohen, *J. Am. Chem. Soc.* **2007**, *129*, 12368–12369.
- [103] Z. Saedi, V. Safarifard, A. Morsali, *Microporous Mesoporous Mater.* **2016**, *229*, 51–58.
- [104] A. D. Burrows, C. G. Frost, M. F. Mahon, C. Richardson, *Angew. Chem. Int. Ed.* **2008**, *47*, 8482–8486.
- [105] M. Meilikhov, K. Yussenko, R. A. Fischer, *J. Am. Chem. Soc.* **2009**, *131*, 9644–9645.
- [106] S. Mandal, S. Natarajan, P. Mani, A. Pankajakshan, *Adv. Funct. Mater.* **2021**, *31*, 2006291.
- [107] O. K. Farha, K. L. Mulfort, J. T. Hupp, *Inorg. Chem.* **2008**, *47*, 10223–10225.
- [108] S. S.-Y. Chui, S. M.-F. Lo, J. P. H. Charmant, A. G. Orpen, I. D. Williams, *Science* **1999**, *283*, 1148–1150.
- [109] F. Eshraghi, M. Anbia, S. Salehi, *J. Environ. Chem. Eng.* **2017**, *5*, 4516–4523.
- [110] F. X. L. i Xamena, J. Gascon (Profesor), *Metal Organic Frameworks as Heterogeneous Catalysts*, Royal Society Of Chemistry, **2013**.
- [111] D. J. Lun, G. I. N. Waterhouse, S. G. Telfer, *J. Am. Chem. Soc.* **2011**, *133*, 5806–5809.
- [112] R. K. Deshpande, J. L. Minnaar, S. G. Telfer, *Angew. Chem. Int. Ed.* **2010**, *49*, 4598–4602.
- [113] T. Yamada, H. Kitagawa, *J. Am. Chem. Soc.* **2009**, *131*, 6312–6313.
- [114] S. Das, H. Kim, K. Kim, *J. Am. Chem. Soc.* **2009**, *131*, 3814–3815.
- [115] N. Wu, H. Guo, M. Wang, Y. Cao, L. Sun, F. Yang, T. Zhang, L. Peng, Y. Liu, W. Yang, *Anal. Chim. Acta* **2022**, *1190*, 339247.
- [116] T. K. Prasad, D. H. Hong, M. P. Suh, *Chem. - Eur. J.* **2010**, *16*, 14043–14050.
- [117] B. Garai, V. Bon, S. Krause, F. Schwotzer, M. Gerlach, I. Senkovska, S. Kaskel, *Chem. Mater.* **2020**, *32*, 889–896.
- [118] U. Fluch, B. D. McCarthy, S. Ott, *Dalton Trans.* **2019**, *48*, 45–49.
- [119] U. Fluch, V. Paneta, D. Primetzhofner, S. Ott, *Chem. Commun.* **2017**, *53*, 6516–6519.
- [120] S. J. D. Smith, K. Konstas, C. H. Lau, Y. M. Gozukara, C. D. Easton, R. J. Mulder, B. P. Ladewig, M. R. Hill, *Cryst. Growth Des.* **2017**, *17*, 4384–4392.
- [121] B. J. Burnett, P. M. Barron, C. Hu, W. Choe, *J. Am. Chem. Soc.* **2011**, *133*, 9984–9987.
- [122] P. Valvekens, E. D. Bloch, J. R. Long, R. Ameloot, D. E. De Vos, *Catal. Today* **2015**, *246*, 55–59.
- [123] T. Toyao, K. Miyahara, M. Fujiwaki, T.-H. Kim, S. Dohshi, Y. Horiuchi, M. Matsuoka, *J. Phys. Chem. C* **2015**, *119*, 8131–8137.
- [124] E. D. Bloch, D. Britt, C. Lee, C. J. Doonan, F. J. Uribe-Romo, H. Furukawa, J. R. Long, O. M. Yaghi, *J. Am. Chem. Soc.* **2010**, *132*, 14382–14384.
- [125] X.-P. Zhou, Z. Xu, M. Zeller, A. D. Hunter, *Chem. Commun.* **2009**, 5439.
- [126] W. Morris, B. Voloskiy, S. Demir, F. Gándara, P. L. McGrier, H. Furukawa, D. Cascio, J. F. Stoddart, O. M. Yaghi, *Inorg. Chem.* **2012**, *51*, 6443–6445.
- [127] K. Oisaki, Q. Li, H. Furukawa, A. U. Czaja, O. M. Yaghi, *J. Am. Chem. Soc.* **2010**, *132*, 9262–9264.
- [128] C.-D. Wu, A. Hu, L. Zhang, W. Lin, *J. Am. Chem. Soc.* **2005**, *127*, 8940–8941.

- [129] R. Van Zeeland, X. Li, W. Huang, L. M. Stanley, *RSC Adv.* **2016**, *6*, 56330–56334.
- [130] N. Wang, J. Xie, J. Zhang, *Arab. J. Chem.* **2022**, *15*, 103962.
- [131] D. Sun, Y. Gao, J. Fu, X. Zeng, Z. Chen, Z. Li, *Chem. Commun.* **2015**, *51*, 2645–2648.
- [132] F. Carson, S. Agrawal, M. Gustafsson, A. Bartoszewicz, F. Moraga, X. Zou, B. Martín-Matute, *Chem. - Eur. J.* **2012**, *18*, 15337–15344.
- [133] H. Hintz, S. Wuttke, *Chem. Mater.* **2014**, *26*, 6722–6728.
- [134] J. Espín, L. Garzón-Tovar, G. Boix, I. Imaz, D. MasPOCH, *Chem. Commun.* **2018**, *54*, 4184–4187.
- [135] M. A. Gotthardt, R. Schoch, T. S. Brunner, M. Bauer, W. Kleist, *ChemPlusChem* **2015**, *80*, 188–195.
- [136] J. Bitzer, S.-L. Heck, W. Kleist, *Microporous Mesoporous Mater.* **2020**, *308*, 110329.
- [137] S. J. Garibay, Z. Wang, K. K. Tanabe, S. M. Cohen, *Inorg. Chem.* **2009**, *48*, 7341–7349.
- [138] A. A. Alqadami, M. A. Khan, M. R. Siddiqui, Z. A. Allothman, *Microporous Mesoporous Mater.* **2018**, *261*, 198–206.
- [139] Z. Wang, K. K. Tanabe, S. M. Cohen, *Inorg. Chem.* **2009**, *48*, 296–306.
- [140] S. Chen, Z. Song, J. Lyu, Y. Guo, B. E. G. Lucier, W. Luo, M. S. Workentin, X. Sun, Y. Huang, *J. Am. Chem. Soc.* **2020**, *142*, 4419–4428.
- [141] N. L. Rosi, J. Eckert, M. Eddaoudi, D. T. Vodak, J. Kim, M. O’Keeffe, O. M. Yaghi, *Science* **2003**, *300*, 1127–1129.
- [142] A. W. Stubbs, L. Braglia, E. Borfecchia, R. J. Meyer, Y. Román-Leshkov, C. Lamberti, M. Dincă, *ACS Catal.* **2018**, *8*, 596–601.
- [143] F. Millange, C. Serre, G. Férey, *Chem. Commun.* **2002**, 822–823.
- [144] C. Serre, F. Millange, C. Thouvenot, M. Noguès, G. Marsolier, D. Louër, G. Férey, *J. Am. Chem. Soc.* **2002**, *124*, 13519–13526.
- [145] T. Loiseau, C. Serre, C. Huguenard, G. Fink, F. Taulelle, M. Henry, T. Bataille, G. Férey, *Chem. Eur. J.* **2004**, *10*, 1373–1382.
- [146] P. L. Llewellyn, P. Horcajada, G. Maurin, T. Devic, N. Rosenbach, S. Bourrelly, C. Serre, D. Vincent, S. Loera-Serna, Y. Filinchuk, G. Férey, *J. Am. Chem. Soc.* **2009**, *131*, 13002–13008.
- [147] A. Boutin, D. Bousquet, A. U. Ortiz, F.-X. Coudert, A. H. Fuchs, A. Ballandras, G. Weber, I. Bezverkhyy, J.-P. Bellat, G. Ortiz, G. Chaplais, J.-L. Paillaud, C. Marichal, H. Nouali, J. Patarin, *J. Phys. Chem. C* **2013**, *117*, 8180–8188.
- [148] E. V. Anokhina, M. Vougo-Zanda, X. Wang, A. J. Jacobson, *J. Am. Chem. Soc.* **2005**, *127*, 15000–15001.
- [149] L. Chen, J. P. S. Mowat, D. Fairen-Jimenez, C. A. Morrison, S. P. Thompson, P. A. Wright, T. Düren, *J. Am. Chem. Soc.* **2013**, *135*, 15763–15773.
- [150] J. P. S. Mowat, V. R. Seymour, J. M. Griffin, S. P. Thompson, A. M. Z. Slawin, D. Fairen-Jimenez, T. Düren, S. E. Ashbrook, P. A. Wright, *Dalton Trans* **2012**, *41*, 3937–3941.
- [151] H. Leclerc, T. Devic, S. Devautour-Vinot, P. Bazin, N. Audebrand, G. Férey, M. Daturi, A. Vimont, G. Clet, *J. Phys. Chem. C* **2011**, *115*, 19828–19840.
- [152] K. Barthelet, J. Marrot, D. Riou, G. Férey, *Angew. Chem. Int. Ed.* **2002**, *41*, 281.
- [153] A. Ghoufi, K. Benhamed, L. Boukli-Hacene, G. Maurin, *ACS Cent. Sci.* **2017**, *3*, 394–398.
- [154] M. Mendt, B. Jee, N. Stock, T. Ahnfeldt, M. Hartmann, D. Himsl, A. Pöpl, *J. Phys. Chem. C* **2010**, *114*, 19443–19451.
- [155] D. Y. Osadchii, A. I. Olivos-Suarez, Á. Szécsényi, G. Li, M. A. Nasalevich, I. A. Dugulan, P. S. Crespo, E. J. M. Hensen, S. L. Veber, M. V. Fedin, G. Sankar, E. A. Pidko, J. Gascon, *ACS Catal.* **2018**, *8*, 5542–5548.
- [156] G. P. M. Bignami, Z. H. Davis, D. M. Dawson, S. A. Morris, S. E. Russell, D. McKay, R. E. Parke, D. Iuga, R. E. Morris, S. E. Ashbrook, *Chem. Sci.* **2018**, *9*, 850–859.

- [157] O. Kozachuk, M. Meilikhov, K. Yusenkov, A. Schneemann, B. Jee, A. V. Kuttatheyil, M. Bertmer, C. Sternemann, A. Pöpl, R. A. Fischer, *Eur. J. Inorg. Chem.* **2013**, 2013, 4546–4557.
- [158] M. Xie, Y. Ma, D. Lin, C. Xu, F. Xie, W. Zeng, *Nanoscale* **2020**, 12, 67–71.
- [159] S. Zhang, M. Li, J. Wang, R. Zhang, X. Ma, H. Tao, *Colloids Surf. Physicochem. Eng. Asp.* **2023**, 664, 131208.
- [160] M. I. Breeze, G. Clet, B. C. Campo, A. Vimont, M. Daturi, J.-M. Grenèche, A. J. Dent, F. Millange, R. I. Walton, *Inorg. Chem.* **2013**, 52, 8171–8182.
- [161] X. Zheng, L. Shen, F. Lin, Y. Xu, Q. Lin, L. Jiang, *Inorg. Chem.* **2022**, 61, 3774–3784.
- [162] N. L. Rosi, J. Kim, M. Eddaoudi, B. Chen, M. O’Keeffe, O. M. Yaghi, *J. Am. Chem. Soc.* **2005**, 127, 1504–1518.
- [163] M. Märcz, R. E. Johnsen, P. D. C. Dietzel, H. Fjellvåg, *Microporous Mesoporous Mater.* **2012**, 157, 62–74.
- [164] L. Garzón-Tovar, A. Carné-Sánchez, C. Carbonell, I. Imaz, D. MasPOCH, *J. Mater. Chem. A* **2015**, 3, 20819–20826.
- [165] J. G. Flores, M. Díaz-García, I. A. Ibarra, J. Aguilar-Pliego, M. Sánchez-Sánchez, *J. Solid State Chem.* **2021**, 298, 122151.
- [166] M. Díaz-García, Á. Mayoral, I. Díaz, M. Sánchez-Sánchez, *Cryst. Growth Des.* **2014**, 14, 2479–2487.
- [167] S. Bhattacharjee, J.-S. Choi, S.-T. Yang, S. B. Choi, J. Kim, W.-S. Ahn, *J. Nanosci. Nanotechnol.* **2010**, 10, 135–141.
- [168] Y. Jiao, C. R. Morelock, N. C. Burtch, W. P. Mounfield, J. T. Hungerford, K. S. Walton, *Ind. Eng. Chem. Res.* **2015**, 54, 12408–12414.
- [169] J. A. Botas, G. Calleja, M. Sánchez-Sánchez, M. G. Orcajo, *Int. J. Hydrog. Energy* **2011**, 36, 10834–10844.
- [170] C. Huang, R. Liu, W. Yang, Y. Li, J. Huang, H. Zhu, *Inorg. Chem. Front.* **2018**, 5, 1923–1932.
- [171] J. Sun, X. Zhang, A. Zhang, C. Liao, *J. Environ. Sci.* **2019**, 80, 197–207.
- [172] X. Gu, C. Huang, Z. Xu, H. Wu, R. Dong, R. Liu, J. Chen, H. Zhu, *J. Solid State Chem.* **2021**, 294, 121803.
- [173] I. Senkowska, F. Hoffmann, M. Fröba, J. Getzschmann, W. Böhlmann, S. Kaskel, *Microporous Mesoporous Mater.* **2009**, 122, 93–98.
- [174] S. Couck, Y.-Y. Liu, K. Leus, G. V. Baron, P. Van der Voort, J. F. M. Denayer, *Microporous Mesoporous Mater.* **2015**, 206, 217–225.
- [175] M. A. Gotthardt, S. Grosjean, T. S. Brunner, J. Kotzel, A. M. Gänzler, S. Wolf, S. Bräse, W. Kleist, *Dalton Trans.* **2015**, 44, 16802–16809.
- [176] C. Yildiz, K. Kutonova, S. Oßwald, A. Titze-Alonso, J. Bitzer, S. Bräse, W. Kleist, *ChemCatChem* **2020**, 12, 1134–1142.
- [177] H. Zou, Y. Zhou, Y. Xiang, Y. Deng, Y. Tan, H. Tang, Y. Xu, *Adv. Eng. Mater.* **2020**, 22, 2000267.
- [178] J. H. Cavka, S. Jakobsen, U. Olsbye, N. Guillou, C. Lamberti, S. Bordiga, K. P. Lillerud, *J. Am. Chem. Soc.* **2008**, 130, 13850–13851.
- [179] H. Ali-Moussa, R. Navarro Amador, J. Martinez, F. Lamaty, M. Carboni, X. Bantreil, *Mater. Lett.* **2017**, 197, 171–174.
- [180] L. Xu, Y. Luo, L. Sun, S. Pu, M. Fang, R.-X. Yuan, H.-B. Du, *Dalton Trans.* **2016**, 45, 8614–8621.
- [181] M. J. Katz, Z. J. Brown, Y. J. Colón, P. W. Siu, K. A. Scheidt, R. Q. Snurr, J. T. Hupp, O. K. Farha, *Chem. Commun.* **2013**, 49, 9449–9451.
- [182] K. O. Otun, S. O. Amusat, I. T. Bello, J. Abdulsalam, A. T. Ajiboye, A. A. Adeleke, S. O. Azeez, *Inorganica Chim. Acta* **2022**, 536, 120890.
- [183] S. Kitagawa, *Acc. Chem. Res.* **2017**, 50, 514–516.

- [184] C. Li, T. Chen, W. Xu, X. Lou, L. Pan, Q. Chen, B. Hu, *J. Mater. Chem. A* **2015**, *3*, 5585–5591.
- [185] Y. Liu, Z. Tang, *Adv. Mater.* **2013**, *25*, 5819–5825.
- [186] H.-Y. Tan, Y. Zhou, Y.-F. Yan, D.-Y. Wu, W.-B. Hu, X.-Y. Shi, *Inorg. Chem. Commun.* **2017**, *79*, 74–77.
- [187] A. J. Amali, H. Hoshino, C. Wu, M. Ando, Q. Xu, *Chem. – Eur. J.* **2014**, *20*, 8279–8282.
- [188] P. Pachfule, D. Shinde, M. Majumder, Q. Xu, *Nat. Chem.* **2016**, *8*, 718–724.
- [189] X. Zhang, C. Y. Chuah, P. Dong, Y.-H. Cha, T.-H. Bae, M.-K. Song, *ACS Appl. Mater. Interfaces* **2018**, *10*, 43316–43322.
- [190] X. Ning, Y. Sun, H. Fu, X. Qu, Z. Xu, S. Zheng, *Chemosphere* **2020**, *241*, 124978.
- [191] L. Jiao, Y. Wang, H.-L. Jiang, Q. Xu, *Adv. Mater.* **2018**, *30*, 1703663.
- [192] C. Parmeggiani, F. Cardona, *Green Chem.* **2012**, *14*, 547.
- [193] G. Cainelli, G. Cardillo, in *Chromium Oxid. Org. Chem.*, Springer Berlin Heidelberg, Berlin, Heidelberg, **1984**, pp. 118–216.
- [194] A. Bavykina, N. Kolobov, I. S. Khan, J. A. Bau, A. Ramirez, J. Gascon, *Chem. Rev.* **2020**, *120*, 8468–8535.
- [195] A. Corma, H. García, F. X. Llabrés I Xamena, *Chem. Rev.* **2010**, *110*, 4606–4655.
- [196] G. H. Twigg, *Chem. Eng. Sci.* **1954**, *3*, 5–16.
- [197] Z. Guo, B. Liu, Q. Zhang, W. Deng, Y. Wang, Y. Yang, *Chem. Soc. Rev.* **2014**, *43*, 3480.
- [198] H. Yang, G. Li, G. Jiang, Z. Zhang, Z. Hao, *Appl. Catal. B Environ.* **2023**, *325*, 122384.
- [199] M. J. Beier, W. Kleist, M. T. Wharmby, R. Kissner, B. Kimmerle, P. A. Wright, J. Grunwaldt, A. Baiker, *Chem. – Eur. J.* **2012**, *18*, 887–898.
- [200] S. M. Hosseini, H. Dehghan, V. Safarifard, *Polyhedron* **2022**, *212*, 115581.
- [201] N. V. Soucy, in *Encycl. Toxicol.*, Elsevier, **2014**, pp. 43–45.
- [202] T. Ishida, M. Nagaoka, T. Akita, M. Haruta, *Chem. – Eur. J.* **2008**, *14*, 8456–8460.
- [203] S. Aryanejad, G. Bagherzade, A. Farrokhi, *Inorg. Chem. Commun.* **2017**, *81*, 37–42.
- [204] P. Guo, Q. Fu, C. Yildiz, Y.-T. Chen, K. Ollegott, C. Froese, W. Kleist, R. A. Fischer, Y. Wang, M. Muhler, B. Peng, *Catal. Sci. Technol.* **2019**, *9*, 3703–3710.
- [205] X.-F. Lu, L.-F. Gu, J.-W. Wang, J.-X. Wu, P.-Q. Liao, G.-R. Li, *Adv. Mater.* **2017**, *29*, 1604437.
- [206] W. Wong-Ng, J. A. Kaduk, H. Wu, M. Suchomel, *Powder Diffr.* **2012**, *27*, 256–262.
- [207] G. Calleja, R. Sanz, G. Orcajo, D. Briones, P. Leo, F. Martínez, *Catal. Today* **2014**, *227*, 130–137.
- [208] E. Welter, R. Chernikov, M. Herrmann, R. Nemausat, *AIP Conf. Proc.* **2019**, *2054*, 040002.

Appendix

Eidesstattliche Erklärung

Hiermit versichere ich, dass die vorliegende Arbeit selbstständig und nur unter Nutzung der angegebenen Quellen verfasst wurde. Außerdem versichere ich, dass diese Arbeit weder in dieser noch in ähnlicher Form einer anderen Prüfungskommission vorgelegt worden ist. Außer den mit dem Zulassungsgesuch urkundlich vorgelegten Graden habe ich keine weiteren akademischen Grade erworben oder versucht zu erwerben.

Kaiserslautern, den 22.02.2024

Milada Teubnerová

Curriculum vitae

Milada Teubnerová

Education

Doctoral studies

9/2018 – 12/2022
Ruhr-university Bochum, Technical university of Kaiserslautern
(since 2023 University Kaiserslautern-Landau)
Title: Heterogeneous single-site catalysts based on multi-
component metal-organic frameworks (MOFs) for sustainable
oxidation reactions in the liquid phase

Master studies

9/2016 – 6/2018
UCT Prague (VŠCHT Praha)
Field of study: Analytical chemistry and Quality Engineering
Thesis title: Vibrational spectroscopic study of acidobasic
properties of zeolites with tetravalent metals.

Bachelor studies

9/2012 – 6/2016
UCT Prague (VŠCHT Praha)
Field of study: Chemistry
Thesis title: The use of infrared spectroscopy, gas chromatography
with mass spectrometric detection and thermogravimetric analysis
for characterization of rubber raw materials and model mixtures

Scholarships

4/2019 – 12/2022 **SFB TRR247**, project number: 388390466

9/2018 – 12/2022 **IMPRS-RECHARGE**
Max Planck Institute, Mülheim an der Ruhr
